Development of a reversible solid oxide cell test station.

Thomas Johan Sebastiaan Wagemans

Technische Universiteit Delft

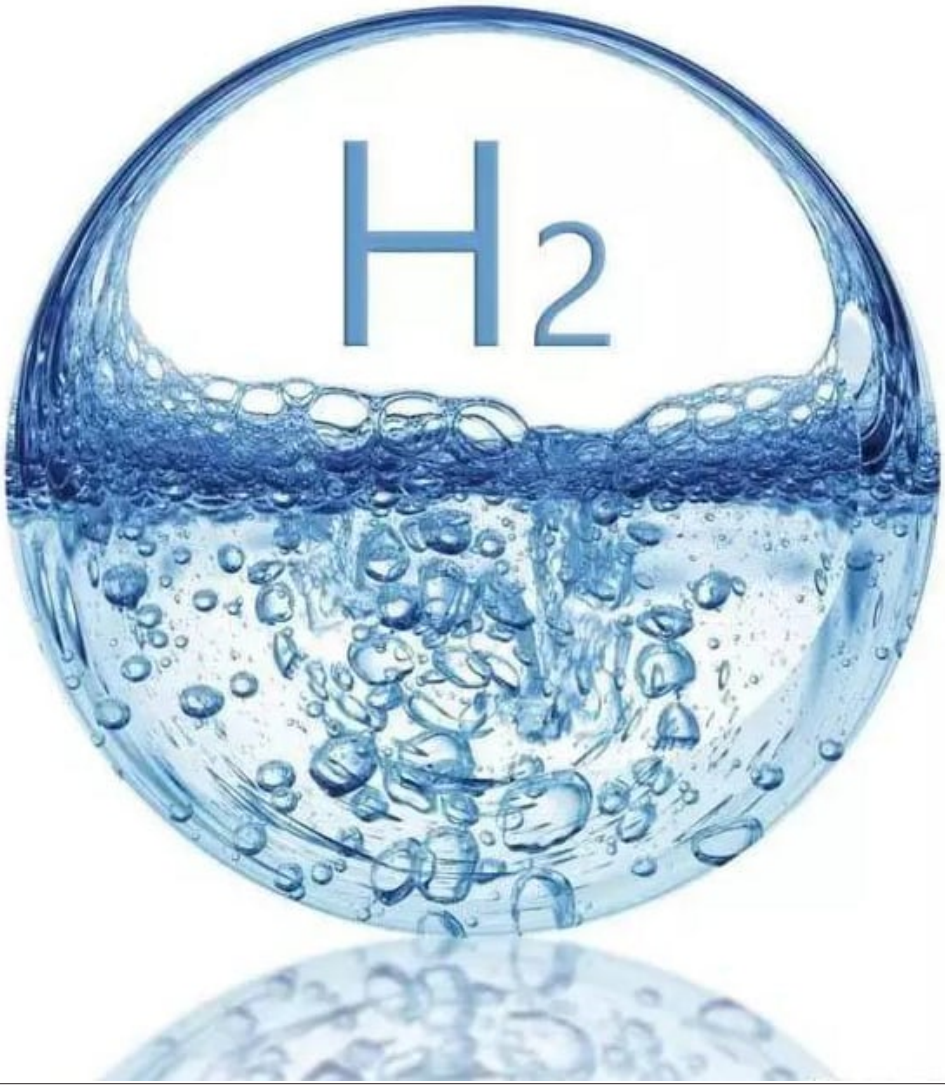

TU Delft Delft University of Technology

BALANCE

Challenge the future

DEVELOPMENT OF A REVERSIBLE SOLID OXIDE CELL TEST STATION

by

Thomas Johan Sebastiaan Wagemans

in partial fulfillment of the requirements for the degree of

Master of Science
in Mechanical Engineering

at the Delft University of Technology,
to be defended publicly on Monday December 16, 2019 at 13:00 PM.

Supervisor:	Prof. dr. P. V. Aravind	TU Delft
Thesis committee:	Prof. dr. ir. B. J. Boersma	TU Delft
	Prof. dr. D. J. E. M. Roekaerts	TU Delft
	Ir. T. Woudstra	TU Delft

TU Delft Delft University of Technology

Abstract

In a effort to curb climate change, more and more countries are adding solar and wind farms to their electrical grid. These solar and wind farms produce electrical energy based on environmental conditions, for example solar irradiation intensity or wind speed. As such these farms create fluctuations in the electrical grid and create a mismatch between energy supply and demand. To solve this problem the European Balance project proposes to use reversible solid oxide cell (ReSOC) systems. These systems can convert the excess energy produced by the solar and wind farms into an energy carrier when the supply of energy is bigger than the demand. At a later time this energy carrier can be reverted back to electrical energy when the energy demand is bigger than the supply. As these ReSOC systems are still in the development phase, experimental work is being carried out to develop these systems. For the Balance project the university of technology Delft (TuD) is tasked to determine the performance and the degradation, during constant operation and during cyclic operation, of a ReSOC system. To achieve these goals the university utilises a ReSOC test station. After use of the test station, the university found that the ReSOC systems showed high degradation and fractured within short use in the test station. As these results were not replicated by other balance partners, a cause for these results had to be found. In this work the test station was investigated to find the cause of the high degradation and breaking of the cells. After investigations of the voltage fluctuations and voltage spikes seen during electrolysis operation, it was found that water condensed in the fuel inlet duct. The liquid water droplets, formed as a result of condensation, caused the voltage fluctuations, high degradation and thermal gradients in the system that eventually fractured the cells. By redesigning the water injection system the fluctuations were reduced by 70% and the voltage spikes were completely removed. This indicates that the redesign solved the problem of water condensation in the fuel inlet duct. The resulting decrease in degradation rate of the ReSOC system extended the experimental duration up to a verified 1000 hours of continuous operation. The extended duration allowed the ReSOC system to complete 900% more cycles, within Balance protocol specification, whilst the current density was also increased by 60%. These improvements enable the test station to determine the objectives given by the Balance project. Whilst investigating the the high degradation, markings were found on the fuel electrode of the cells as well. A computational fluid dynamics (CFD) study confirmed that these markings indicated the fuel flow distribution. By converting the CFD data to current density and fuel utilisation data, it was shown that the overall performance of the ReSOC system was influenced negatively by the flow distribution plate. The results also showed that the ReSOC performance in the test station of the TuD can improve significantly if the fuel inlet flow is switched from a perpendicular to a tangential flow direction at the cell surface area. A redesigned flow distribution plate is therefore proposed that closely matches an ideal tangential flow distribution.

Acknowledgements

First and foremost, I would like to thank my parents for supporting me during my time at the university and enable me to complete the degree in my own pace. I would also like to thank my girlfriend Jolet for being there for me day and night and providing the mental support when needed, without her this report would have never been finished.

Furthermore, I would like to thank prof.dr. Aravind for his guidance during the project and Biju Illathu Kandy for proof-reading my report and providing me with valuable feedback.

Finally, I would like to thank Jonah, Kristin and Nuria for everything they have done for me during the master program, I learnt a lot from them.

Thomas Johan Sebastiaan Wagemans,
Delft, December 2019

Contents

List of Figures

List of Tables

Chapter 1

Introduction

1.1 background

On December 12th 2015, 174 states and the European Union (EU) signed the Paris agreement. In this agreement the parties agreed to reduce greenhouse gas emissions to limit the rise of global temperature to less than 2° Celsius above pre-industrial levels [1]. If the parties who signed the agreement want to achieve the goals set by the agreement, they have to radically rethink the way they create and use power in the industrial, commercial and transportation sectors.
A study done by the U.S. energy information administration in 2011 found that 32% of U.S. greenhouse gasses where produced by the electrical energy sector, which is 39.8% of the total emissions of the energy sector [2]. The same numbers are found by the Dutch bureau of statistics (CBS) for their country [3]. This gives an indication that the electrical energy sector is a big polluter in a lot of (western) countries. In order to meet the Paris agreement goals a significant number of these countries are rapidly substituting coal and other fossil fuel based power plants with more sustainable electricity production methods to generate their electricity. When it comes to the more sustainable electricity production methods hydroelectric turbines, photovoltaic solar panels and wind turbines are most frequently used [4]. Unfortunately solar panels and wind turbines have a great drawback: they are intermittent. This means that the power they produce can fluctuate from minute to minute due to environmental conditions such as sun hours and wind speeds, unlike a coal power plant which can run 24/7 at a constant power output. As the environmental conditions dictate when and how much power is produced, a mismatch between the power supply and demand is created.
To smooth out the fluctuating power production various ideas have been put into place. One example is pumped hydroelectric energy storage. This method of storing energy is used near hydroelectric power plants. These power plants utilise a large reservoir of water at a high altitude. When power is required the water from the reservoir flows through a turbine generating electricity. When there is an abundance of electrical energy, energy is used to pump water from a low attitude to the reservoir at high altitude. This way the energy is stored as gravitational potential energy. Another example is the large battery bank in Australia built by Tesla [5]. This battery bank can store energy when the wind turbines and solar panels produce more power than is consumed

and release the energy when more energy is required than they can produce. The battery bank solution is a very cost effective way of dealing with the power fluctuations. An other example, yet to be implemented in large scale, is the Balance project from the European Union [6]. The project uses reversible solid oxide cells (ReSOC) to convert the excess power from the electricity grid to transform water into an energy carrier, namely hydrogen. When there is an electrical power shortage, the ReSOC can be reversed. Using the hydrogen as a fuel to produce electricity. This process is depicted in Figure 1.1.

The main difference between using a ReSOC system over a solution like the Tesla battery bank is that it creates an energy carrier. This energy carrier can be hydrogen, synthetic gas or hydrocarbons. The benefit these energy carriers have over normal energy stored as a potential is their diverse applications. Potential stored energy can usually only be released in the form that it was used as to create the potential energy. Energy carriers are not limited by that restriction. For example, water and carbon dioxide can be fed to a ReSOC system to create synthetic gas during electrolysis. Synthetic gas is a mixture of hydrogen and carbon monoxide. This gas can be fed back through the ReSOC for fuel cell mode operation to create electricity or the gas can be used in applications that do not produce electricity. The gas can also be used to fuel combustion engines for planes and ships, or can be used as building blocks to produce other hydrocarbons [7]. If the carbon dioxide that is used during the electrolysis is sourced from air, the burning of synthetic gas, or resulting hydrocarbons, in planes and ships can be come part of a CO_2 neutral cycle, if the power for electrolysis is sourced from non greenhouse gas emitting power plant.

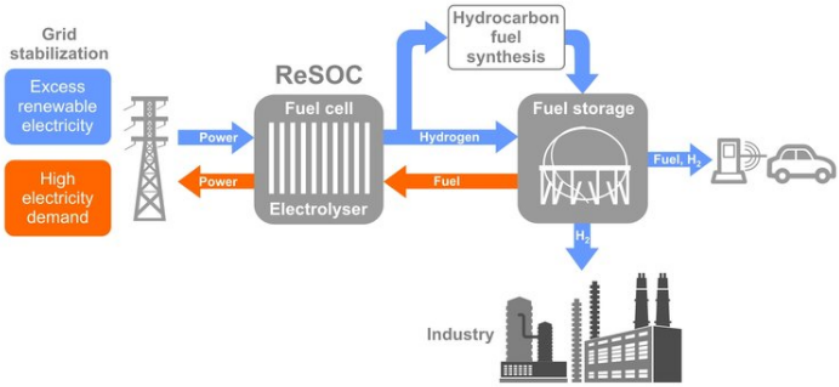

Figure 1.1: An overview of the Balance project process chain. Figure reprinted from [6].

As is with everything in life, nothing is perfect. The main challenge of the ReSOC system, at present time, is the relative poor economic viability. This is due to multiple reasons, one of which is the high operating temperature of 700-1200 degrees Celsius[8]. The high operating temperature means that exotic materials are needed to contain the system and that the energy to get the system up to that temperature it has to be generated. Ideally, this energy sourced from waste heat, however waste heat is scarcely found at these temperatures.

The process of turning water into hydrogen and back into water has a thermodynamic round trip efficiency limit of 98%, and whilst this sounds good, a currently commercially available ReSOC can only deliver a round trip efficiency of 55-60% [9]. To become economically viable, this number needs to go up and the operating temperature has to go down. Research and development in this area is therefore an active and ongoing process.

1.2 Thesis objective

The results from the experiments performed in the test station differed, in a negative way, from what was expected and what was achieved by other Balance partners. Therefore, in this thesis the reversible solid oxide cell test station which is in use by the university of technology Delft (TuD) for the Balance project is developed. The development of the test station is to lead to better and more reliable experimental results.

1.3 Thesis approach

The subject goal of the thesis is approached by firstly creating a computational fluid dynamics (CFD) analysis of the fuel flow distribution as a result of the flow distribution plate which is currently used in the test station. Using the data of this CFD analysis, a current density approximation is made. These results are compared to the results of a more ideal flow distribution to determine if the flow distribution in the test station can be improved in a significant way. With the results from this comparison a new design for a fuel flow distribution plate is made to achieve the more ideal flow distribution and thus a better performance.
Development of the liquid water injection system is done through analysis of the components of the original system, as used before this work. With the knowledge from the analysis a new water injection system is designed and produced for the test station. After the production the design is verified during experiments for the Balance project.

Chapter 2

Literature review

The main subject of this thesis is the reversible solid oxide cell, or ReSOC in short. In this section of the report a more detailed picture of the inner workings, advantages and challenges of a ReSOC is made.

2.1 Fundamentals of electrolysis and fuel cell

2.1.1 Reactions

A reversible solid oxide cell can be thought of as a rechargeable battery. Like a battery the cell has two electrodes, an Anode and a Cathode. On the surfaces of these electrodes reactions occur [10]. In electrolysis mode the hydrogen evolution and oxygen evolution reactions, abbreviated to HER and OER respectively, are shown in equations 2.1, 2.2 and 2.3. In this mode a power source is used to drive the reactions and converts water into hydrogen. The overall reaction is therefore endothermic. The cell is storing energy by creating an energy carrier.

$$Cathode(HER): \quad 2H2O + 4e^- \rightarrow H2 + 2O2^{2-} \tag{2.1}$$

$$Anode(OER): \quad 2O^{2-} \rightarrow O2 + 4e^- \tag{2.2}$$

$$Overall: \quad 2H2O \rightarrow O2 + 2H2 \tag{2.3}$$

In fuel cell mode the reverse reactions happen as shown in the reactions 2.4, 2.5 and 2.6. In this mode the energy carrier, hydrogen, is converted to its lower energy state, in this case water, releasing energy in the process. The overall reaction is therefore now exothermic.

$$Anode(HER): \quad 2H2 + 2O2^{2-} \rightarrow H2O + 4e^- \tag{2.4}$$

$$Cathode(OER): \quad O2 + 4e^- \rightarrow 2O^{2-} \tag{2.5}$$

$$Overall: \quad 2H2 + O2 \rightarrow +2H2O \tag{2.6}$$

As seen in the reactions above, the cathode and anode switch reactions as the mode is switched. The electrodes switch names because the electron flow reversed direction when the mode of the cell is changed. This can led to confusion when discussing a particular electrode. The electrode where the oxygen is reacting shall therefore be referred to as the "air electrode" and the other electrode as the "fuel electrode" in order to minimise confusion.

2.1.2 Thermodynamics

During electrolysis energy is required to split water molecules into hydrogen and oxygen. This energy is supplied to the molecules in two forms, electrical energy and heat energy. In Figure 2.1 a graph is shown where the energy demands for electrolysis are displayed against the operating temperature for a generic solid oxide cell in electrolysis. From the graph it is clear that with an increase in operating temperature the heat energy demand becomes greater. There are two ways of supplying the heat energy. At low heat energy demand, electrolysis cells usually supply this heat via losses in the cell, which will be explained more in detail later on. The high heat demand from electrolysis at high temperature, can also be provided via losses. However, at this point it becomes more efficient to utilise waste heat from other processes and allow the system to run in an endothermic manner. When the cell operates in an endothermic manner it contracts heat energy from the fuel and air streams. As the solid oxide cells typically operate at high temperatures, they can be integrated into other industrial processes if a suitable temperature match can be found. If the waste heat from other processes is used to supply the heat energy, a solid oxide electrolyser system could operate close to 90 to 100% electrical efficiency [11]. Operating at 100% electrical efficiency is defined so that the produced hydrogen has the same energetic value as the electricity that was put into the system, neglecting the energy from the waste heat input arguing that this energy would otherwise be wasted.

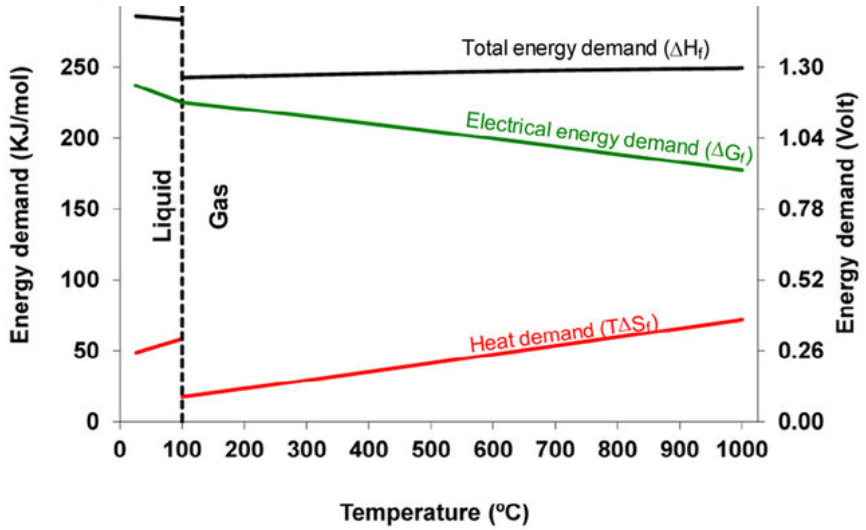

Figure 2.1: A graph showing the correlation between temperature and the electrical and heat energy demand for electrolysis. Figure reprinted from [12].

Lowering the operating temperature of a solid oxide cell for economic purposes poses a challenge. The ion conductivity of the electrolyte is strongly dependent on the temperature. As temperature decreases ion conduction becomes more difficult, which in turn explains the increases in specific resistance of a solid oxide cell at lower temperature [13]. This increase in resistance is the main reason behind the fact that the efficiency of a solid oxide cell decreases with a decrease in temperature. Solid oxide cells running in fuel cell mode are more affected by this decrease in efficiency than the cells running in electrolysis mode, as they can not absorb some of the extra losses within the cell as heat energy input. A solid oxide in fuel cell mode can not do this as the reaction is exothermic, which means that it always emits heats energy.
In Figure 2.2 the ion conductivity of certain ceramics is displayed. For a solid oxide cell a conductivity of 0.1 S/cm is the minimum requirement [14]. This means that a solid oxide cell with a YSZ electrolyte can not operate below 600 degrees Celsius, regardless of efficiency. To be able to operate at lower temperatures new ceramics are invented, such as GDC and DWSB that show better ion conduction at lower temperatures, enabling cell operation at lower temperatures.

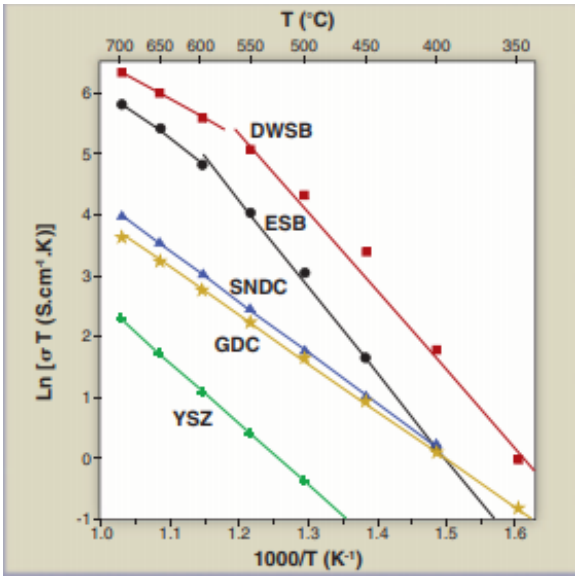

Figure 2.2: A figure showing the correlation between temperature and the ionic conductivity of several ceramics. Figure reprinted from ScienceMag.

Due to economic reasons the general trend of ReSOC is to decrease the operating temperature to below 500 degrees Celsius as the high temperatures (1000+ degrees Celsius) require the use of exotic materials. Because these materials are expensive to purchase and process, the system requires a large initial cost. With the decrease in operating temperature, more common types of materials become physically feasible to use in the system, lowering the cost of the ReSOC system significantly [15]. Another reason for lowering the operating temperature is market applications. With a lower operating temperature a solid oxide cell has a faster start up time, the time it takes to heat the cell up from room temperature to operating conditions. This faster start up time can open new markets for the solid oxide cell, such as the transport industry or the domestic appliances market. Furthermore a lower operating temperature means that more waste heat sources becomes suitable for use, widening the integration possibilities with other processes.

2.1.3 Overpotentials

The Nernst equation relates the equilibrium cell potential to the concentration gradient of an ion across a permeable membrane or electrolyte under non standard conditions [16]. In Equation 2.7 this relation is shown. In this equation Q denotes the reaction quotient which is a ratio of relative amounts of reactants and products. The letters R and F represent the constants known as the universal gas constant and the Faraday's constant respectively. The temperature is denoted as the variable T and the Gibbs free energy under standard conditions as G_f. The term standard conditions mean that the values are taken at room temperature, 298 Kelvin, and at atmospheric pressure.

$$E_N = \Delta \frac{G_f}{2F} + \frac{R * T}{2F} ln(Q) \tag{2.7}$$

As the equation determines the cell potential at equilibrium, it is used to calculate the potential of a cell when there is no net flow of electrons and ions [17]. This potential is therefore referred to as the open circuit potential, or OCV in short.
When the cell is in operation the potential of the cell increases or decreases due to several factors. The difference between the OCV and the cell potential during operation is called the overpotential. Overpotentials are also referred to as losses. These losses decrease the cell potential during fuel cell operation and increase the cell potential during electrolysis. In this chapter the equation for cell potential during fuel cell operation is made.

The cell potential change due to the movement of ions through the electrolyte and the movement of electrons. This is shown in Equation 2.8, where η_{ohm} denotes the losses due to electron and ion movement.

$$E_{Cell} = E_N - \eta_{ohm} - \eta_{con} - \eta_{act} \tag{2.8}$$

To calculate η_{ohm}, Equation 2.9 is used. In this equation the I denotes the current in the cell and Ω denotes the resistance to the electron and ion movement. The overpotential is therefore referred to as the ohmic overpotential as it is caused by ohmic losses.

$$\eta_{ohmic} = I\Omega_{el} \tag{2.9}$$

The resistance, Ω, is calculated with Equation 2.10, where τ is the thickness of the electrode or electrolyte layer and the σ is the conductivity of the layer.

$$\Omega_{el} = \frac{\tau_{air}}{\sigma_{air}} + \frac{\tau_{el}}{\sigma_{el}} + \frac{\tau_{fuel}}{\sigma_{fuel}} \tag{2.10}$$

To calculate the conductivity in the electrolyte layer, σ_{el}, Equation 2.11 is used, where C_1 and C_2 are constants determined by the material of the electrolyte and T is the temperature of the electrolyte [18].

$$\sigma_{el} = C_1 e^{\frac{C_2}{T}} \tag{2.11}$$

When there is current in the cell, species are consumed and produced. These reaction occur where the electrode, electrolyte and gas interface meet. This reaction site is called triple phase boundary. If the mass transport from and to the triple phase boundary is less than the conversion due to the current, a gradient of concentration of the species occurs. This gradient causes the cell potential to deviate from the OCV potential [19]. This is shown in Equation 2.8, where η_{conc} is the overpotential due to the concentration gradient. As the overpotential is caused by concentration gradients the overpotential is referred to as the concentration overpotential.

The concentration overpotential is made up of two equations as the gradient can be present at the fuel and air electrode. The η_{conc} is therefore the sum of Equations 2.12 and 2.13. In these equations the C_i denotes the concentration of a species in the bulk flow and the C_{iTPB} is the concentration of that species at the triple phase boundary. The R still denotes the universal gas constant, T the temperature at the triple boundary and F Faraday's constant.

$$\eta_{con,fuel} = \frac{R * T}{2F} ln(\frac{C_{h_2,TPB} C_{h_2O}}{C_{h_2O,TPB} C_{h_2}}) \tag{2.12}$$

$$\eta_{con,air} = \frac{R*T}{2F} ln(\frac{C_{O_2,TPB}}{C_{O_2}}) \tag{2.13}$$

The triple boundary concentration is for these equations is calculated with Equation 2.14. In this equation τ represents the thickness of the electrode, n the number of free electrodes per molecule, D_{eff} the effective diffusion coëfficient and j the current density. The current density is the current per surface area. The number of free electrons per molecule is 1 at the fuel electrode and 2 at the air electrode. This difference is due to the fact that the oxidation state for hydrogen is +1 and the oxidation state for oxygen is -2.

$$C_{i,TPB} = C_i + (\frac{\tau}{2*n*D_{eff}*F})j \tag{2.14}$$

Like every other chemical reaction, to start the reaction an activation energy needs to be supplied. The overpotential related to these chemical reaction kinetics is referred to as the activation overpotential, shown in Equation 2.8 as η_{act}.

Like the concentration overpotential, the activation overpotential consists of two parts as reactions occur on both electrodes. The activation overpotential is the sum of Equations 2.15 and 2.16. These equations are better known as the Butler-Volmer equations. In these equations C_r is the concentration of reactants, C_p the concentration of the products, j_0 the exchange current density and α is the charge transfer coëfficient, which is usually taken as 0.5 [20].

$$\begin{aligned} j = j_0(&\frac{C_{r,TPB}}{C_r} exp(\frac{2*(1-\alpha)*F*\eta_{act,fuel}}{R*T}) - \\ &\frac{C_{p,TPB}}{C_p} exp(\frac{-2*\alpha*F*\eta_{act,fuel}}{R*T})) \end{aligned} \tag{2.15}$$

$$\begin{aligned} j = j_0(&e^{(\frac{2(1-\alpha)*F*\eta_{act,air}}{R*T})} - \\ &\frac{C_{r,TPB}}{C_r} * e^{(\frac{-2*\alpha*F*\eta_{act,air}}{R*T})} \end{aligned} \tag{2.16}$$

At both electrodes the exchange current density is calculated with Equation 2.17. In this equation i denotes either the fuel or air electrode, k the pre-exponential factor and $E_{electrode}$ the activation energy.

$$j_0 = \frac{R*T}{2F} * k_{electrode,i} * e^{\frac{-E_{electrode,i}}{R*T}} \tag{2.17}$$

2.1.4 Reaction rates

As the ReSOC that is subject to this research is converting water to hydrogen and back, there is a need for an equation that determines how much of each species is converted. Equation 2.18 can be used for this purpose [21]. In this equation n is the number of free electrons per molecule, j the current density, $\dot{m}_i$ the consumed mass per species and M_i the molar mass per species.

$$\dot{m}_i = \frac{A*j*M_i}{n*2*F} \tag{2.18}$$

As the concentration of the reactants, water and hydrogen, changes over the length of the cell the overpotentials change, which in turn impact the local current density. This means that the reaction rate is one of the causes that the current density fluctuates along the cell. Another factor for the fluctuations is the variation of temperature along the cell. This temperature fluctuation is due to the heat conduction from the cell to the gas streams and the local losses in the cell.

2.2 The components and degradation mechanisms of a ReSOC

In this section the three main components of the ReSOC, the electrolyte, the electrodes and the current collectors are discussed. As well as discussing the three main components, some attention is given to the degradation mechanisms as this is still an important research area of the ReSOC.

2.2.1 Electrolyte

The material properties of the electrolyte significantly influence the operating temperature of the ReSOC. The electrolyte conducts the ions, O^{2-}, from one electrode to the other electrode. To ensure the resistance for the ion movement are minimised, the electrolyte is kept as thin as possible and the material should have good ionic conductivity. In the latter of those constraints lays the problem. Most materials conduct ions better at high temperature, as was shown in Figure 2.2. When operating at high temperatures more material constraints are put in place, such as that the thermal expansion coëfficients should be compatible with electrode materials. This eventually led R. Ruka et al. at the Westinghouse Power Corporation to use YSZ, also known as Yttria-Stabilized Zirconia [22]. This material since then the most common type of high temperature electrolyte, as it offers good chemical stability and excellent thermal compatibility with electrode materials. Although the research into lower temperature electrolyte materials is gaining traction and has its own advantages and challenges, it is not discussed further in this thesis.

2.2.2 Electrodes

On the air electrode the first challenges appear due to the oxidation environment and high temperature. The first generations of SOFC used Lanthanum Strontium Manganites, abbreviated to LSM, as electrode. These first generations electrodes could be operated at 1273 Kelvin. This material is now widely used as electrode material in high temperature solid oxide cells as it provides good chemical stability, as this was given a higher priority in early prototypes. Research found that if the operational temperature is lowered the material rapidly decreases in performance. At these lower temperatures it also becomes vulnerable to poisoning by chromium containing gasses [23]. These gasses can come from the oxidation of the chromium containing metal casings, interconnects or tubing.
To solve these problems with LSM researches switched to Lanthanum Strontium Cobaltite, or LSC. Unfortunately it was quickly discovered that LSC degrades rapidly due to the reactions that occur with the YSZ electrolyte. In order to prevent these reactions from from happening a CGO (Ceria-Gadolinia) layer is placed between the LSC electrode and the YSZ electrolyte. This CGO layer is a very good conductor of oxide ions and prevents the conduction of strontium ions, which

caused the reactions with the YSZ electrolyte [24].

The fuel electrode is often made out of a cermet. For the metal component Nickel is widely used. The ceramic component is often the same material as the electrolyte, YSZ. For the production of the cermet coarse and fine grains of YSZ are used. The coarse grains form a framework on which fine grains of nickel and YSZ are deposited. This framework reduces the anode thermal expansion coëfficient making it closer to that of the electrolyte. As the framework is made of YSZ, the anode acts as an ionic as well as an electronic conductor which increases the triple phase boundary area. The framework can also make the anode more stable. The relatively low melting temperature and higher sintering ability of a pure nickel anode can cause a reduction of porosity due to nickel agglomeration and grain growth. Using a cermet with a framework of YSZ can minimise the nickel agglomeration and nickel grain growth [25].
The choice of Nickel as a electrode is based on the low cost, the good performances at high temperature and the fact that it can be made into a porous structure aiding the fuel to reach the electrolyte [26].
If the fuel electrode is thicker than the air electrode, the cell is said to be anode supported. The extra thickness given by the support is to give the cell more mechanical strength. A cell with a thicker air electrode is referred to as an cathode supported cell and a cell with a thicker electrolyte is called an electrolyte supported cell. A cathode supported cell can offer more outright performance compared to the other types of support. A electrolyte supported cell offers better economic value compared to the other support types. The anode supported cells offer a compromise between the economic value and performance as well as better long term stability than cathode supported cells [27].
An alternative to adding material to a layer to increase the mechanical strength of the cell, is to support the cell the interconnect or to add a porous metal on the electrodes to support the cell. The material for the porous metal has to be carefully chosen to prevent unwanted reactions, ohmic losses and mismatching of thermal expansion coefficients. Although Anode supported cells are still the most common type of cell support, interconnect supported cells are becoming more common. This is to maximise cell performance and lower costs, as less material is needed [28][29].

2.2.3 Current collection

The transport of electrons away from and towards the electrode is referred to as current collection. Current collectors come in three different forms, the air electrode current collector, the fuel electrode current collector and the interconnect. The interconnect is often used if multiple cells are connected in a stack, as depicted in Figure 2.3. The interconnect carries the electrons from the air side of one cell to the fuel side of the next cell. The conduction of electrons in this manner effectively puts the cells in series, thus creating a bigger voltage difference at the same current. The stacking in series is common practise as the currents produced by even small single cell, capable of producing approximately 10 Watt of power, in fuel cell mode can produce currents as high as 20 ampère. This amperage is good enough for some applications. This current however is coupled to a potential of 0.5 volt, which if often too low to be usable.
As a single cell setup does not need interconnections, the current is usually collected differently. At the air electrode the current is collected by a gold or platinum mesh on top of the electrode. The materials of the air electrode current collector is based on the behaviour of the material at high temperature oxidising environment and catalytic properties [30]. The mesh connects the electrode

to the electrical subsystem.
The fuel electrode current collector is often a nickel foam. This foam is electronically connected to the (metal) housing of the cell. The housing is in turn connected to the electrical subsystem. As the fuel electrode is connected to the metal housing it is of utmost importance that the air electrode is well insulated from the metal housing to prevent short circuiting. The reason nickel foam is chosen as a current collector as it offers a thermal expansion relatively close to that of the cell, high porosity to allow the fuel to reach the electrode reaction sites and it is relatively cheap [31].

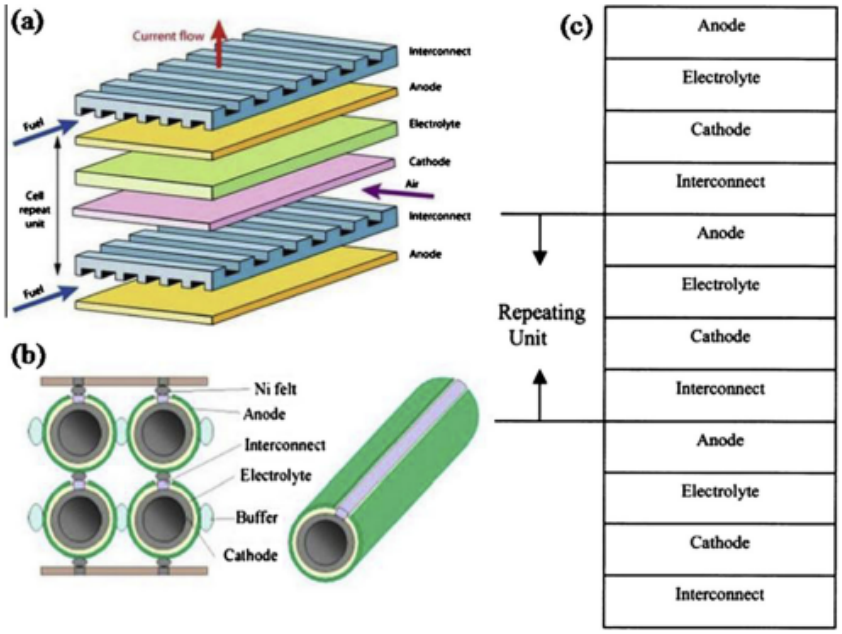

Figure 2.3: A representation of a planar and a tubular stack configuration. Figure reprinted from [32].

2.2.4 Degradation mechanisms

Together with the initial cost and operating temperature, longevity is still a major issue that needs development if the technology is to become financially feasible. As such, research has focused on understanding the mechanisms of cell degradation as well. These mechanisms can cause the cell to fail instantaneously or slowly lose performance over time. If the mechanisms of cell degradation are understood, the cell can be designed to counter the degradation. There are many degradation mechanisms as described by a study of DTU, shown in Figure 2.4 [33]. This report will only briefly discuss four common types degradation mechanisms: thermal expansion mismatching, poisoning/electrode coarsening, cell delamination and nickel depletion.

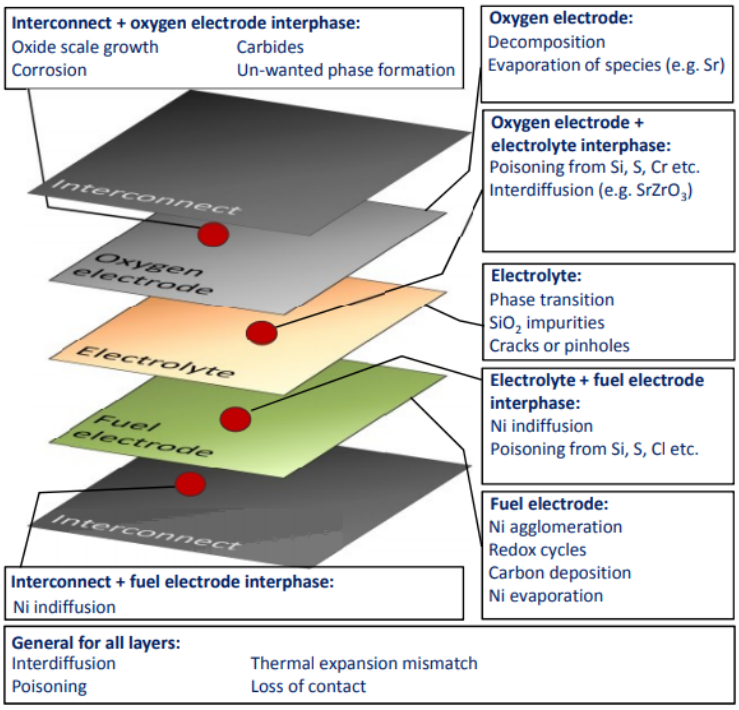

Figure 2.4: An overview of the possible degradation mechanisms identified by researchers at DTU. Figure reprinted from [33].

All degradation mechanisms interfere with how the chemical conversion happens. In Figure 2.5 the three main pathways of oxygen molecules in the triple phase boundary are shown at the air electrode-electrolyte interface. When a degradation mechanism takes place these pathways can get completely blocked off or become significantly more restricted[34].

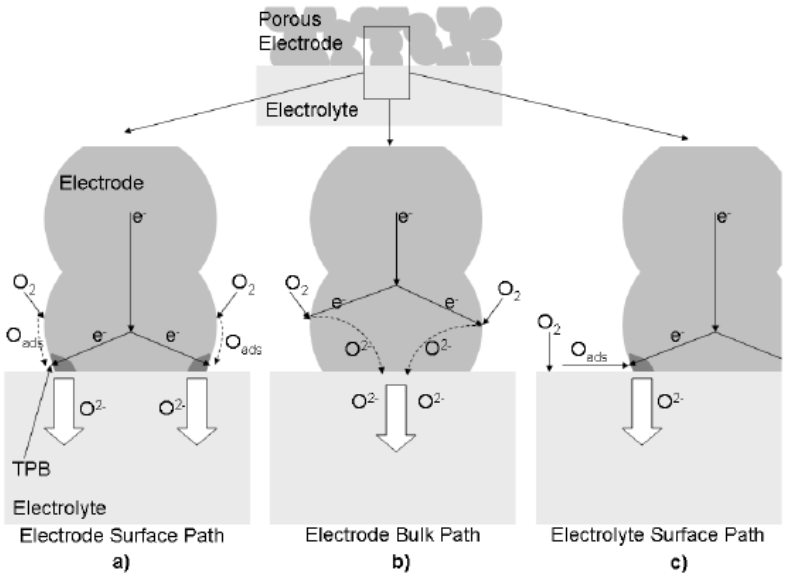

Figure 2.5: Pathways of oxygen in the triple phase boundary. Figure reprinted from [35].

Thermal expansion mismatching happens when two components are connected to each other but have different thermal expansion coëfficients. When the system heats up or cools down the components expand and contract at different rates. This causes mechanical stress which can break the bond connecting the components or break one of the components. This mismatching of thermal coëfficients can cause the cell to break on the initial warm-up or shortly after the first use. Fortunately the materials mentioned in the sections above have already been carefully selected to have matching thermal expansion coëfficients [36]. Often the thermal expansion coëfficient of the components is matched to that of the electrolyte, YSZ, as this is the material that is most difficult to change. The expansion coëfficients of the materials around the cell, such as the housing and the seals, are often no issue as these components can expand freely because they are not connected to the cell[37].

Electrode poisoning and electrode coarsening have similar effects on cell performance. Both increase the resistance of the electrode pathways to the triple phase boundary, which leads to a deterioration cell performance. The performance of the cell doesn't immediately drop, rather it starts to degrade steadily. This is a telltale sign that the cell is influenced by one of these mechanisms. Post-mortem investigation or Electrochemical Impedance Spectroscopy (EIS) measurements of the cell can reveal which of these mechanisms was the reason for degradation.

Under certain conditions the oxygen in the air stream flowing towards the cell can react with the components of the inlet duct. When the oxygen reacts with components of the inlet duct it is often with chromium, however cases of boron and sulphur poisoning are known. The reaction between the oxygen and chromium produces chromium(III)oxide. The chromium(III)oxide detaches from

the metal and floats on the inlet stream to the electrode where it deposits on the electrode. This blocks off a part of the electrode/electrolyte area for fresh air. As Chromium(III)oxide is being produced in the air inlet, the electrode becomes more blocked off as time progresses, and thus the performance steadily declines as the cell effectively becomes smaller[38]. It is observed that LSM electrodes are more susceptible to chrome poisoning than LSC electrodes, while the reverse is true for sulphur poisoning [39]. There is no reported significant difference between LSM and LSC with regards to Boron poisoning [40]. The operating and gas inlet temperature play a crucial role in preventing chromium poisoning. The chromium oxidation reaction happens above 800 degrees Celsius. This means that an operating temperature or an inlet stream of more than 800 degrees can increase the chances of chromium poisoning, when using chromium containing metal parts[41].

At the fuel electrode silica poisoning is a well known phenomenon. The origin of silica poisoning is still debated within the scientific community. Some believe that it comes from the glass sealing, some believe that the silica comes from the water and others contribute the source to rubber tubes. Silica poisoning happens as silica which is transported to the cell by the fuel gas stream, where it reacts with oxygen at the triple phase boundary to SiO_2 and blocks off the fuel reaction sites[42]. When hydrocarbons, carbon dioxide and carbon monoxide are used as reactants in solid oxide cells, sulphur poisoning and carbon deposition at the fuel electrode is known to happen. In Reference [25] it is mentioned that this is still an active area of research as the nickel/YSZ cermet electrode has poor tolerances when these degradation mechanisms happen.
Coarsening is also known as grain growth. Grain growth is when two grains of a material, which are in contact with each other, form a new single bigger grain. The process is depicted in Figure 2.6. The fusing of grains is dependent on the temperature of the material, the time it is exposed to that temperature and the initial grain size and shape. The coarsening of the nickel electrode causes a decrease in the density of three phase boundaries and total nickel surface area. The coarsening of nickel therefore causes a reduction of sites where the chemical conversion of water and hydrogen can occur. Furthermore, it can cause a decrease in electrical conductivity of nickel, increasing the ohmic losses [43]. Due to developments in cermet fuel electrode production the nickel grain growth can be minimised as described in Reference [25].

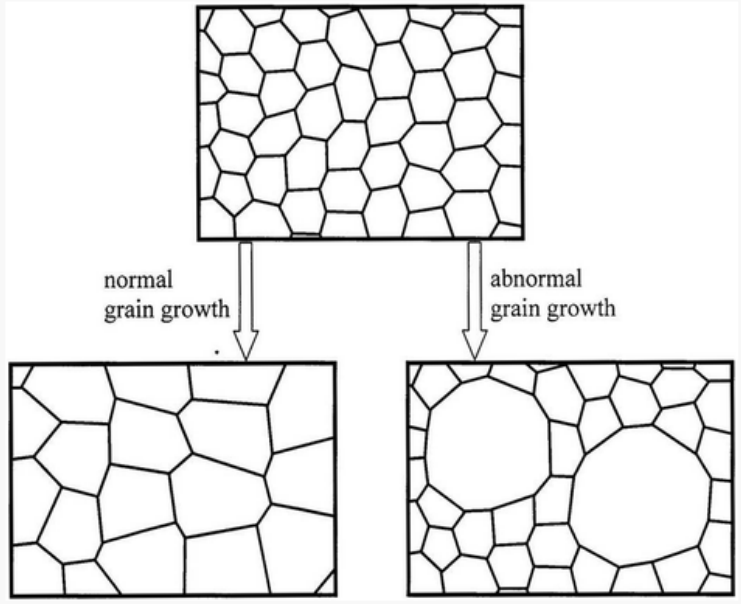

Figure 2.6: A basic representation of grain growth. Figure reprinted from [44].

Arguably, the most destructive form of degradation is delamination of the cell. Delamination is when two layers start to separate from each other. Delamination in solid oxide cells can happen between the air electrode side and the CGO barrier layer, between the YSZ electrolyte and the CGO layer or between the CGO layer and the LCS. These delamination types are shown in Figure 2.7. In this figure the delamination between the electrolyte and CGO layer is shown in Figure (b) and the delamination between the CGO and LSC layer in Figure (c).

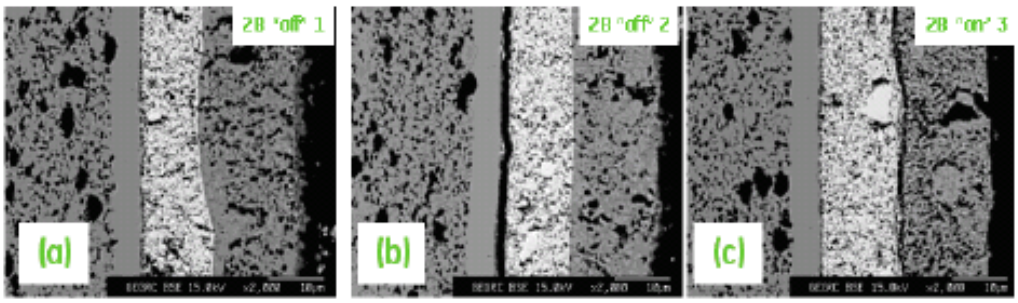

Figure 2.7: The two delamination cracks that can occur at the air electrode. Figure reprinted from [45].

When delamination occurs the cell performance drops suddenly and steeply, unlike the previous mentioned degradation mechanisms. The sharp decrease of performance is due to the sudden inability of the oxygen ions to pass through the boundary connection between the layers. When an electrode delaminates from the electrolyte or the barrier layer the ion transport is locally

interrupted and the active chemical conversion sites disappear. Likewise if the barrier layer delaminates from the electrolyte the path of the oxygen ions becomes longer, and thus more difficult, or even completely blocked off. Delamination of the air electrode happens more frequently than the other delamination possibilities mentioned above. The main reason for this delamination was determined to be an increase in oxygen partial pressure in the electrolyte underneath the air electrode. This partial pressure can break the bond between the electrode and the electrolyte or even the electrode itself. The increase in pressure can become strong enough that it can overcome traditional strengthening measures that try and prevent it, thus other methods have to be developed to prevent the oxygen pressure build up. The phenomenon is more likely to happen during electrolysis than during fuel cell mode [46]. During electrolysis it is possible that at the fuel electrode more oxygen ions are produced than can be released by the air electrode. This leads to a buildup of oxygen ions in the electrolyte. This buildup of oxygen ions causes the oxygen ions to redistribute inside the electrolyte and increase the partial pressure underneath the air electrode. It is this increase in pressure that causes the split of the electrode and electrolyte layers [47][48][49].
Delamination can occur on the fuel electrode, however this is much more rare than air electrode or barrier layer delamination. Fuel electrode delamination can occur when there is a large enough difference between the thermal expansion coëfficient of the electrode and the electrolyte. When, for example, the electrode is attached to the electrolyte and is expanding more than the electrolyte during heating it might detach from the electrolyte to be able to accommodate for the extra expansion. Due to the constant development of materials as mentioned before, this type of delamination is becoming increasingly rare.

For the fuel electrode, nickel depletion or agglomeration is one of the more common degradation mechanism together with nickel grain growth. During nickel depletion nickel starts to evaporate or diffuse into the housing. When this occurs, especially at high current densities and high potentials, nickel migrates away from the electrolyte. When the migration happens the reaction sites are moved away from the electrolyte, increasing losses. At temperatures of 950 degrees Celsius and above it is observed that the nickel moves towards the electrolyte clogging the pores. This is known as nickel agglomeration. Unfortunately these two nickel movements can not be used to reduce the effects of the other [50][51].

2.3 Computational fluid dynamics

Computational fluid dynamics, often abbreviated to CFD, is a part of fluid dynamics that uses numerical analysis to describe flows. This tool is also used in the field of solid oxide cell research. When it is used in this field of research, it is usually coupled with an electrochemical model to solve for the reactions and mass transfer phenomenons associated with solid oxide cells. Many of the studies done on CFD for solid oxide cells are centred around the interconnects. Which is logical as solid oxide cells will only be used in multiple cell stack setups in industrial applications. However, a significant portion of experimental work is still being carried out on single cell setups. This discrepancy between the experimental and simulation work causes a lack of understanding on how single cell setups function. In this section the literature gap between the CFD analysis of stack

systems and single cell testing and modelling is addressed.

The main difference encountered between the stack CFD models and single cell experimental conditions is the mass flow inlet conditions. The mass flow inlet conditions determines how mass enters a flow area or volume above the cell electrode. In CFD analysis studies the inlet flow is usually supplied as depicted in Figure 2.8. A uniform inlet condition across the whole inlet area at one side of the cell, creating flow tangential to the cell [52][53][54] [55][56]. However, creating this inlet condition in experimental setups brings significant challenges. In stack setups the total mass flow to each cell can be different due to a sub optimal flow distribution. Even on a cell level, the mass flow per channel across the cell can vary significantly.
For single cell setups creating this specific inlet condition seen in Figure 2.8 is challenging as well as sealing is a big challenge for ReSOC systems. This is due to the operating temperature and the fact that hydrogen is the smallest molecule, thus diffusion through sealing imperfections happens relative quickly. To aid sealing in single cell setups, the inlet(s) and outlet(s) are often moved to the top of the cell supplying mass flow perpendicular to the cell rather than tangential [57][58][59].
Supplying the mass flow for a cell perpendicular, instead of tangential to the cell, not only creates a difference at the inlet, the flow distribution across the cell surface differs significantly as well. The streamlines in the CFD studies have a relative small curvature, this does not hold true if the cell inlets are perpendicular to the cell [60].

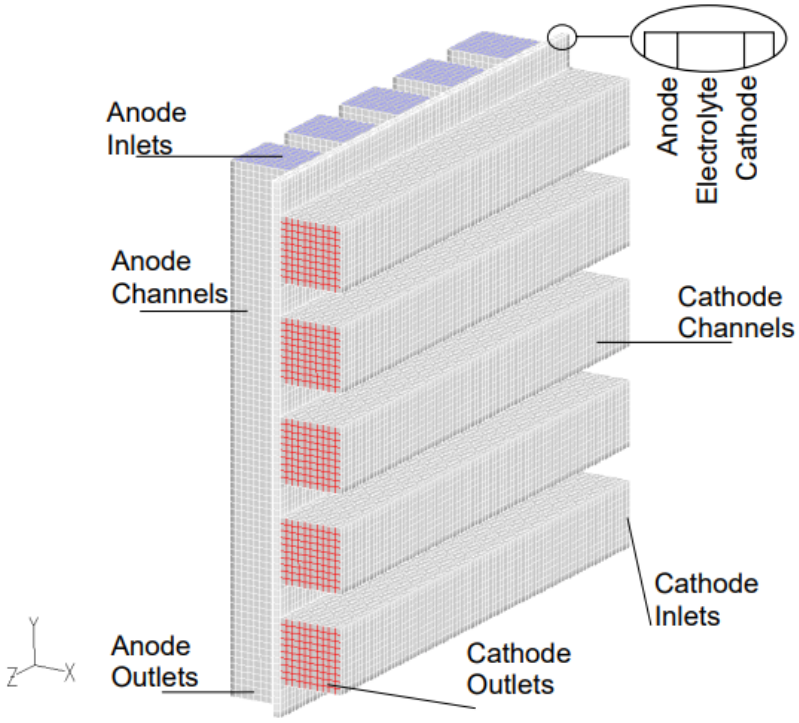

Figure 2.8: A Figure depicting commonly used anode and cathode inlet conditions for CFD studies. Figure reprinted from [61].

On a interesting note, only 3 of the 10 CFD studies used as reference in this section have disclosed some form of the velocity (or streamline) results in their report. The other studies fail to mention the velocity results in their reports as they focus on other aspects, such as temperature or concentration development along the cell. It is interesting to note this, as the velocity flow profile gives a good and easy visual indication if the CFD simulation has correctly applied the right boundary conditions which are the necessary constraints that are needed to solve differential equations.

Chapter 3

Experimental test strategy and setup

3.1 Experimental test strategy

3.1.1 Objectives

According to the Cambridge dictionary, an experiment is an test preformed in order to learn something. It is therefore of vital importance that what needs to be measured to learn said thing is clear. In the case of the Balance project, the experiments are performed to determine the following properties of a solid oxide cell:

1. The degradation caused by cyclic operation.

2. Cell performance in fuel cell and electrolysis operation.

3. Steady state fuel cell and electrolysis performance degradation over time.

Performance in the above mentioned properties is defined as the voltage at a certain current density. During fuel cell operation a higher voltage is defined as a better performance as more power is produced, likewise during electrolysis a lower voltage is better as less power is consumed by the cell. The performance for both fuel cell and electrolysis operation is displayed with an i-v curve. An i-v curve is made by measuring the potential of a cell at various current densities. Performance degradation is measured by the difference between two i-v curves that have been taken a certain amount of operational time apart.
With the objectives clear, a test plan or protocol can be made. This protocol contains a detailed plan of how experiments are going to be performed in order to determine the properties mentioned above.

3.1.2 Protocol

The experiments during this thesis were conducted following the Balance project test protocol, as made by DTU. This protocol is depicted in Figure 3.1. Testing is started off by heating the cell to 850 degrees Celsius to reduce the nickel oxide in the fuel electrode to nickel, after which the temperature is lowered to 750 or 700 degrees, depending on the experiment. Experiments begin by making an i-v curve for both fuel cell and electrolysis operation to asses cell performance. After the initial i-v curve measurements the cell is operated for 120 hours in fuel cell mode, after which another i-v curve is taken. The same is than done with electrolysis mode. These sections of continuous operation in one single mode will be referred to as constant current operation. With these i-v curves the performance degradation over time of each mode can be assessed. With each i-v curve measurement an electron impedance spectroscopy measurement is also taken to determine the change in the area specific resistance of the cell over time. The constant current operation modes are done with a current density of 0.5 A/cm^2.
After two periods of constant current operation, cyclic operation is used to determine the degradation caused by switching between the operational modes. During a cycle the cell will run 3 hours in fuel cell mode and 20 hours of electrolysis, which means that there is 1 hour to change the modes back and forth. For the experiment the cycle has to be repeated 33 times, given that the cell voltage remains between the cell voltage limits.
For the lower voltage limit during fuel cell operation, 0.4 volt is chosen. Because the potential difference between the two electrodes is the main driving force transporting the oxygen ions through the electrolyte, this driving force can not become too low. If this driving force becomes too low the oxygen transport through the electrolyte is stopped and the current through the device drops to 0. To prevent this from happening the minimum potential between the electrodes is set to 0.4 volt. The upper limit of 1.7 volt during electrolysis is chosen based on system performance requirements. As the cell voltage rises above a certain value during electrolysis, the system starts to emit heat energy. The higher the cell voltage, the more heat is emitted from the cell. This heat output from the cell has an effect on the systems that it is integrated with. To limit the heat output, the cell voltage is limited to 1.7 volt during electrolysis.
Due to safety regulations, only 4 cycles were done per week, as the system was not allowed to operate during the weekends. During the weekends the system was left in fuel cell mode without current draw, referred to as OCV-mode. The cyclic operation is done at 0.5 A/cm^2 as well. After the 33 cycles, or if the cell voltage exceeds the maximum or minimum values, a final i-v curve and EIS measurement is taken for both operational modes. With these measurements the degradation due to cyclic operation can be determined.
To give more insight in the performance of the cell, the cyclic operation is also performed with a higher current density of 1.25 A/cm^2 and a lower operating temperature of 700 degrees Celsius.

The volume flow rate during operation is prescribed as well by the Balance project. This makes the results from experiments easier to compare to the results from other Balance partners. The volume flows for operation are shown in Table 3.1 at atmospheric pressures and at 25 degrees Celsius. The water volume flow is an exception to this, as it needs to be vapour and therefore its volume flow rate is given at 101 degrees. To achieve the higher current density of 1.25 A/cm^2 at approximately the same fuel utilisation, all volume flows in Table 3.1 are multiplied by 2.5.

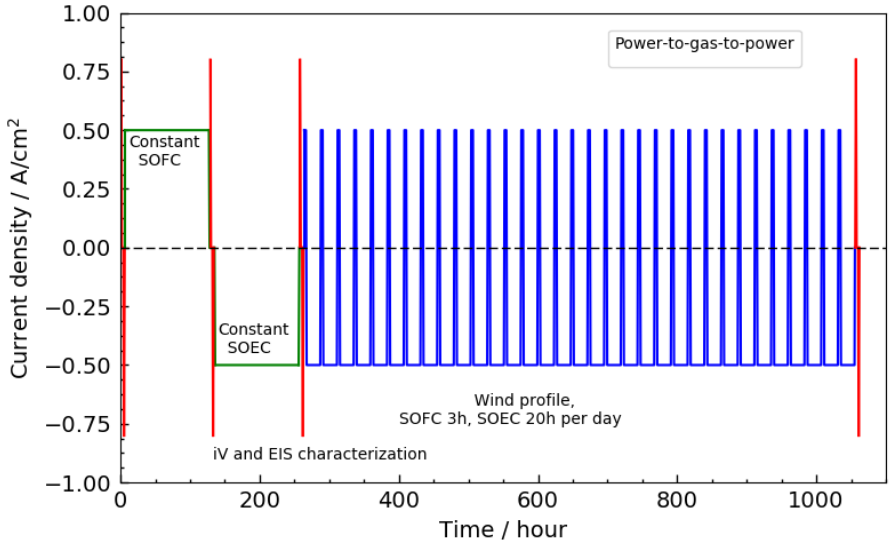

Figure 3.1: Balance project test protocol as made by DTU.

Table 3.1: Prescribed operating conditions

opertional mode	Fuel cell	Electrolysis
Air composition	21/79 (O_2/N_2)$[volume\%]$	21/79 (O_2/N_2)$[volume\%]$
Air volume flow	1000 [ml/min]	250 [ml/min]
Fuel composition	50/50 (H_2/N_2)$[volume\%]$	45/45/10 ($N_2/H_2O/H_2$)$[volume\%]$
Fuel volume flow	320 [ml/min]	365 [ml/min]

3.1.3 Cells used for testing

The cells used for testing have a total surface area of 25cm^2, with an active area of 16cm^2. The cell were supplied by DTU. These cells have a YSZ electrolyte and a LSC air electrode with a CGO boundary layer between the air electrode and the electrolyte. The fuel electrode is made of a Ni-YSZ cermet, on which the cell is supported. Table 5.5, gives the specific thickness of each layer. During experiments generation 1 and generation 2 cells were used. According to personal correspondence with DTU, this should not effect the performance in the initial i-v curves. Generation 2 cells should have an decrease in degradation over time due to improved manufacturing process, compared to generation 1 cells. A detailed description on cell preparation and operation of the cell during experiments is given in Appendix D.

3.2 Test station details

To perform the experimental protocol a test setup is used which is shown, schematically, in Figure 3.2. The oven, in which this setup resides, and the electrical connections are not drawn here for simplicity in this figure. In this figure the blue arrows represent the air flow and the red arrows the fuel and exhaust flow. Figure 3.3 in combination with Table 3.2 show the name (and function) of the components of the setup. The naming scheme of upper and lower inconel housing can be confusing as the setup is drawn in assembly orientation in Figure 3.2 and is rotated 180 degrees once it is inside the oven, as seen in Figure 3.4. The inconel housing that incorporates the fuel in and outlets will be named the lower inconel housing.

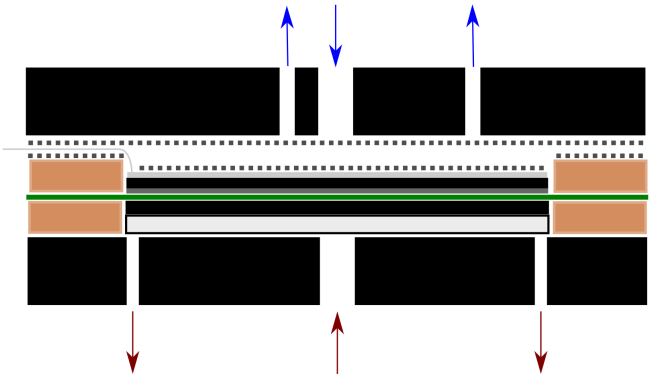

Figure 3.2: A schematic overview of the test setup.

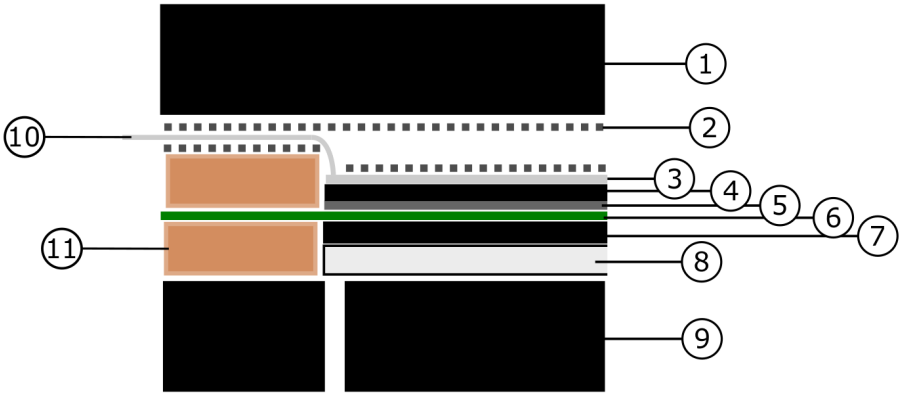

Figure 3.3: Naming of the components inside the cell.

Table 3.2: Naming of the components of the test setup.

Number [#]	Description
1	Upper inconel housing (flow distribution)
2	Alumina felt (electrical insulation)
3	Platinum mesh (current collector)
4	LSC (air electrode)
5	CGO boundary layer
6	YSZ electrolyte
7	Nickel-YSZ layer (fuel electrode)
8	Nickel foam (current collector)
9	Lower inconel housing (flow distribution)
10	Platinaum wires
11	Mica sheet (sealing)

The setup is connected to the outside world via the inlet and outlet ducts that carry the gasses to and from the setup. These ducts are connected to the lid of the oven, allowing the cell to be suspended in the middle of the oven. This is shown in Figure 3.4. In this figure the electrical connections are not drawn for simplicity. As the ducts carrying the gasses to the cell travel a distance in the oven before reaching the setup, the gasses get preheated. The exhaust gasses are carried away via ducts leading to a condenser. After the condenser the exhaust gasses are vented safely out of the building. The air coming from the cell is dumped into the oven, which has a small hole in the side to prevent a pressure build up.

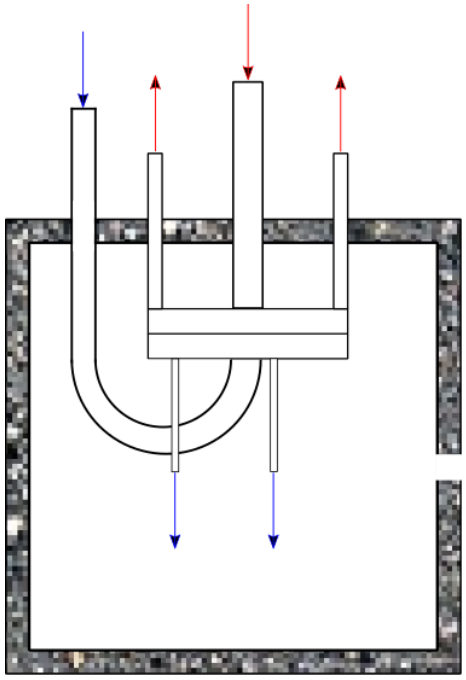

Figure 3.4: A simple representation of the setup inside the oven.

For the mica seals to function properly a pressure needs to be applied on them. To apply this pressure on the seals four springs, one at each corner, are compressed on top of the lower inconel housing. One of these springs is shown in Figure 3.5. Table 3.3 shows the names of the components of the clamping mechanism. These springs have an initial length of 29 millimeter and are compressed to 26 millimeter, applying 9 kilograms of force each. This means a total pressure of 1 kilograms per square centimetre is put on the cell, as the total area including the mica seals is $36cm^2$.

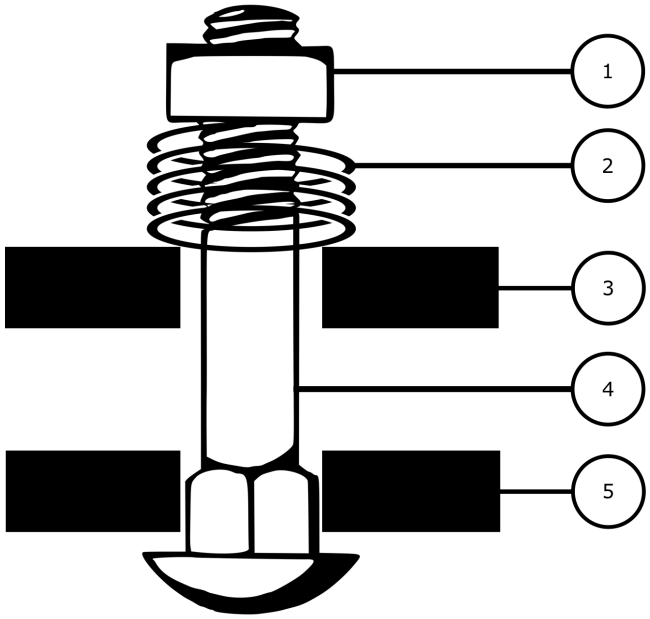

Figure 3.5: A simple representation of the clamping mechanism used to put force on the cell.

Table 3.3: Naming of the components of the clamping mechanism.

Number [#]	Description
1	Tightening nut
2	Spring
3	Lower inconel housing
4	Bolt
5	Upper inconel housing

3.2.1 Electrical system

The cell is connected to the electrical subsystem via the housing and the platinum wires. The electrical subsystem consist of a DC power supply, a switch and an electronic load.
During electrolysis the power supply is directly connected to the cell, as shown in Figure 3.6A. The power supply used in this electrical system has a current and a voltage limiter build in. The current limiter on the power supply is used to keep a constant current during operation. This is done by setting the current limiter to the desired current value and by setting the voltage limit of the power supply to a relatively high value, 10 volts. With these settings the current limiter will always be met earlier than the voltage limit. This means that the current is kept constant, at the limit, whilst the voltages is allowed to fluctuate below its limit to maintain the current in the system. This

practice ensured the voltage could fluctuate for a certain constant current. This is important as the fluctuations in voltage could be monitored whereas the fluctuations in current could not.

In fuel cell mode an electrical load needs to be introduced in the circuit to dissipate the power produced by the cell. Unfortunately most electronic loads can not work with the high currents at low voltages that are produced by single cell SOFC systems. To increase the voltage supplied to the electronic load a voltage booster is used between the cell and the load. In the experimental setup the dc power supply was used as a voltage booster when the cell was operating in fuel cell mode. This system is displayed in Figure 3.6B. During operation the dc power supply the voltage is set to 10 volts, which means the electronic load is supplied with a voltage of 10 volt plus the voltage of the cell. To set and maintain a current in the circuit, the electronic load can be set to a user specified value. The electronic load then regulates its internal resistance to maintain the set current value.

To switch between the electrical circuits a changeover switch was used, as shown in Figure 3.6C. The build in switch is also equipped with an "OCV mode" position, where the electrical circuit is interrupted, blocking electron flow. In Figure 3.6C the switch is in this state. When the mode is switched from fuel cell to electrolysis or vice versa, the polarity of the power supply has to be switched. This could be done using an high current rated H-bridge, however during the experiments the cables connected to the positive and negative connections of the power supply were swapped manually.

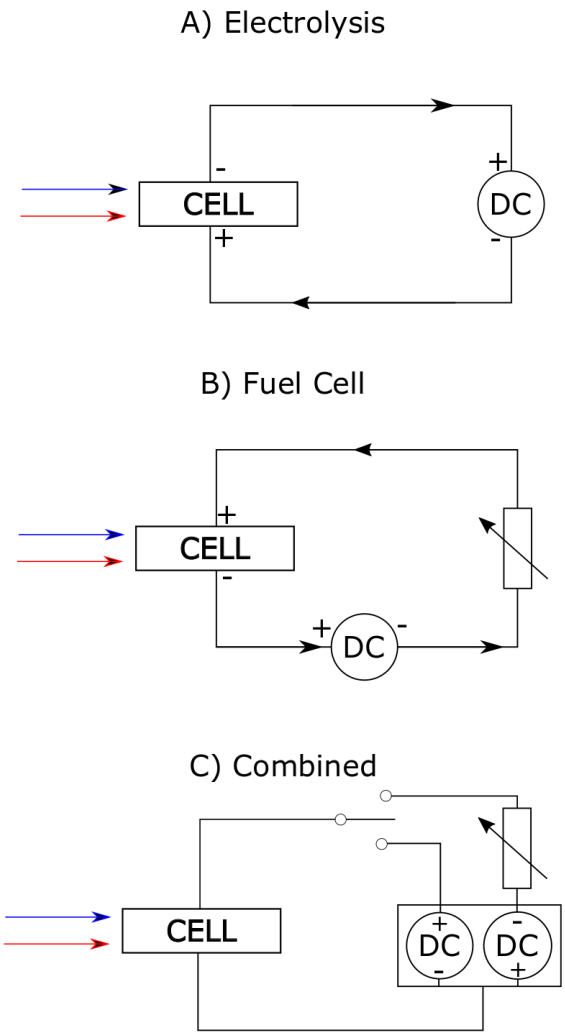

Figure 3.6: A simple schematic of the electrical connections of the ReSOC in electrolysis and fuel cell.

3.2.2 Mass flow inlet systems

As depicted in Figure 3.4 the cell receives mass flow on the fuel side and air side with a single duct for each side. To supply the air for the air inlet on the cell two mass flow controllers are used. One mass flow controller controls the oxygen flow the other one controls the nitrogen flow. To mimic the air around us, the oxygen and nitrogen are mixed in a ratio of 21%-79% respectively. Mixing is done by connecting the ducts coming from the mass flow controllers with a t joint to an single duct going towards the cell.
The fuel inlet mass flow control is more complicated as fuel cell and electrolysis modes need different fuels. In fuel cell mode the cell receives dry hydrogen gas, which is a mixture of 50%

hydrogen and 50% nitrogen. The flow rates of these gasses are controlled by separate mass flow controllers and are mixed the same way as the air side flow. During electrolysis the cell operates with a fuel inlet flow of 50%-40%-10% mixture of nitrogen,water and hydrogen respectively. The nitrogen and hydrogen mass flows are still controlled by the mass flow controllers mentioned before. Supplying the water to the inlet is more challenging as water is in liquid phase at ambient conditions. This means that a system has to be put in place that can supply the water in liquid form into the inlet duct and evaporate the water before it reaches the cell. To supply the liquid water a peristaltic pump, Longer bt100-2j, is used in combination with an needle to inject the liquid into the inlet duct. This liquid water injection system is discussed in more detail in the next section.

3.2.3 Original water injection system

The water injection system can be divided into two objectives. The first objective is to supply the heat energy for the vaporisation of water. The second objective is to create a continuous flow of water vapour.
During experiments the required water mass flow is between 2.12 and 5.32 milligrams per second. This means that, if the water is supplied at 25 degrees Celsius, it takes between 5.5 and 13.7 Watt to evaporate the water mass flow to steam. This is calculated using an enthalpy of 104 kJ/kg at 25 degrees and 2677 kJ/kg at 101 degrees Celsius, at atmospheric pressure. Even the higher of the two energy numbers is low compared to what most electrical heaters can supply, which is in the order of a factor 10 to 20 higher. This implies that the challenge for this system is not supplying the total energy requirement, but rather the transfer of the energy to the water.

If the flow rates are low enough adhesion and surface tension become important forces. These forces cause the water to form droplets at the end of the injection needle, rather than creating a continuous stream. This is the second part of the water injection system, creating a continuous flow of water. A common trick to get water flowing steadily at low mass flows from a needle is to let it trickle down a solid object. This can be done by making the needle come in contact with a solid surface, such as the inner wall of the inlet duct, or a cartridge. The "cartridge" is a bundle of ceramic wires, as displayed in Figure 3.7. If the water injection needle is inserted into this cartridge water can trickle down these strands of ceramic wire.

Figure 3.7: The cartridge displayed in a fuel inlet duct.

The original water injection system is depicted in Figure 3.8. In Table 3.4 the components of the water injection system are named. The red arrow depicts the incoming hydrogen and nitrogen flow that is required for electrolysis, as specified in Table 3.1. For simplicity the thermocouple temperature sensor that is inserted through the cartridge is not shown in the figure below.

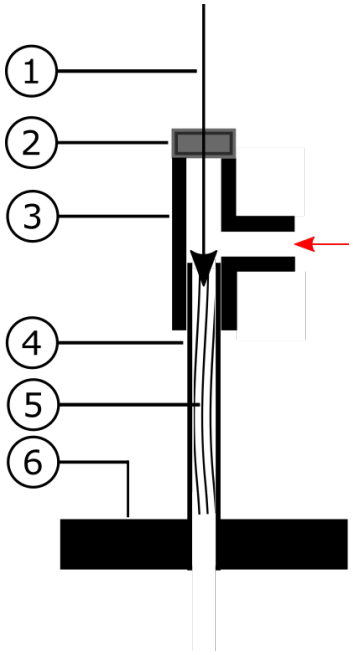

Figure 3.8: The original water injection system

Table 3.4: Naming of the components of the injection system.

Number [#]	Description
1	Liquid water injection needle
2	Rubber seal
3	T joint
4	Inlet duct
5	Ceramic cartridge
6	Lower inconel housing

The performance achieved with this setup is displayed in Figure 3.9. The performance of the water injection system is measured with the voltage fluctuation, where lower fluctuation is better. To be able get a fair comparison between two injection systems, the first hour of electrolysis during the constant current operation is compared. The figure below therefore, shows the voltage measurements during the first hour of constant current electrolysis operation at 0.5 A/cm^2. The graphs are made by voltage measurements taken at three seconds intervals. The average value of the voltage measurement in this graph is not of importance when comparing water injection systems. The fluctuation in these graphs is more important because incomplete evaporation and noncontinuous water supply will show up in the voltage graph as fluctuations.
The figure below shows little fluctuation, approximately 5 millivolt, between hours 59.2 and 59.8.

However the graph shows two spikes in voltage of 40 and 25 millivolt. This behaviour was present throughout electrolysis testing with this injection system. The fact that the cell voltage after the spike is slowly decreasing over 45 minutes rather than decreasing to the normal value within a couple of measurements, is indicative of a bigger problem. This indication of a problem is amplified by the breakage of the ReSOC cells after relatively short use in this setup. This is shown in Figure 3.10. Multiple cells have been tested with this setup and all cells show cracks that originate from the center of the cell.
It is assumed that the problems stated above are caused by droplets of water which reached the cell electrode. If a water droplet reaches the cell it will evaporate quickly to steam, creating a high concentration of water on the cell electrode area. The increase in water concentration explains the spike down in voltage, due to the decrease in Nernst potential and the decrease in activation and concentration overpotentials, shown in the equations in Section 2.1.3. Once the (excess) water mass is exhausted from the cell, the operational voltage is expected to return to the values seen before the spike as the Nernst potential and the activation and concentration overpotentials return to the values before the droplet. However, rather than a return to the operational voltage measured before the spike, a spike up in voltage and a gradual return is seen. This spike in voltage is caused by the evaporation of water on the electrode surface. Due to the evaporation, heat is contracted from the cell by the water. This contraction of heat locally lowers the cell temperature. The subsequent gradient in cell temperature can cause the cracks in the cell, as explained in Section 2.2. The crack would start in the center of the cell, as the gradient is largest where the droplet evaporates. The local decrease in cell temperature explains the rise of voltage as well, due to worsened ion conductivity of the electrolyte. This worsened ion conductivity increases the ohmic overpotential, as shown in Equations 2.9, 2.10 and 2.11. When the cell starts heating up again the performance returns to its original level, as the ohmic overpotential decreases again due to the increase in temperature. This gradual decrease in operational voltage can be seen in the graph of Figure 3.9. Other degradation mechanisms such as, clamping pressure, manufacturing defects, poisoning and delamination could be ruled out by later experiments as they showed no cracks with the same operational parameters and a different water injection system.

This problem of cell breakage within short use of the cell led to the development of a new water injection system along with a new inlet duct. This development was started as the setup could not determine the experimental objectives specified in Section 3.1, as the breaking of the cell shortly after electrolysis significantly influenced the results.

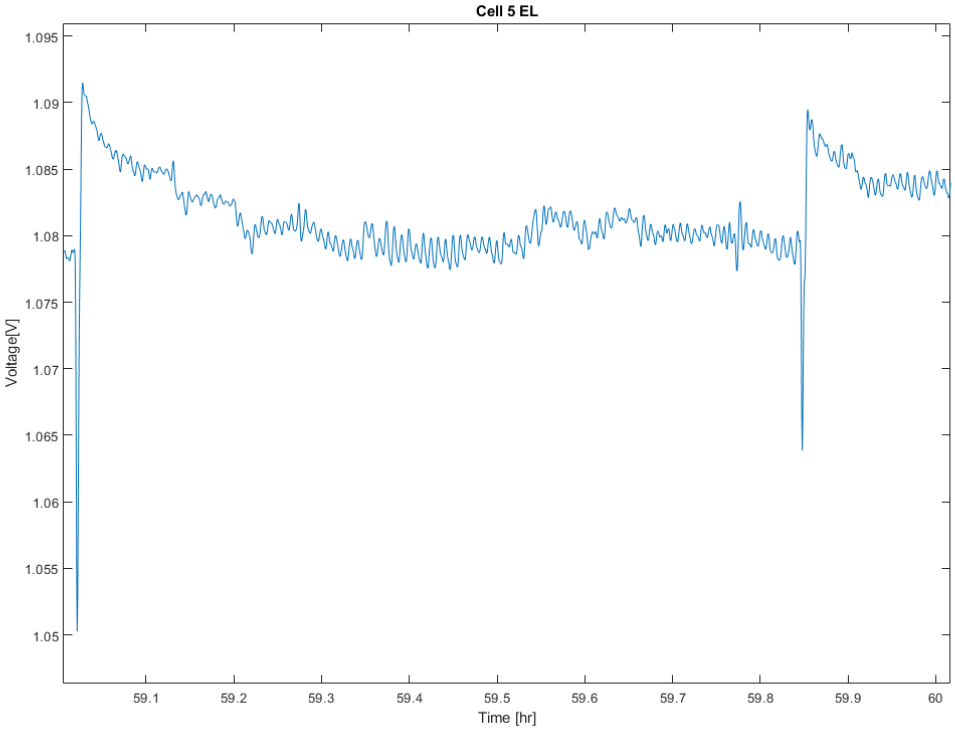

Figure 3.9: Voltage fluctuations during electrolysis with the original system

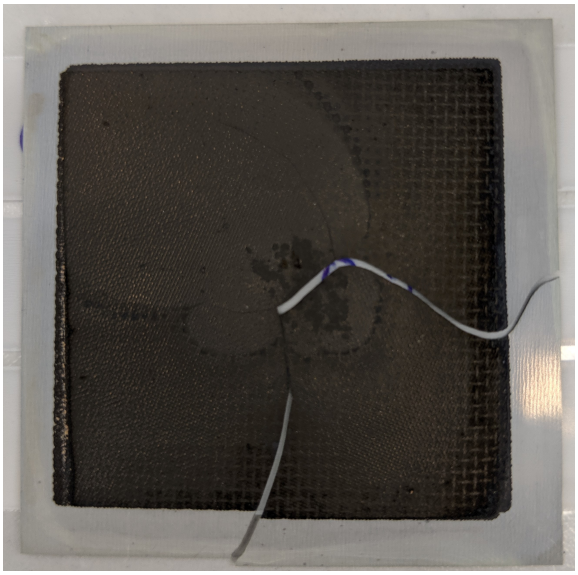

Figure 3.10: Cracked cell.

3.2.4 Measurement uncertainty

As this thesis uses measurements from an experimental setup to determine cell and water injection system performance, it is important to mention the uncertainties that are introduced by the measurement devices. The measurement specifications are taken from their respective operating manuals unless stated otherwise.

3.2.4.1 Voltage

The Gamry 600 measurement system is used for the voltage measurements. This is the only device that recorded data it was measuring automatically, all other data is recorded manually. The data logging frequency was set to 3 seconds. The specifications of this measurement system are stated in the table below. The measurement device has an maximum operating temperature of 45 degrees Celsius, during testing it never exceeded these temperatures however the device did reach 40 degrees Celsius at various points. These temperature fluctuations influence the measurement results, however according to the manufacturer's manual this does not have to be taken into account when only measuring voltage.

Table 3.5: Measurement specifications for the Gamry 600.

Name	value	note
A/D full scale ranges	$\pm$12.0 [V]	typical
Resolution	400 [μV/bit]	typical
Zero offset error	1 [mV]	maximum
Gain error	0.2 [%]	maximum
Offset range	$\pm$10 [V]	typical

3.2.4.2 Current

Current measurements are taken with two different devices. In fuel cell mode an electronic load, Kikusui PLZ153W, is used. Apart from the measurement specifications in Table 3.6, it was noticed that the electronic load could drift $\pm$0.05 ampère over a time period of 3 hours.
During electrolysis the SM30-100D power supply did not only provided the power for the cell but also functioned as a current sensor and controller. The remaining specifications for this device are given in Table 3.7.

Table 3.6: Measurement specifications for the Kikusui PLZ153W.

Name	value [unit]
Operating range	0-30 [A]
Operating range	1.5-120 [V]
Setting accuracy	$\pm$0.3% + 30 [mA]
Setting resolution	8 [mA]
Ripple noise	30(@ 30A) [mA]
Stability	10 [mA]

Table 3.7: Measurement specifications for the SM30-100D powersupply.

Name	value [unit]
Operating range	0-30[V]
Operating range	0-100[A]
Setting resolution	0.03 [%]
Accuracy	0.5[%]

3.2.4.3 Temperature

As the measurement specifications for the thermocouples used in the setup were not found in the manufacturer data sheet, the accuracy of the type K and type N thermocouples are both estimated to be $\pm 0.75\%$. According to the website of Pico Technology, these are typical values. The temperature sensors were calibrated to an internal standard.
The oven temperature sensor gave a reading which was 10 degrees Celsius lower compared to the reading from the thermocouples, at a temperature of 700 degrees Celsius. Recalibration of the oven temperature sensor was not possible and therefore the temperature reading from the thermocouples was used to set the over temperature.

3.2.4.4 Mass flow

A synsodyne Gilibrator 2 is used to calibrate the Bronkhorst mass flow controllers, of the EL-Select product range, to ± 2 millilitres per minute of the desired flow rate. The accuracy of the Gilibrator is given by the manufacturer as "better than 1%".
The peristaltic pump can be adjusted between 0.1-100 rpm with steps of 0.1 rpm. To calibrate the pump a measuring cylinder combined with a stopwatch is used. This means that the accuracy and precision of this device is unknown. To prevent the uncertainty to cause a water mass flow shortage, the mass flow was set 2.5% higher than required. This figure is based on previous experimental work.

Chapter 4

Water injection system optimisation

The problems described in Section 3.2.3 impose an uncertainty on the i-v curve measurements. This uncertainty comes from the fact that an i-v curve measurement taken at different times will give different results with the original water injection system. This time dependence of the measurement is shown in Figure 3.9. From this figure it becomes clear that, for example, an i-v curve taken between 59 and 59.2 hours will give a different result than if an i-v curve measurement is taken at 59.6 to 59.8. This could be negated by taking multiple i-v curve measurements. However as the Balance project studies the loading and unloading of a solid oxide cell, taking more i-v curve measurements will interfere with the results, as taking multiple i-v curve measurements will load and unload the cell.
Another problem described in Section 3.2.3 is that the solid oxide cells tested with the original water injection system lost most performance relatively fast and all the cells cracked within short use. To study the long term degradation effects of cyclic operation of a solid oxide cell, a change in the experimental setup is required to prevent the reoccurring cell damage and extend the experiment duration. As the assumption is that liquid water could reach the cell, as explained in section Section 3.2.3, the water injection system is redesigned.

In this chapter the design process used to produce the new injection system is described. For the redesign a design constraint was imposed. This constraint was that the peristaltic pump and injection needle were to remain part of the system. This restriction was imposed as alternatives could not be purchased, delivered and incorporated into the system within the given time frame.

4.1 Evaluation of evaporation mechanism

Firstly the function of the cartridge is examined as this part plays a crucial role in the evaporation process. Without the cartridge inside the inlet duct the injection needle would be suspended in mid air. From experiments it was determined that at a flow rate of 0.128 millilitres of liquid water per minute, the needle would release a droplet every three seconds. After the droplet is

released from the needle, it needs to be evaporated via heat transfer of the energy originating from the inlet duct walls. To give an overview of the situation, a thermal circuit is drawn up in Figure 4.1.

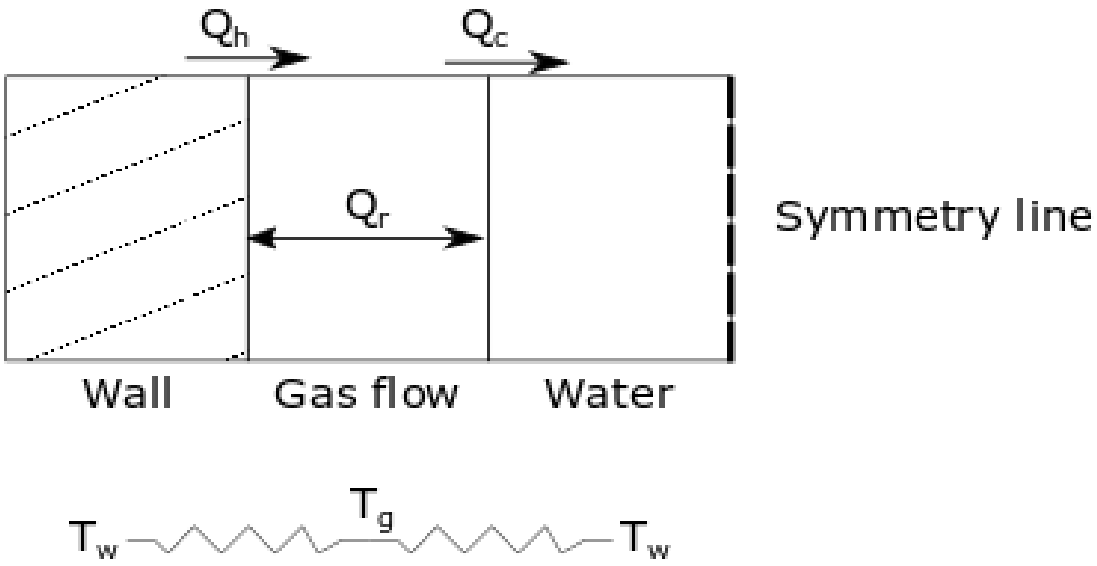

Figure 4.1: Schematic overview of the conduction problem with thermal circuit equivalent below.

The frame of reference used for the heat energy transfer equations in this section is chosen as shown in Figure 4.2. Where the dashed line shows the frame of reference, the sphere in the middle depicts the water droplet and the wavy lines depict the inlet duct walls. This choice of frame of reference determines the surface areas of the wall, inlet duct and also the mass of the droplet in the equations as the frame of reference ends at the symmetry line, shown in Figure 4.1. The frame of reference is chosen to move with the droplet, as this is the object that is studied in this section. This, combined with the assumption that the gas in the reference frame has the same velocity as the droplet, means that only the walls move relative to the frame of reference.

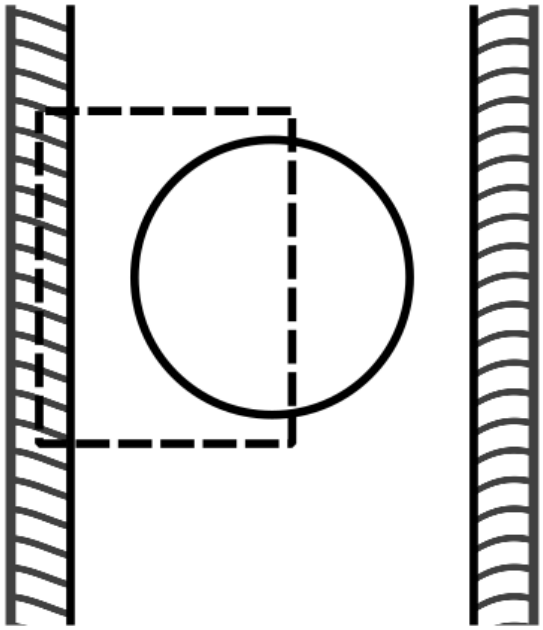

Figure 4.2: Frame of reference.

To calculate the heat transfer from the (assumed) uniform wall temperature to the gaseous layer Equation 4.1 is used. In this equation h_c is the heat transfer coëfficient, ΔT the temperature difference, A the contact surface area, k the thermal conductivity of the material and D the thickness of the layer. The heat transfer coëfficient,h_c, is estimated with Equation 4.2, as the wall temperature is assumed uniform [62].
The droplet is assumed to travel at the same velocity as the gasses. This assumption means that the heat transfer from the gaseous layer to the droplet is calculated with the heat conduction equation, shown in Equation 4.4, rather than the convection equation. In the heat conduction equation L is the characteristic length, in this case the radius of the droplet.
The radiation heat transfer between the wall to the droplet is calculated with Equation 4.3. In this equation the ϵ is the emissivity coëfficient and σ is the Stefan-Boltzmann constant. In the equation it is assumed that only the wall inside the frame of reference irradiates the droplet, that the gaseous layer can be neglected and that the view factor is equal to 1 from the wall to the droplet and vice versa.
For all equations it is assumed that all layers have uniform properties at all times and the properties of the species needed for the calculations are obtained from the program Refprop.

$$Q_h = h_c * \Delta T * A \tag{4.1}$$

$$h_c = 3.66\frac{k}{D} \tag{4.2}$$

$$Q_r = \epsilon\sigma T^4 A \tag{4.3}$$

$$Q_c = \frac{\Delta T * k * A}{L} \tag{4.4}$$

$$\Delta h = \frac{\Delta Q \delta t}{m} \tag{4.5}$$

Table 4.1: Values for the variables in Equations 4.2, 4.1, 4.4 and 4.5

Variable	value [unit]	description
T_w	573 [K]	Wall temperature
T_g	298 [K]	initial gas temperature
T_d	298 [K]	initial water temperature
D	0.005 [m]	diameter of inlet duct
m_w	2.1457e^{-6} [kg]	water mass in droplet
m_g	1.494e^{-8} [kg]	nitrogen and hydrogen mass in reference frame
A_g	1.57e^{-5} [m^2]	surface area from wall to gas
A_w	6.4 e^{-6} [m^2]	surface area from gas to droplet
δt	0.001 [s]	time step in seconds
ϕ	365 [ml/min]	total gaseous flowrate
σ	5.670e-8 [W/m^2K^4]	Stefan-Boltzmann constant
ϵ	0.8& 0.95	emissivity coëfficient of stainless steel and water

To find the time it takes to evaporate a droplet Equation 4.5 is used. In this equation the δt is the time step and ΔQ the net energy difference in a layer and m is the mass in the layer. With the equation the the change in enthalpy for each of the layers in the thermal circuit is calculated. Using the program Refprop the enthalpy of a layer can be converted to temperature and for the water layer to vapour quality, given that the pressure is atmospheric. Using the Euler forward method of solving the system of equations mentioned above and the values from Table 4.1, it was determined that it takes approximately 55 seconds for the water in the droplet to vaporise. This evaporation time means that a 13.5 meter long inlet duct is needed to evaporate the water droplet. The length is calculated with the average velocity of 0.24m/s.
In contrast, if the water droplet and gas flow switch places in the thermal circuit, it takes only 5 seconds to evaporate the water. For this calculation the radiation is neglected. This result illustrates the working principle of the cartridge. It brings the liquid water in contact with high temperature surfaces, which maximises heat transfer to water by increasing the thermal conductivity and surface area whilst minimising the characteristic length.
To validate this calculation, two water injection systems were trialled without a cartridge installed. In these experiments the inlet duct was extended to 1 meter and to 3 meters, both with wall

temperatures heated to 300 degrees Celsius. From the results in Figures 4.3 and 4.4 it becomes apparent that in both systems still a lot of voltage fluctuation is present. This fluctuation in voltage means that the water was not converted into vapour form in a continuous manner because the heat transfer rate is too low. Both systems did have a p-trap duct design before the cell inlet to prevent liquid water to enter the cell.

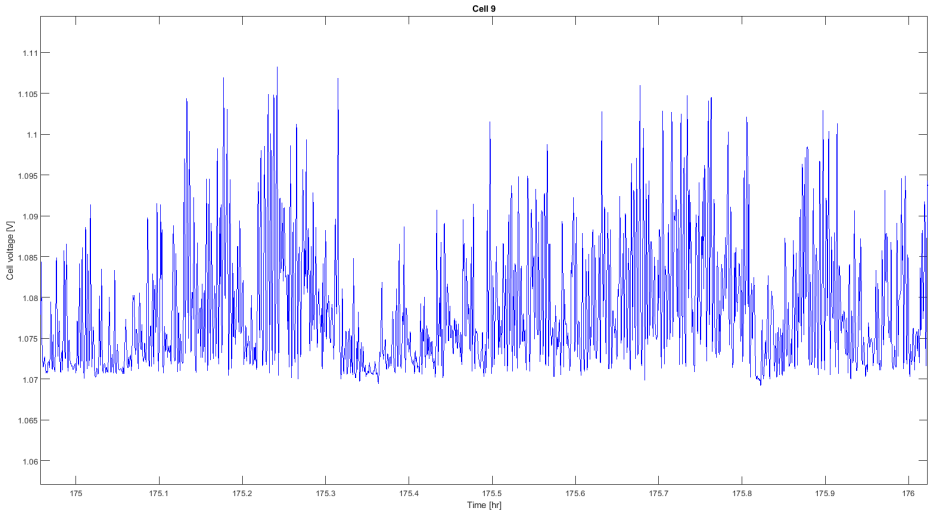

Figure 4.3: Voltage fluctuations during electrolysis with an elongated inlet duct of 3m meters.

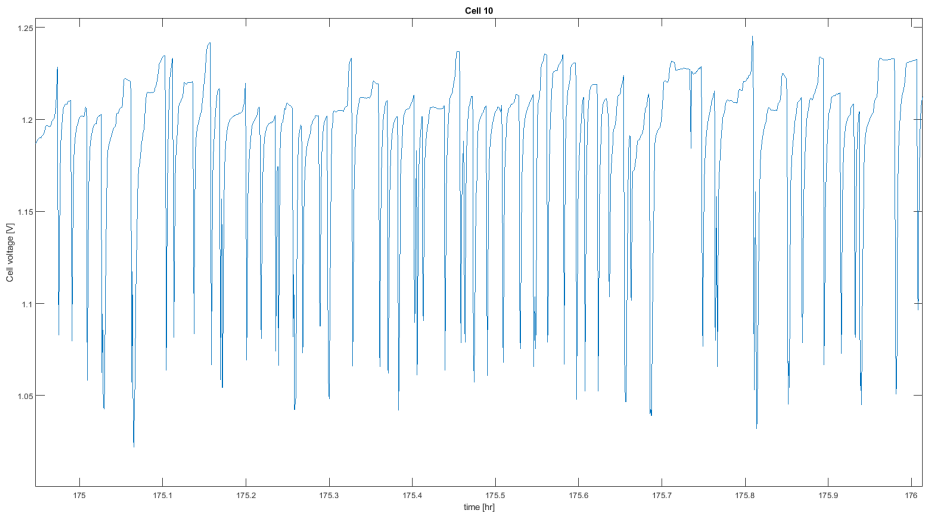

Figure 4.4: Voltage fluctuations during electrolysis with an elongated inlet duct of 1m meter.

The reason for this long evaporation time without cartridge is the thermal conductivity of nitrogen gas. At only 0.025 W/m-K nitrogen acts as an insulator. By inserting the cartridge inside the inlet duct a large surface area at high temperature with a low characteristic length is created, assuming the cartridge is in contact with the inlet duct wall. With the cartridge in place the water is dispersed and can come in contact with this large high temperature surface area of the inlet duct walls and the cartridge. With a thermal conductivity of 0.6 W/m-K liquid water conducts energy significantly faster than nitrogen.
The, assumed, reason why the original design showed signs of liquid water reaching the electrode surface even tough a cartridge was used, is that the thermocouple interfered with the working of the cartridge. When a thermocouple is inserted into the cartridge it creates a discontinuity in the center. Water can trickle down the sensor where a nitrogen layer can insulate it from the cartridge. This is depicted in Figure 4.5. This water can build up on the end of thermocouple and reach the the cell electrode from there, as seen in Figure 3.9. Because inlet and outlet temperature data is important for modelling, removing the thermocouple from the inlet duct is not an option, however relocating the water injection point is.

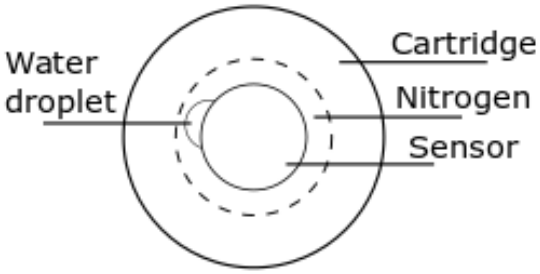

Figure 4.5: Insulating effect of a sensor in the middle of the cartridge.

4.2 New water injection system design

In the previous section it is shown that placing a cartridge inside the inlet duct at the liquid water injection point significantly reduces the inlet duct length required to evaporate the injected water. This is the reason why the cartridge is retained for the new injection system. The previous section also shows that the working principle of the cartridge can be disrupted by inserting a device through the middle. The redesign therefore focuses on finding a solution to incorporate both a temperature sensor at the cell inlet and a cartridge without causing interference.

The solution was found by relocating the water injection point from the cell inlet, as seen in Figure 4.6. The choice to relocate the water injection point rather than the temperature sensor is based on the fact that the water does not need to be evaporated close to the cell inlet. The water can be evaporated earlier, as long as the water does not condenses back to the liquid phase. The cell inlet temperature sensor does need to be close to the cell inlet, as temperature measurements outside the oven do not account for the preheating done by the oven.
With the injection point moved to the top right in the figure, more space is created between the cell inlet, and thus the temperature sensor, and the water injection point. This extra space allows the 30 centimeter long cartridge to sit clear of the temperature sensor at the inlet. In Figure 4.6 the temperature sensor enters the inlet duct vertically where the duct makes a 90 degree turn, which is a distance away from the end of the cartridge.
With the placement of the water injection point to the top right the inlet duct becomes angled, rather than going straight down. This angle allows buoyancy forces to effect the mass flow. As the density of liquid water is a factor of 1000 to 2000 bigger than that of nitrogen, water will sink to the bottom of the inlet duct and nitrogen and hydrogen rise to the top. With the buoyancy forces forcing the gases up, the concentration of liquid water will be relatively high on the bottom, aiding better thermal conduction to the liquid phase water as the insulating nitrogen gas is separated from the water. After the cartridge the duct makes a 90 degree turn down and travels towards the cell. This part is preheated by the oven and is where the thermocouple resides for inlet temperature measurements, as was the same in the original setup.
As the water injection is relocated away from the oven the inlet duct wall needs to be actively heated. This is done with a one meter long trace heating cable that can operate at a maximum of 400 degrees Celsius and deliver 100 W/m of energy. The heater is wrapped around the half a

meter long inlet duct that contains the cartridge. As the total energy needed to heat the entire mass flow in the inlet duct up from 25 degrees to 300 degrees Celsius is between 7,5 to 19,2 watts, depending on the mass flow rates, the trace heating cable can supply more than the system needs. During the experiments the trace heating cable heated the outer wall of the inlet duct to 325 degrees Celsius. Experiments showed that this temperature produced the lowest fluctuations during the voltage measurements.

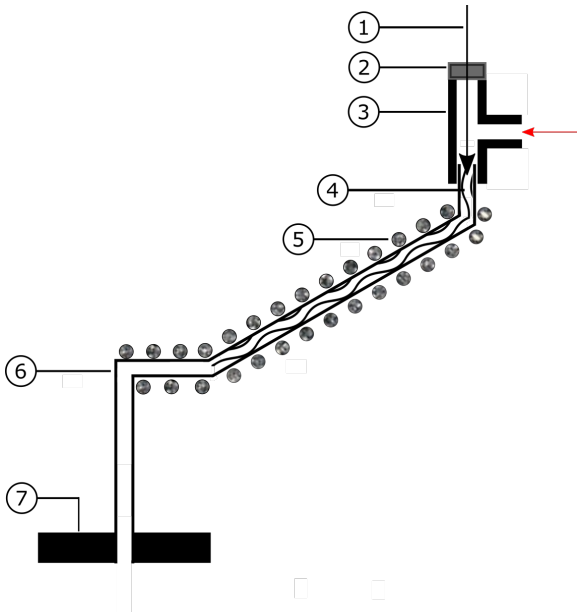

Figure 4.6: The redesigned water injection system

Table 4.2: Naming of the components of the evaporator.

Number [#]	Description
1	Liquid water injection needle
2	Rubber seal
3	T joint
4	Ceramic cartridge
5	Heating wire
6	Inlet duct
7	Lower inconel housing

4.3 Validation of design

The results with the new water injection system are shown in Figure 4.7. Fluctuations have decreased from 5 millivolt to 1.5 millivolt, which is a reduction of 70%. This result indicates that a good continuous water vapour flow is created. More notably the big spikes have been removed, confirming that the water is now fully evaporating before entering the flow distribution plate, or lower inconel housing. With the fluctuations reduced and the spikes removed the reliability of an i-v curve measurement increased.
Due to the full evaporation of water the cells no longer break within short use and the degradation has been reduced. Experiments with the redesigned water injection system have been verified to last up to 1000 hours of continuous operation, where as the experiments before lasted less than 200 hours. A cell after 800 hours of operation is shown in Figure 4.8. The figure shows some damage on the air electrode, attributed to a air inlet duct failure, but more importantly it shows that the cell is still in one piece. These results mean that the experiment duration is no longer limited by the water injection system but by the performance of the cell and the experimental protocol. This in turn means that the test station with the redesigned water injection system, can be used to study long term degradation due to cyclic operation.

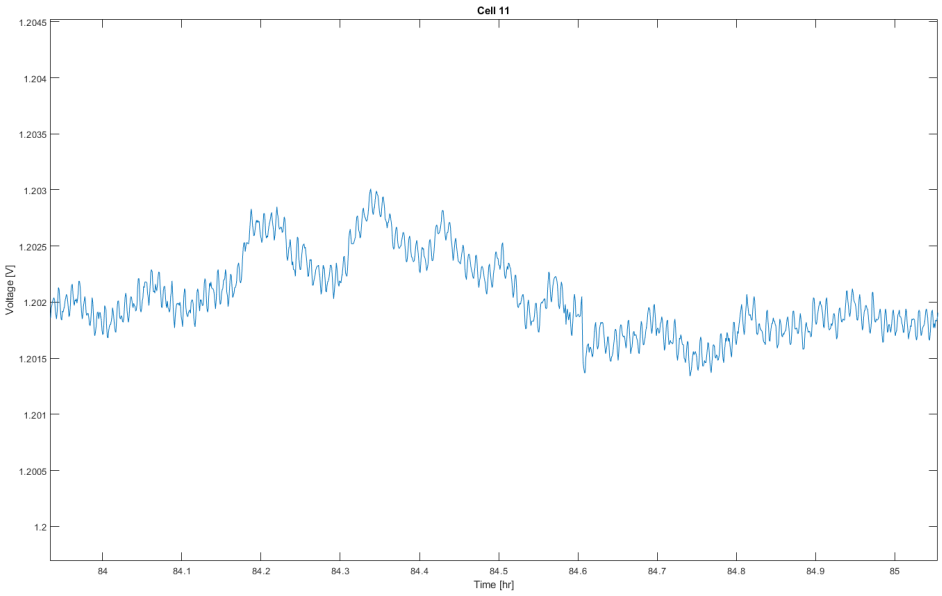

Figure 4.7: Voltage fluctuations during electrolysis with the redesigned injection system.

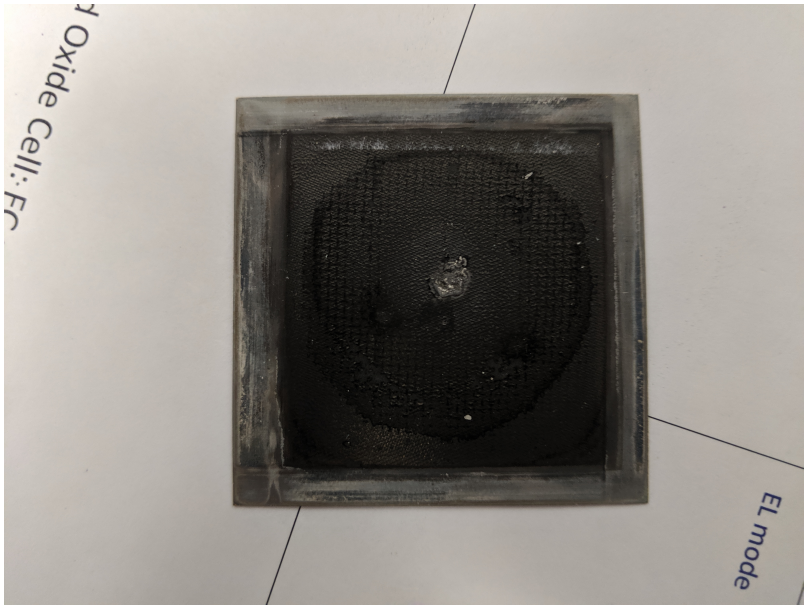

Figure 4.8: Cell after 800 hours of operation with the redesigned injection system.

Chapter 5

Fuel flow distribution model

In Figure 5.1 two things stand out. The first thing that stands out is that the cell is cracked, which is addressed in previous chapters. The second thing that is remarkable is that there are markings on the cell. The colour of the markings on the cell are in a spectrum between gray, the colour of nickel, and bright green, the colour of nickel oxide. This indicates that the markings are due to different oxidation gradients of the fuel electrode. Oxidation of the fuel electrode occurs during operation if the oxygen ions transported through the electrolyte do not react with hydrogen but with the nickel fuel electrode instead. As the oxidation rate of the fuel electrode also depends on the (local) amount of hydrogen, these markings can be indicators of the fuel flow pattern on the fuel electrode.
If these markings indicate the fuel flow pattern across the cell, the flow distribution in the test station differs significantly from the uniform flow distribution shown in Figure 2.8. The non-uniformity of the flow distribution can cause temperature fluctuations in the cell, due to differences in convective heat transfer from the cell to the fuel stream, and it can cause fluctuations in current density due to differences in local concentrations of reactants. This difference in local concentrations of reactants can, in extreme cases, cause (local) fuel starvation. These effects can influence the experimental results, by for example introduce temperature gradients or fluctuations, concentration differences which effect overpotentials and in extreme cases it can cause the nickel in the fuel electrode oxidise and reduce cyclically [58].

Figure 5.1: Marks on the fuel side of the ReSOC which indicate a flow pattern.

In this chapter the hypothesis, that the cell performance measurements are effected significantly by the fuel flow distribution, is evaluated. This evaluation is done by firstly confirming that the markings on the fuel electrode are indicative of the fuel flow distribution with a 2 dimensional (2D) CFD analysis. With the streamlines resulting from the CFD analysis, a conversion model is made. This model uses the CFD data to calculate local current density and fuel utilisation across the cell.
To finally to evaluate the hypothesis the data resulting from the CFD analysis of the test station is compared to a more ideal flow that is usually found in literature, as described in Chapter 2. To simplify the naming of the two models, the flow distribution in the test station will be referred to as the setup case, the flow distribution derived from literature will be referred to as the ideal case.

The choice to make a standard CFD analysis of the fuel flow and produce a program that converts the streamline data to current density and fuel utilisation data, is based on time constraints. As, at the time of writing, add-on modules for CFD programs lack proper support and the SOFC/CFD models from literature are difficult to reproduce, it takes a long time before a model made with a CFD add-on module produces acceptable results. It is not unusual that it takes up to 6 to 9 months to get acceptable results with these kinds of models, based on personal correspondence with professionals in this particular field. Because the goal of this model is to evaluate the hypothesis stated above, a less detailed model can be used to save time. As a model with less detail contains more assumptions, the effects of these assumption will be discussed in Chapter 7.
Because of the time constraints the model will focus solely on the fuel electrode during fuel cell operation. The choice to focus on the fuel side was made on the basis it that it is the fuel electrode where the markings where seen. Furthermore, imperfections of the flow distribution on the air electrode can often be more easily compensated for. This can be done by, for example, opening the flanges or by increasing the volume flow.

5.1 2D flow analysis

For the fuel flow analysis, a 2D flow model is made of flow area above the fuel electrode. The choice to go with a 2D rather than a 3D simulation is based upon the fact that the height of the flow area in this setup is between a factor of 20 to 80 lower than the length of either axes of the cell and that the computational time is longer for 3D simulations compared to 2D simulations. A drawback of 2D simulations in this case is that the entrance effects of the inlet and outlet are neglected. These entrance affects happen as the incoming flow is turned perpendicular to the flow direction in the duct when it enters the flow distribution area. To neglect these entrance effects the inlet line, from where the mass enters the model, is drawn as the outer diameter of the inlet duct. The outlets are treated the same way as the inlets. This allocation of the inlet and outlets, mean that the surface area of the inlet and outlet ducts is omitted from the CFD anlysis, which will have an impact on the model converting CFD data to current density and fuel utilisation data later on. The choice to set the inlet and outlets as the outer diameters of their respective ducts is thus chosen to Balance the effect on the conversion model and the assumption to neglect entrance effects.
The CFD meshes were made using a meshing program within the Ansys Workbench program, the calculations were done using the Ansys Fluent 19.0 program. In this section the Mesh and model settings that were used in the CFD model are discussed. If a particular setting is not mentioned in this section it is left at the default setting.

5.1.1 Mesh settings

Drawings of models used in the CFD are displayed in Figures 5.2, with the dimensions in Table 5.1. A normal drawing was used rather than a technical drawing for ease of reading. Both these models have a total length and width of 40 millimeter. Meshes of these models are made using the settings displayed in Table 5.2 and are shown in Figure 5.3 and 5.4. The choice to forgo inflation layers at the boundaries is that the mesh elements are small enough that implementing inflation layers does not improve the solution or the residuals significantly.
The choice to use triangle mesh elements over quadrilateral elements is that for the same element size, which is measured as the characteristic length, a triangle has a lower surface area. This means that there are more nodes on the flow area and as the nodes will be used later on for graphing the results, a higher node count leads to a higher resolution.

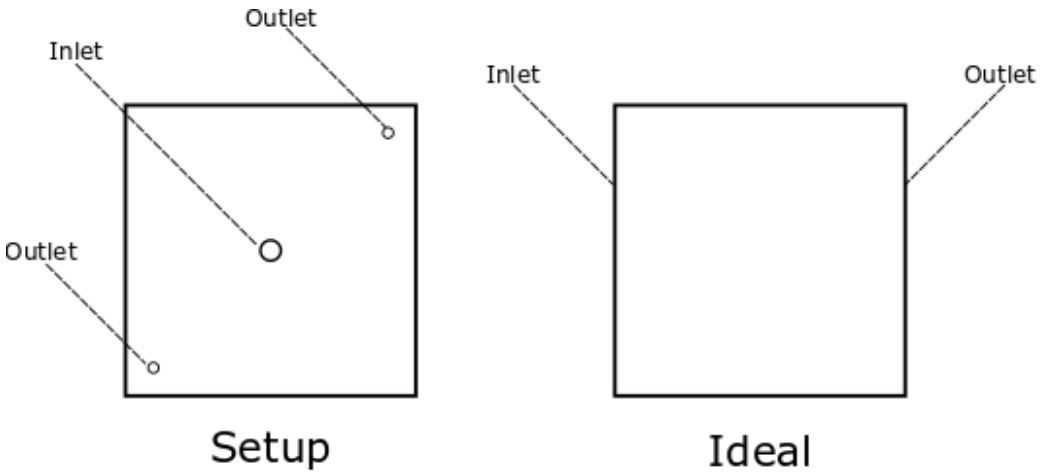

Figure 5.2: Drawing of the 2D models used for CFD.

Table 5.1: Dimensions of the model

Variable	Value [unit]
Total length	0.04 [m]
Total width	0.04 [m]
Setup inlet diameter	3.15 [mm]
Setup outlet diameter	1.7 [mm]
Setup distance between inlet and outlet	20.75[mm]

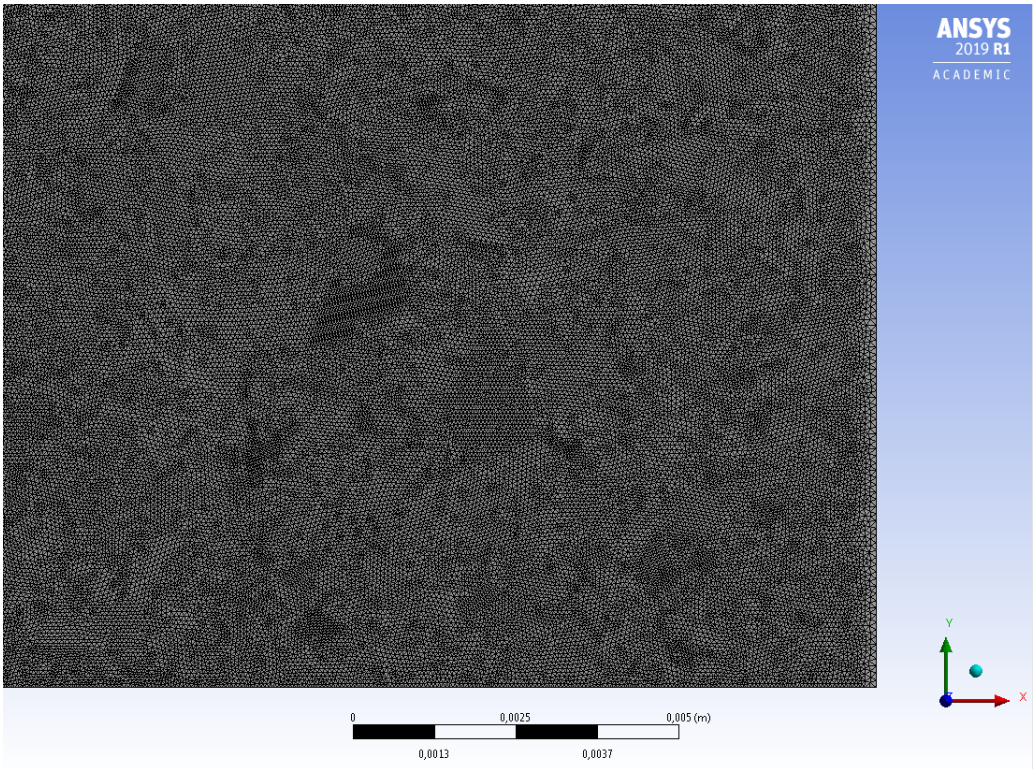

Figure 5.3: The mesh in the bottom corner of the outlet of the ideal case model.

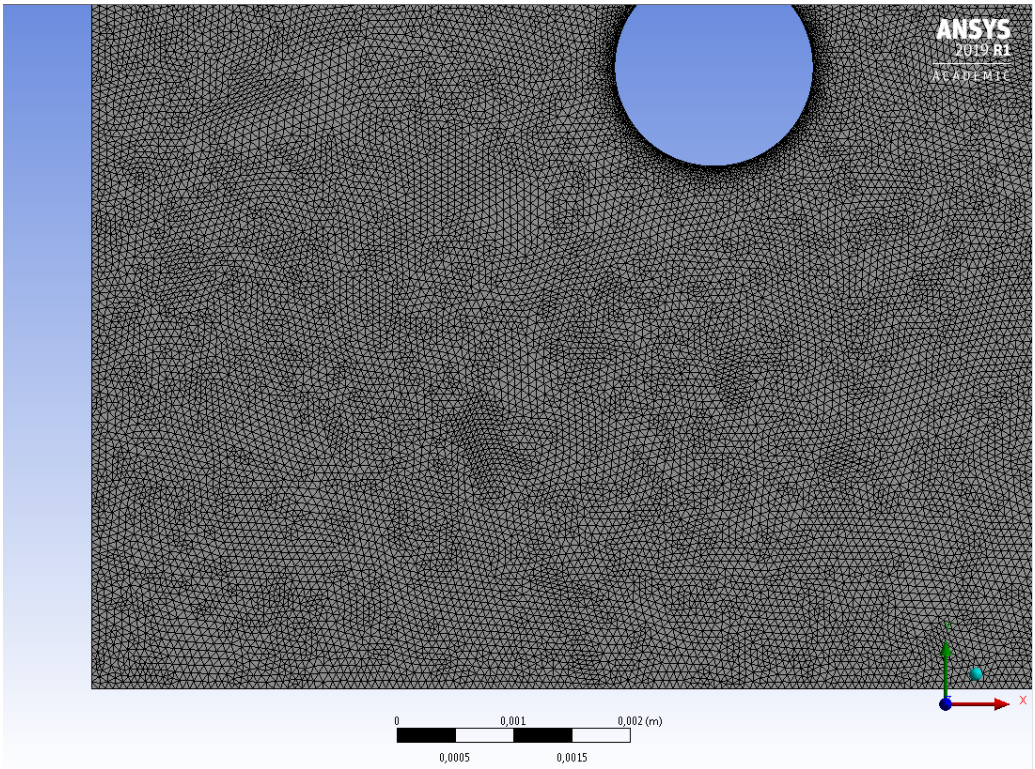

Figure 5.4: The mesh in the bottom left corner of the outlet of the setup case model.

Table 5.2: Mesh settings

Setting	for ideal case	for setup case
Mesh method	all triangles	all triangles
Element size	$6e^{-5}$[m]	$6e^{-5}$[m]
inlet and outlet divisions	360	360
number of elements	923244	935516
number of nodes	462647	469630

5.1.2 Model settings

Within Ansys Fluent there are several models which the user can choose to use and modify. In this section these settings are discussed. If a particular setting or model it is not mentioned in this chapter it is left at the default setting.

With the two inlet flow conditions, which are determined by the Balance protocol, the inlet flow

velocity and the Reynolds number are calculated with Equations 5.2, 5.3 and 5.4. Using the values displayed in Table 5.3, the inlet velocity for the experimental setup is determined to be 1.08 meters per second and 2.7 meters per second for the low and high volume flow rate respectively. For the ideal case this is reduced, due to the larger inlet area, to 0.27 and 0.675 meters per second respectively.
The Reynolds number is calculated with Equation 5.4. This equation is used to determine Reynolds numbers for a flow in a duct, which means that the in this case the porous media is neglected in this calculation. Both these velocities led to a laminar flow as the Reynolds numbers vary between 10 and 300. These Reynolds numbers are far below the values that indicate the transitional region, which is around 2,100 [63]. This means the viscous model is set to laminar.
As the inlet flow contains hydrogen and nitrogen, the species model and therefore the energy equations are turned on in the CFD models menu. For this model the mass ratio of hydrogen and nitrogen at the inlet needs to be specified. This ratio is determined with Equation 5.5 to be 0.069. As there is no conversion, or leaks, in the CFD model the back flow at the outlet is also set to the same mass ratio. This helps with convergence if reverse flow at the outlet occurs. As the Pécelet numbers, calculated with Equation 5.1, are much higher than 1, mass transport is dominated by kinetics rather than diffusion [64]. This is calculated with the velocities (U) mentioned above, the length (L) was set to 20mm and to 40mm for the setup and the ideal case respectively and the diffusion (D) was taken from Section 5.2.2. As such diffusion is neglected in the model and the settings are turned off in the species model.

$$Pe = \frac{UL}{D} \tag{5.1}$$

As current collection on the fuel side of the cell happens through a nickel foam, this has to be taken into account as it has an impact on the flow. This nickel foam will be referred to as the nickel foam diffuser or just as the diffuser. To implement the nickel foam inside the CFD analysis, the flow region is set at a porous medium with the settings shown in Table 5.4. To be able to quantify the effect the nickel foam has on the performance of the cell a CFD analysis is done without nickel foam as well. This is done by setting the flow region set to fluid in the model settings.

$$\begin{aligned} A_{setup} &= 2 * \pi * R * H \\ A_{ideal} &= L * H \end{aligned} \tag{5.2}$$

$$v = \frac{\dot{\phi}}{A * 6e^{7}} \tag{5.3}$$

$$Re = \frac{v * D_h}{\nu} \tag{5.4}$$

$$Ratio = \frac{\rho_h}{\rho_{h2} + \rho_{n2}} \tag{5.5}$$

Table 5.3: Model settings

Variable	description	Value [unit]
$\dot{\phi}$	volume flow rate	320 & 800 [ml/min]
H	height of flow area	0.0005 [m]
L	length of inlet	0.04 [m]
R	radius of inlet	0.001575[m]
D_h	hydraulic diameter	0.001 [m]
ν	kinematic viscosity	0.00017356 [Pa s]
ρ_h	Density hydrogen (1000K)	0.0246 [kg/m^3]
ρ_n	Density nitrogen (1000K)	0.331 [kg/m^3]

To simplify the case studies the temperatures are assumed constant, as will be done in the conversion model. The Balance protocol prescribes that experiments which are done with a 320 ml/min inlet flow rate are operated at 1023Kelvin, experiments with a higher inlet flow rate operate at 973 Kelvin. These temperatures were used for the respective CFD models and in the conversion model. The remaining model settings are displayed in Table 5.4.

Table 5.4: Remaining model settings

Setting	for ideal case	for setup case
Viscous	laminar	laminar
Species	on (hydrogen & air)	on (hydrogen & air)
diffusion models	off	off
Energy	on	on
Velocity inlet	0.27 & 0.675 [m/s]	1.08 & 2.7 [m/s]
Hydrogen mass fraction	0.069	0.069
inlet temperature	1023	1023
Wall temperature	1023	1023
Outlet back flow temperature	1023	1023
Outlet back flow hydrogen mass ratio	0.069	0.069
Residual target	$1e^{-6}$	$1e^{-6}$
Hybrid initialisation iterations	10	10
Courant number	100	100
Pseudo transient	off	off
Underrelaxing factors	1	1
Explicit underrelaxing factors	0.5	0.5
Solution method (spacial discretization)	2^{nd} order upwind	2^{nd} order upwind
Solution method (scheme)	coupled	coupled
Solution method (gradient)	least squares cell based	least squares cell based
Flow region	fluid & porous	fluid & porous
Permeability	$1e^{-10}$	$1e^{-10}$
Porosity	0.95	0.95
Direction vector	[1,1]	[1,1]

5.1.3 Results of the CFD

In this section the CFD results of the ideal case and the setup case with the nickel foam diffuser and the higher inlet volume flow rate will be shown. The remainder of the results are shown in Appendix A.

Firstly the ideal case results will be discussed. Figure 5.5 shows that all residuals have reduced past the residual target within 500 iterations. In the discussion of the results of the setup case, it will be shown that this residual target is sufficient for this case.

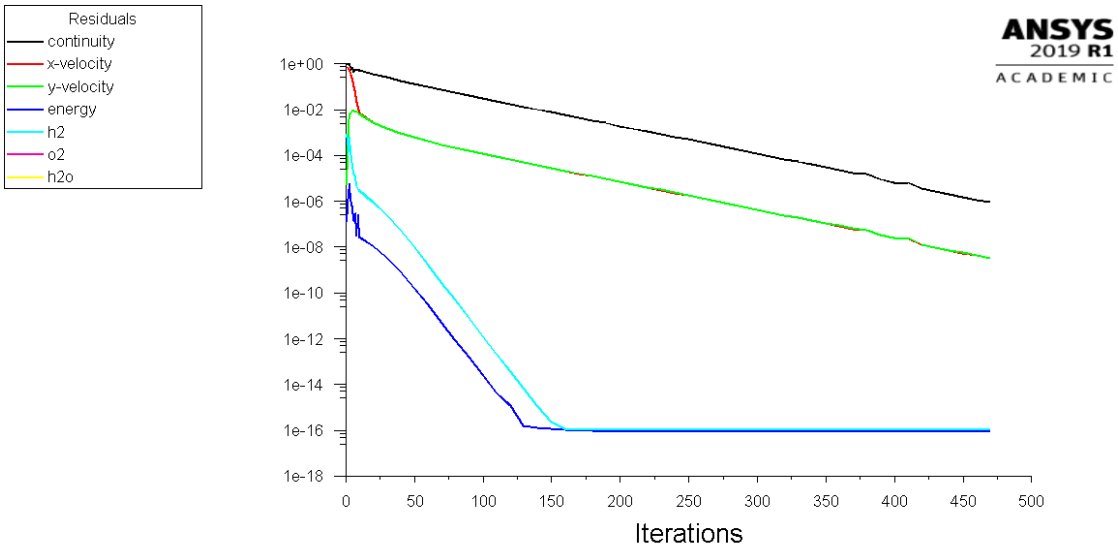

Figure 5.5: Residual plot of the CFD for the ideal case.

From the velocity profile the no slip boundary conditions at the top and bottom wall is barely visible. This boundary condition resulted in a thin blue layer on the top and bottom edges of the flow area in Figure 5.6. Compared to the case with no nickel foam diffuser the boundary layer is significantly thinner, as shown in Figure 5.7. To more quantitatively compare the scenarios of the ideal case with and without the nickel foam diffuser, the vertical velocity profile at the halfway point are shown in Figure 5.9. This figure shows the effectiveness of the porous nickel foam diffuser in reducing the boundary layer development. In Figure 5.8 the vertical velocity profile of the ideal case, with nickel foam diffuser, at the halfway point is compared to the inlet velocity profile. In this figure the boundary condition of no slip at the upper and lower wall are seen as the blue dots decrease rapidly at the top and bottom of the graph. This boundary condition causes the velocity in the middle to rise slightly, however not as significant as seen without nickel diffuser.

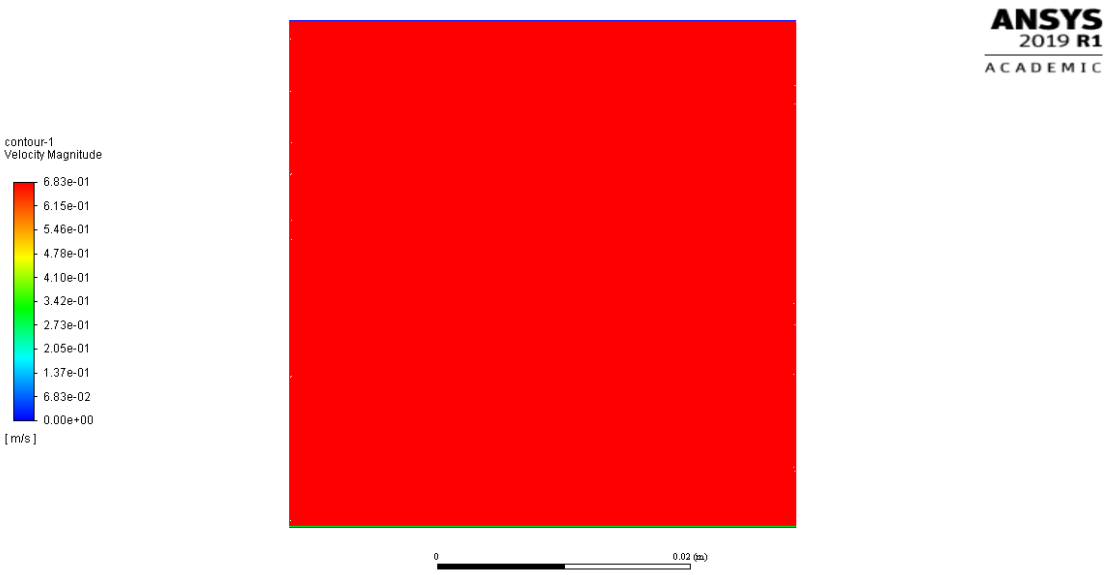

Figure 5.6: Velocity plot of the ideal case.

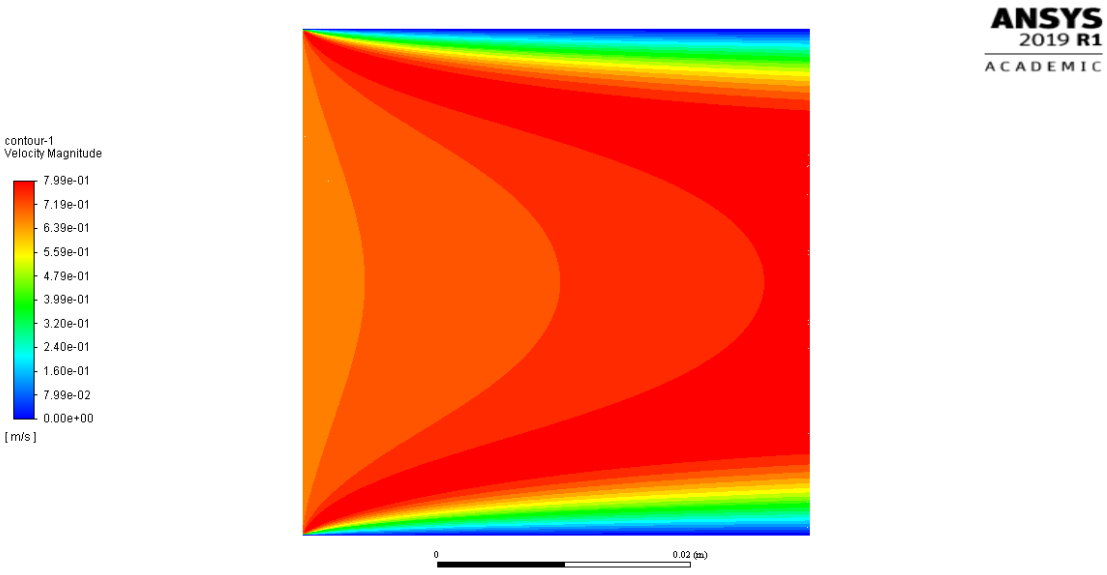

Figure 5.7: Velocity plot of the ideal case without diffuser.

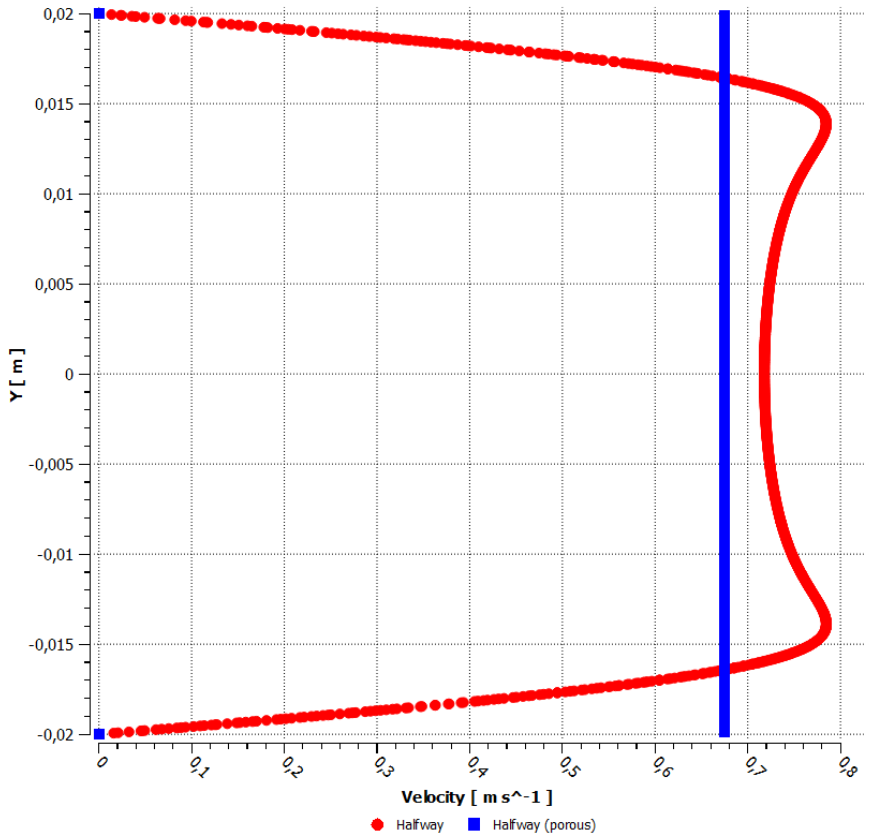

Figure 5.8: Vertical velocity profile of the ideal case with and without diffuser at the halfway mark.

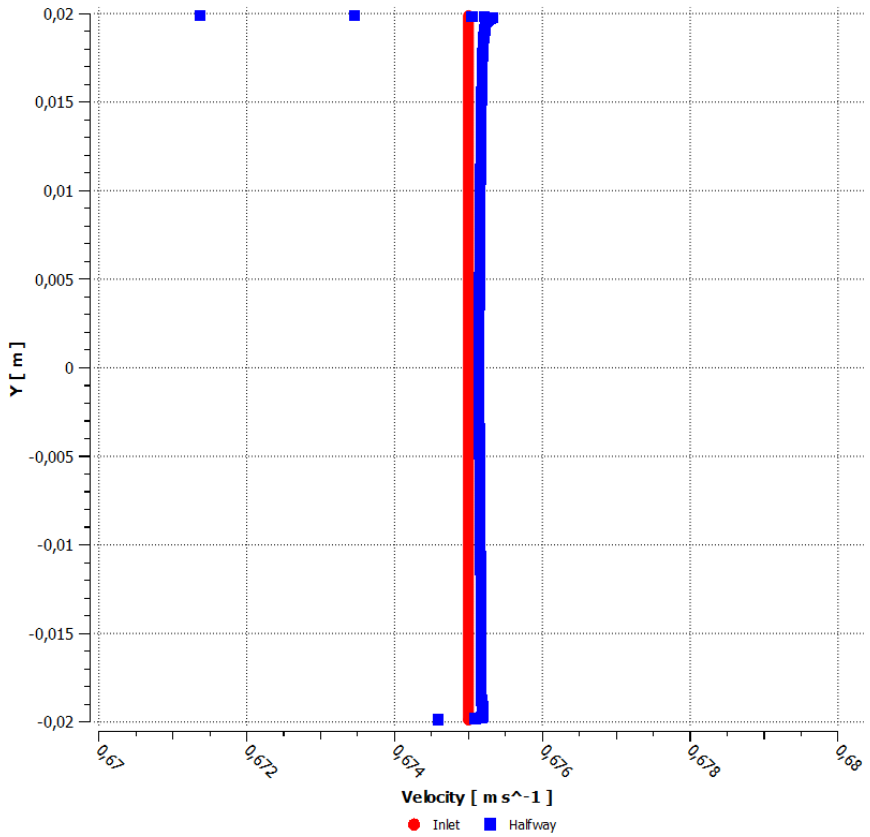

Figure 5.9: Vertical velocity plot of the ideal case with nickel diffuser at the halfway mark compared to the vertical velocity profile at the inlet.

The inlet was divided into 360 segements, as mentioned earlier. This is done so 360 streamlines can be created with different origins, to avoid streamlines sharing the same start coördinates. In Figure 5.10 the streamlines for the ideal case with nickel foam diffuser are displayed.

Figure 5.10: Streamline plot of the ideal case.

When discussing the results of the setup case a new cross section needs to be introduced. In Figure 5.11 the cross section line AA is shown. Why this line was chosen as cross section will be explained later on.

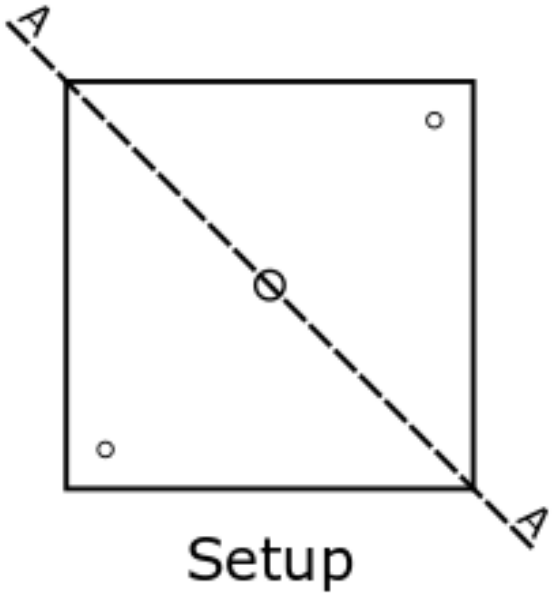

Figure 5.11: Identification of AA cross section of the setup case.

The residuals plot for the setup case with the nickel foam diffuser is shown in Figure 5.12. This figure shows that all residuals of the variables are below the target value within 300 iterations. To show that the residual target, $1e{-}6$, is sufficient the CFD analysis was left to run for an additional 1200 iterations, bring the total to 1500 iterations. After 1500 iteration the residuals had stabilised with all residuals below $2.3e^{-12}$. In Figure 5.13 the difference in the velocity profile along the AA cross section is displayed for the case with 300 and 1500 iterations. The figure indicates that the residual target chosen earlier is sufficient for this analysis.

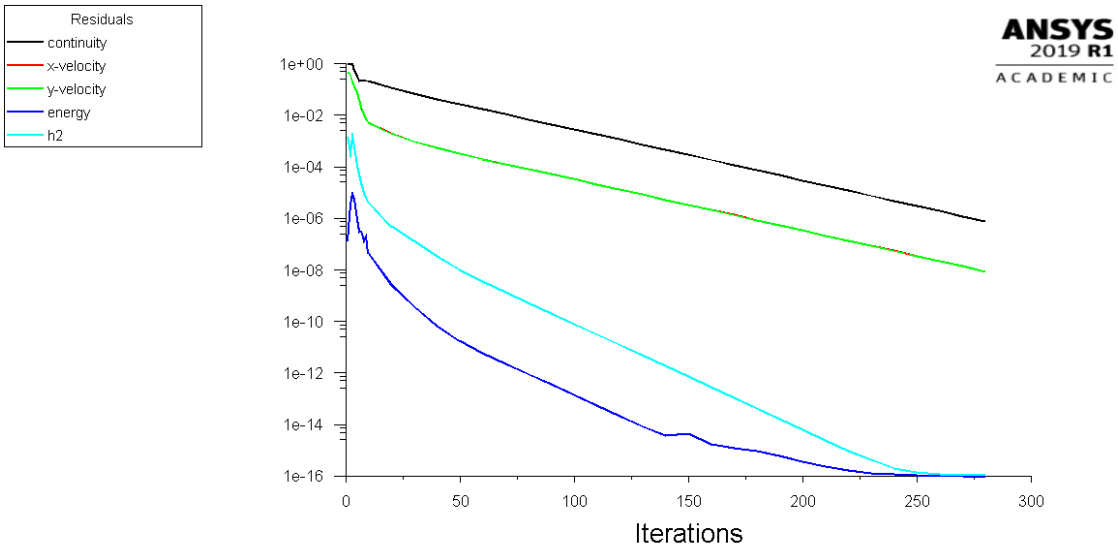

Figure 5.12: Residual plot of the CFD for the setup case.

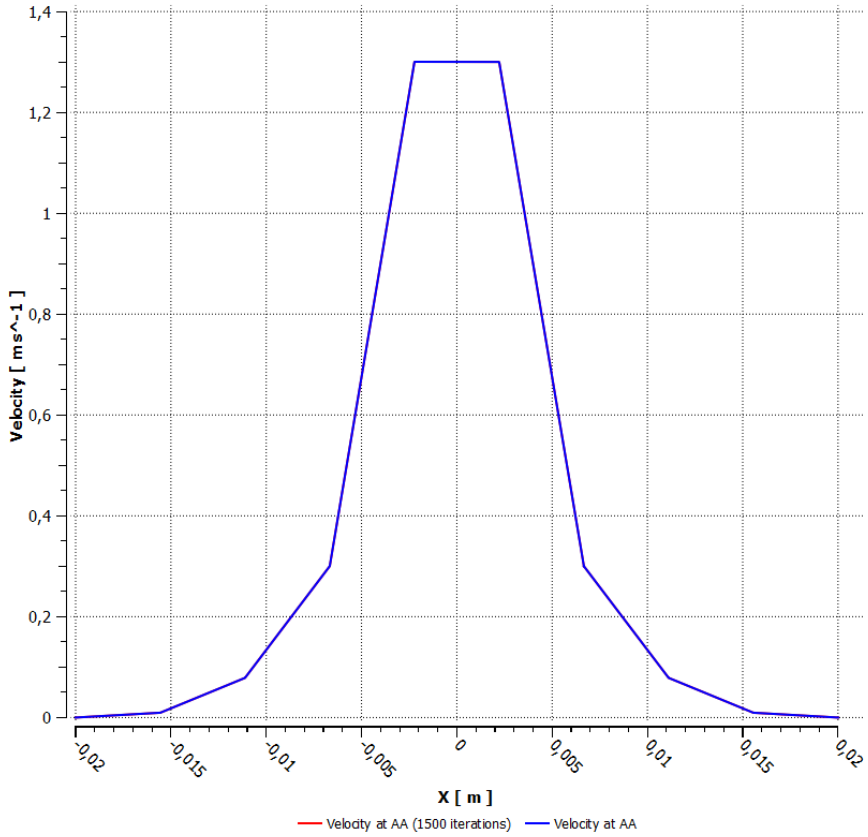

Figure 5.13: Velocity difference at the AA cross section for a simulation of 300 and 1500 iterations.

The velocity plot, shown in Figure 5.14, shows a significant difference to the more ideal case. The velocity profile shows an increased velocity on the diagonal between the outlets and the inlet and very low velocities at the ends of cross section line AA. The velocities become low enough in the top left and bottom right corner that the no slip boundary becomes invisible on the plot. To more quantitatively compare the velocity result of the setup case with nickel foam, shown in Figure 5.14, to the velocity result of the setup case without nickel foam, shown in Figure 5.15, a comparison plot is made of the velocity at the AA cross section line. This comparison is shown in Figure 5.16. In the figure the effect of the porous media is visible as the velocities in the center are lower and the velocities at the boundaries are higher. The difference between the porous case and the non porous case is not as stark as the difference seen in the ideal case. This is attributed to the fact that due to the low flow velocities in those areas, boundary layers don't develop at the same rate as seen in the ideal case.
Figure 5.16 also provides the first indication that the cell has areas where fuel starvation could be occurring and effecting cell performance, as the flow velocities are a order of magnitude lower in the upper right and lower left corners compared to the inlet. This relatively low velocity at these corners is the reason why the the AA cross section was placed on this diagonal, as it provides more information on the low velocity areas.

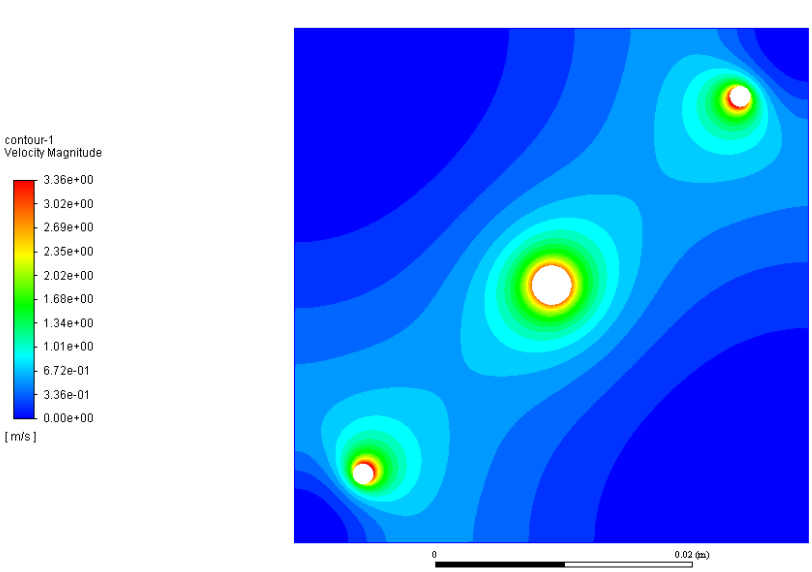

Figure 5.14: Velocity plot of the setup case.

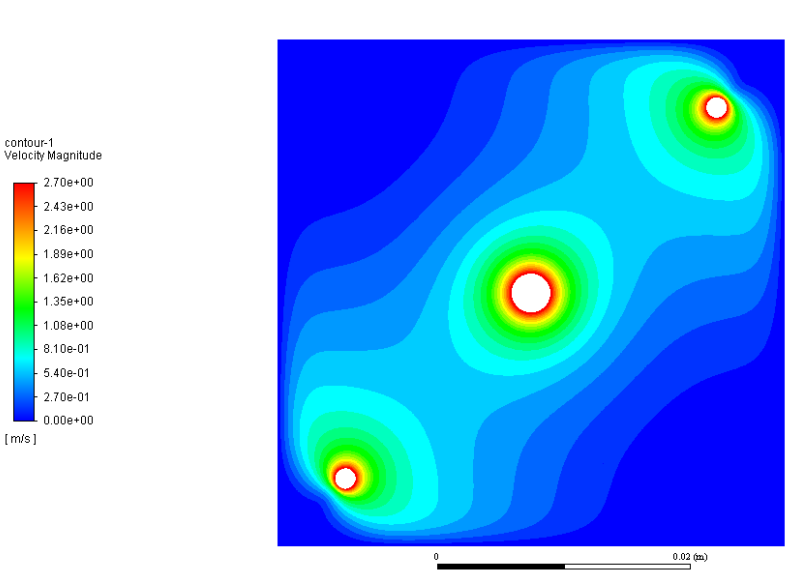

Figure 5.15: Velocity plot of the setup case without nickel foam diffuser.

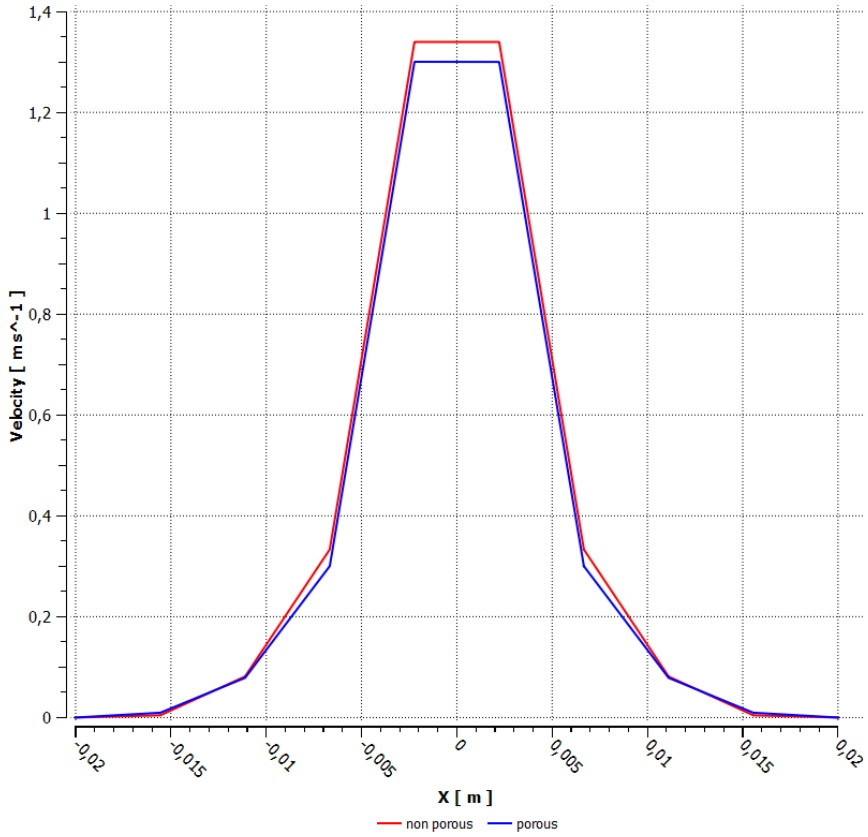

Figure 5.16: Velocity difference at the AA cross section, comparing the setup case with and without nickel foam diffuser.

In Figure 5.17 the 360 streamlines originating from the inlet are shown, and in accordance with the velocity figures, it shows a significant difference to the ideal case. The diverging streamlines in the upper left and lower right corners are in accordance with the low velocity in these corners seen in Figure 5.16. As mass can not cross a streamline and the streamlines diverge, the flow velocity between streamlines has to decrease.

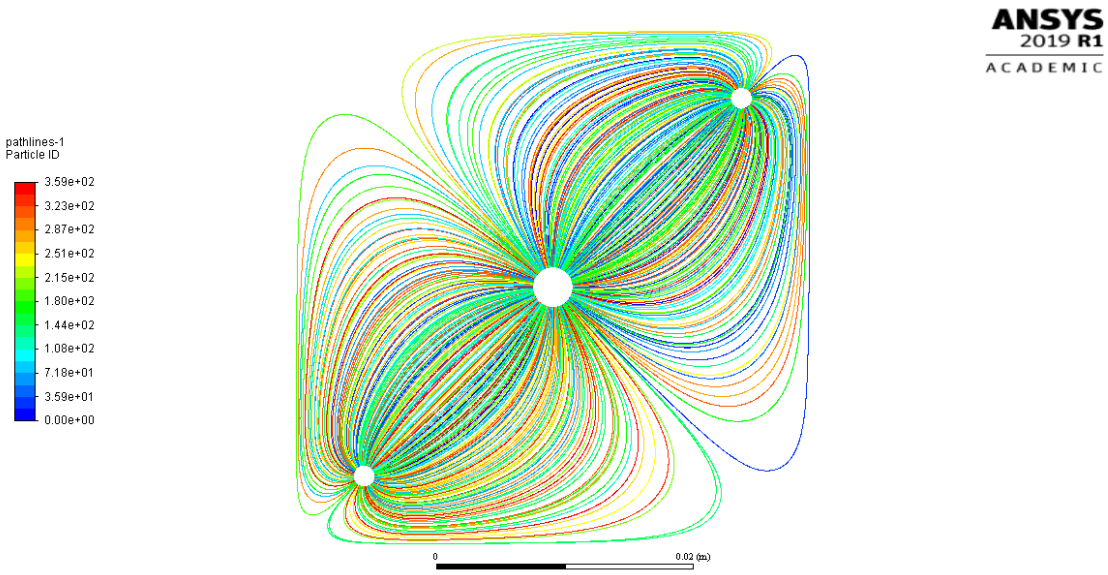

Figure 5.17: Streamline plot of the setup case.

5.2 The conversion model

In this section the conversion model is described. The conversion model utilises the streamlines produced by the CFD analysis described in the previous section. Between these streamlines segments are made, these segments will act as mesh elements. The choice to remake a mesh using the streamlines is based on the assumption that diffusion is neglected, see Section 5.1, and that no mass crosses streamlines [65]. This makes calculations easier as the mass from one segment can only go to the next segment between the same streamlines. Each segment is then solved with a 0D SOFC model.
By basing the conversion model on the streamlines from the CFD analysis it is assumed that the streamlines do not significantly change due to phenomenons associated with SOFC operation, as the CFD analysis does not include mass transfer or electrochemical reactions due to SOFC operation. The streamline plot in 5.17 shows a very similar pattern as seen on the fuel electrode in Figure 5.1. The fact that the markings are the result of oxidation of the nickel fuel electrode, means that the markings shown in Figure 5.1 are made when the cell was in operation. The visual comparison between the CFD results and the markings on the fuel electrode is the only comparison method available during this research. This means that the assumption, that the streamlines do not change significantly due to mass transport effects due to SOFC operation, can not be rejected on the basis of these CFD results and comparison method.

The conversion model is made using the program Matlab. The choice to make a Matlab script based model rather than a Matlab simulink or Aspen model is based on the fact that less programming skill is required, as a Matlab script contains a list of equations which are calculated

in order from top to bottom. This, when sufficient comments are added, makes the model easier to debug and modify. Matlab also offers tools to import data from Ansys Fluent in contrast to Aspen.

5.2.1 Producing segments

Each of the streamlines from the CFD analysis are stored as a number of x and y coördinates and a streamline number in Ansys. These values can be exported as csv file. This file can be converted in matlab to a matrix with the "csvread" command. This command converts the csv file into a three column matrix where the first two columns contain the x and y coördinates and the third column contains the streamline number. In this section it is described how this streamline data is converted into the segments.

The streamlines for the ideal case are numbered from bottom to top in ascending order. In the setup case the streamlines originate from a circle, which caused Ansys to number the streamline seemingly random. This seemingly random numbering of streamlines means that streamline 1 and 2 are not necessarily neighbouring streamlines. Therefore, the streamlines from the setup case need to be renumbered to be able to make segments between the streamlines later on. The sorting is done by calculating the angle of each initial point of the streamlines to the negative x-axis. To sort the streamlines the streamline with the lowest angle was given streamline number one, with ascending numbering in a clockwise direction.
With the streamlines numbered in a predictable order, segments between streamlines can be made. These segments will be used for the SOFC model later in this chapter. Due to the different nature of the streamlines from the setup case compared to the ideal case, a slightly different approach is needed for this case.

To make a segment between streamlines consists of 4 coördinates. Two of these coördinates need to be on the streamline at the top of the segment, two need to be on the streamline at the bottom of the segment. The top coördinates of the segment can be the same as the coördinates from the top streamline. However, as not all streamlines have the same number of points, making all segments with the bottom points with the coördinates of the corresponding streamline therefore won't work. To solve this problem two points are created on the lower streamline below the top points of the segment. These points are created by using what will be referred to as "dummy lines". These lines are used by the program to produce the bottom coördinates of the segments but are otherwise meaningless. These dummy lines are drawn vertically down from the third to the second to last coördinate of the top streamline. The vertical dummy line intersects with the streamline below, these intersection points are used as the bottom coördinates of the segment. This is shown in Figure 5.18. In this figure the black lines are the streamlines from the CFD where the stars indicate the coördinates that are imported with the "csvread" command. The blue lines originating from those black stars are the dummy lines, dotted for the first streamline and dashed for the second streamline. The intersection points on the streamlines are marked with red stars.

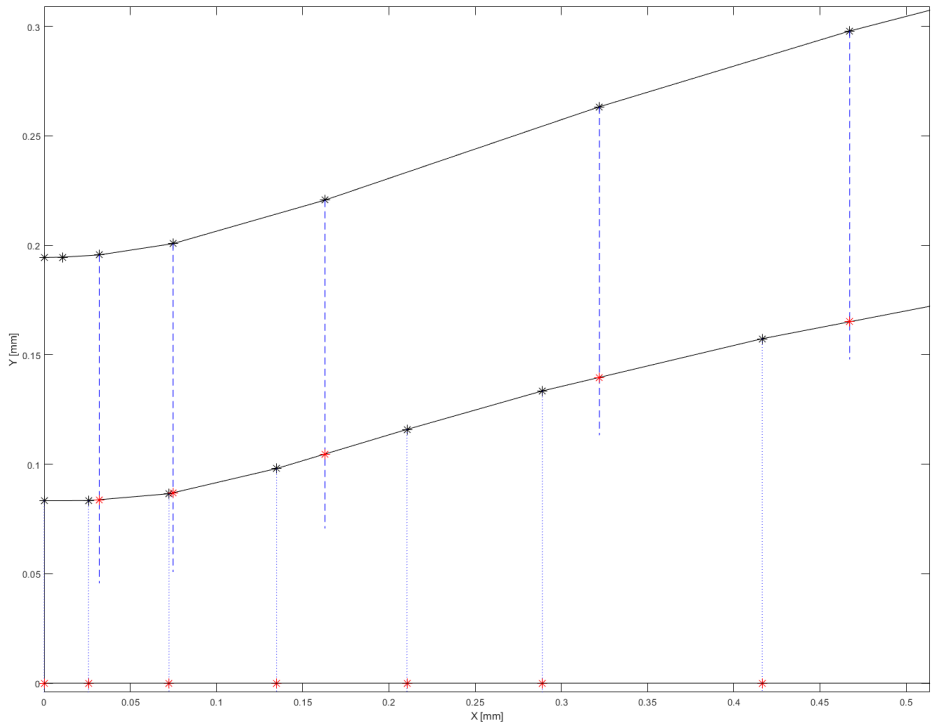

Figure 5.18: A figure displaying coördinates and intersection points made by the conversion model.

For the first segment between two streamlines, the first two coördinates of the upper streamline and first two coördinates of the streamline below are used. For the second segment the second and third coördinates of the top streamline are used in combination with the second coördinate of the bottom streamline and the first inter section point. All following segments, except the last segment, between these streamlines only utilise the coördinates of the top streamline and the intersection points on the bottom streamline. In the case of the last segment the last coördinates of both streamlines are used in combination with the second to last coördinate of the upper streamline and the last intersection point created by the dummy lines on the streamline below.
As the first streamline does not have a streamline below it the dummy lines can not intersect with a streamline. Therefore the wall below the first streamline is assumed to be a streamline. This assumption can be done as no mass flows through the wall of the setup. With the wall representing an effective 0th streamline segments between the first streamline and the bottom wall can be made. When producing the segments between the upper most streamline and the top wall, the same principle applies. In that case however, the lines are drawn vertically up from the last streamline, rather than down from the top wall. This is done as the lines representing the walls only contain two coördinates each, one at each end.
The resulting segments of this method is displayed in Figure 5.19 for the first two streamlines.

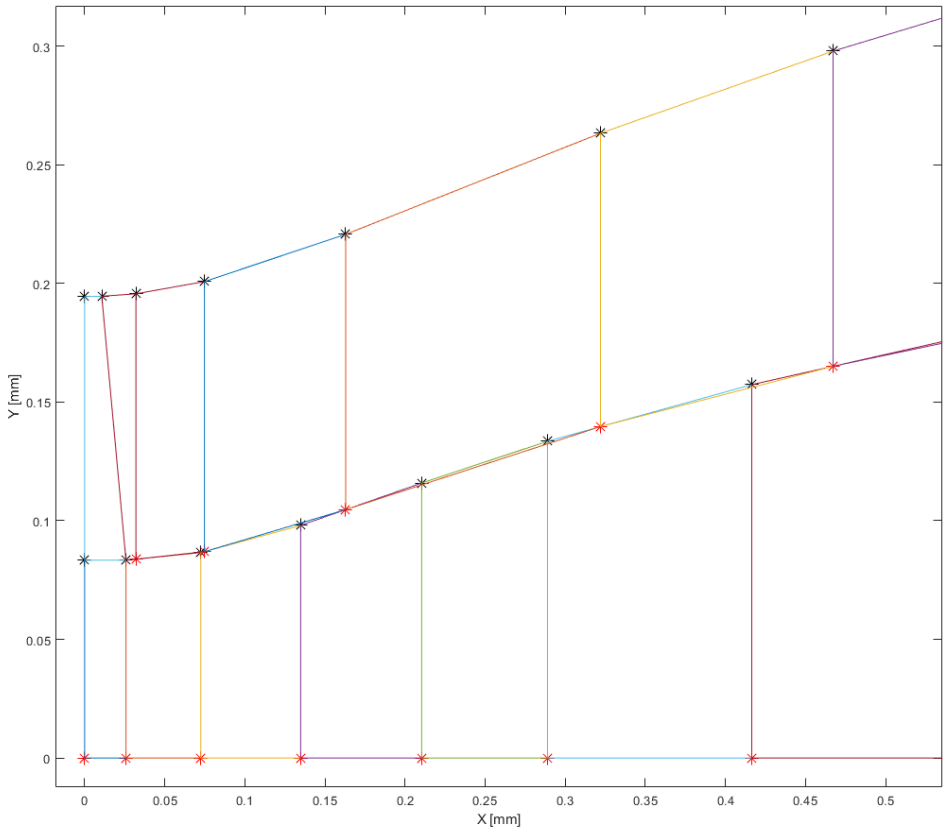

Figure 5.19: A figure displaying the segments in the ideal case.

In the setup case the same principle is used as described above, creating dummy lines originating from a particular streamline coördinates which intersect another streamline. Because the streamlines in this case change directions significantly, a simple line vertical dummy line down does not work, as intersection can not be guaranteed with this method. As such the dummy lines originating from the streamline coördinates are drawn perpendicular to the streamline. This practice is shown in Figure 5.20.

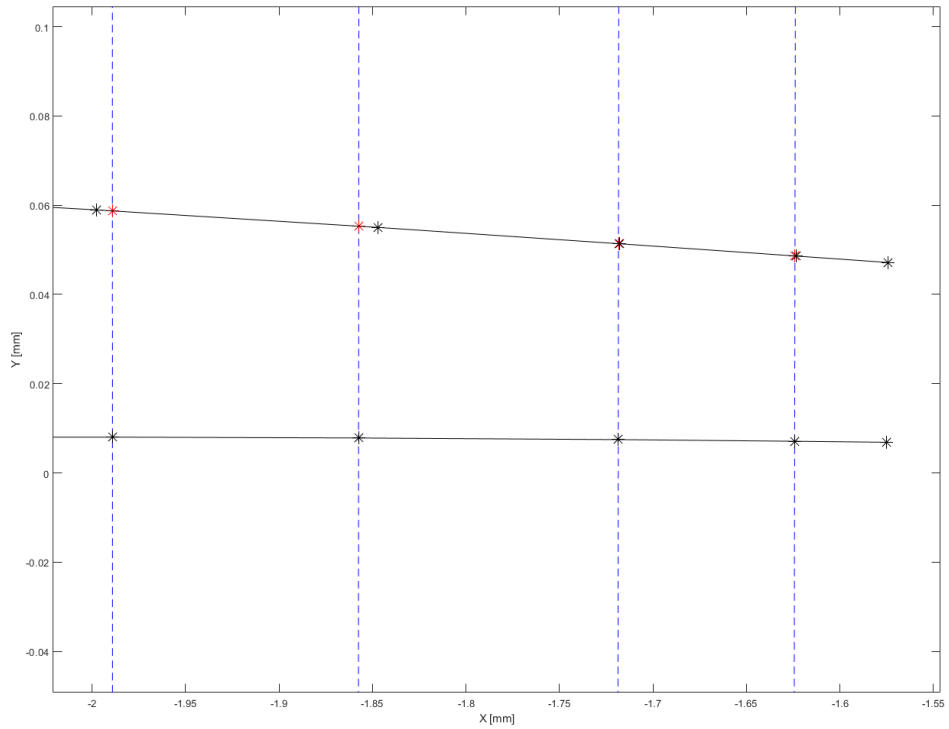

Figure 5.20: A figure displaying the streamlines, the dummy lines and intersection points in the setup case

As becomes apparent in the figure above the intersection points are on the upper streamline rather than on the bottom. This is an effect of the upper streamline being longer than the bottom streamline. When the dummy lines originate from the shorter of the two streamlines, it ensures that the dummy lines intersect with the neighbouring streamline. The program therefore checks the number of coördinates associated with both streamlines. From the streamline with the fewest coördinates the dummy lines are drawn towards the longer streamline. This results in the segments seen in Figure 5.21

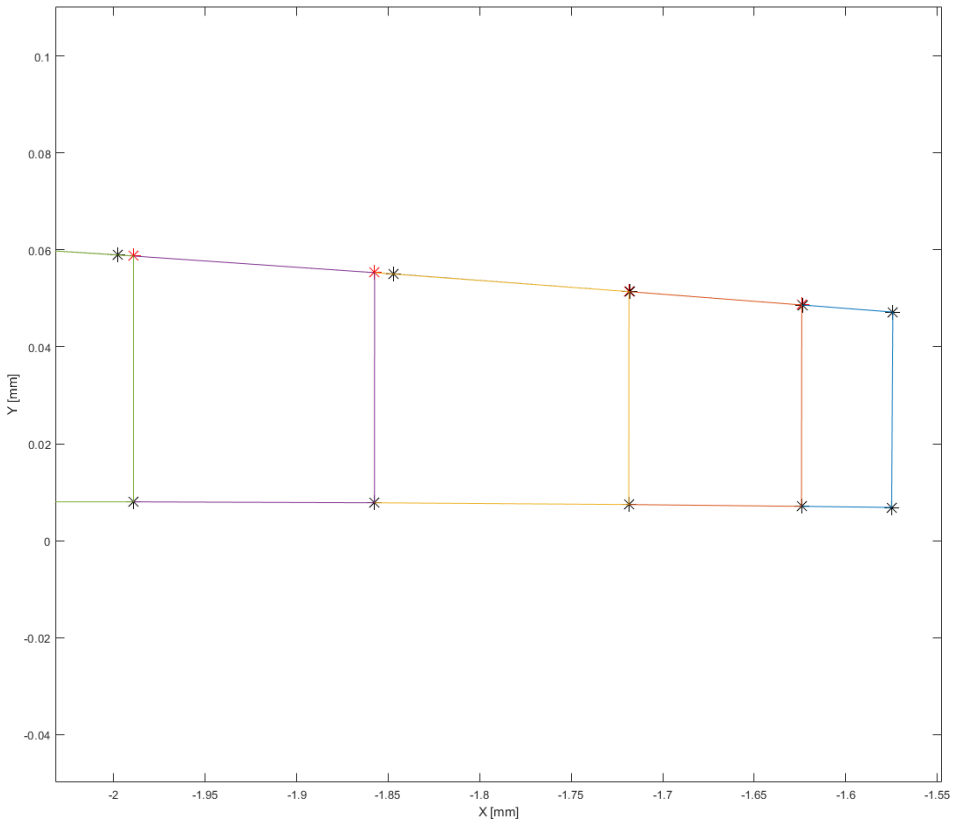

Figure 5.21: A figure displaying the segments in the setup case.

The limitation of this method of making segments becomes clear as it does not function between four streamlines. As the outer streamlines, depicted in Figure 5.22 as solid lines, diverge, any dummy line originating from either of the streamlines do not always intersect the neighbouring streamline in a useful way. To solve this problem imaginary streamlines are introduced. These imaginary streamlines are depicted in Figure 5.22 as dashed lines. Part of the imaginary streamlines are the walls of the setup. As there is no mass flow through the wall of the setup this is a relatively safe assumption. The diagonal imaginary streamlines can have mass crossing them, which is neglected if they are assumed to be streamlines. As the diagonal lines are also mirror lines, the mass flow across the lines should be relatively minimal and thus negligible.

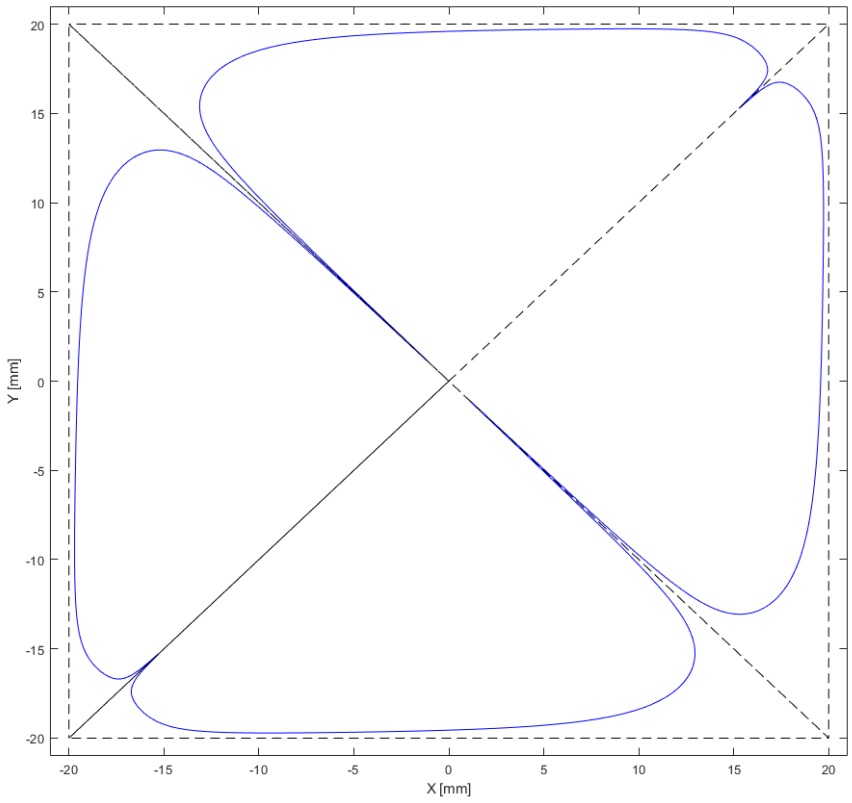

Figure 5.22: A figure displaying the outer most streamlines and the imaginary additional streamlines.

5.2.2 SOFC model

With the area between the streamlines divided into segments with the methods described in the previous section, the matlab conversion model needs a 0D SOFC submodel to convert the data from each segment into current densities, fuel utilisation and potentials. In this section the SOFC submodel is described. The section is split into two sections, the electrochemical model and the equipotential control mechanism. In the electrochemical model section the equations used to simulate the solid oxide fuel cell process are described. In the equipotential control section the method used to ensure all segments are operated at the same potential is explained. The choice for for an equipotential model is based on the fact that the electrodes are good conductors which implies that they are equipotential surfaces [66].

5.2.2.1 Equipotential control method

As the current density and the potential of a fuel cell or electrolysis system are dependent on each other, one is often prescribed as a uniform user specified value in a model. When the potential is chosen by the user and assumed uniform across the cell, the model is said to be equipotential. As mentioned, the model in this report is under equipotential conditions, meaning the operational potential in each segment is equal, with the current density varying in each segment. However, it is quicker to compute the potential with a given current density. The model therefore aims to combine the equipotential constraint and the ease of calculation if the current density is given. In the section below it is explained how this is achieved by the model.

It is possible to take all the relevant Nernst and overpotential equations from the Chapter 2 and use a "system of equations" solver to calculate the current density for a given potential. However this takes a relatively long time, approximately 0.5 seconds per segment. This doesn't seem a much initially, but over 500 segments this adds up to about 3.5 minutes. With approximately 55000 segments in the model, a faster way of solving the system of equations needed to be found. This new method was found by asking the question: how precise does the equipotential condition need to be? If the equipotential condition is allowed to fluctuate 0.01% between segments, an alternative way of doing the calculation becomes available as explained below.

Rather than using a system of equation solver, an iterative loop is placed around the relevant equations. In this loop the (over)potentials are calculated for a segment, with a given current density. In the first iteration of the loop, the calculations are done with a very high current density value, 50000 A/m^2. This causes the potential resulting from the calculations to be relatively low, compared to normal operating voltages. For each of the following iteration this current density is decreased by 1 A/m^2, causing the calculated potential to rise slightly with every iteration. When the potential is lower than the user specified value the loop continues, if the potential is equal to or higher than the user specified potential value, the iterations are stopped. This decision tree is shown in Figure 5.23 and is also known as a while loop.
Doing the calculations with this method, the script can calculate the current density for 500 segments within 10 seconds. The cost of this decreased computational time is that the potentials of each segment can fluctuate by a maximum of 0.01%. Further computational time decreases can be made if the current density step is increased or if the initial current density value is dynamically adjusted per segment. For this research however the computation time of 10 seconds per 500 segments is deemed acceptable.

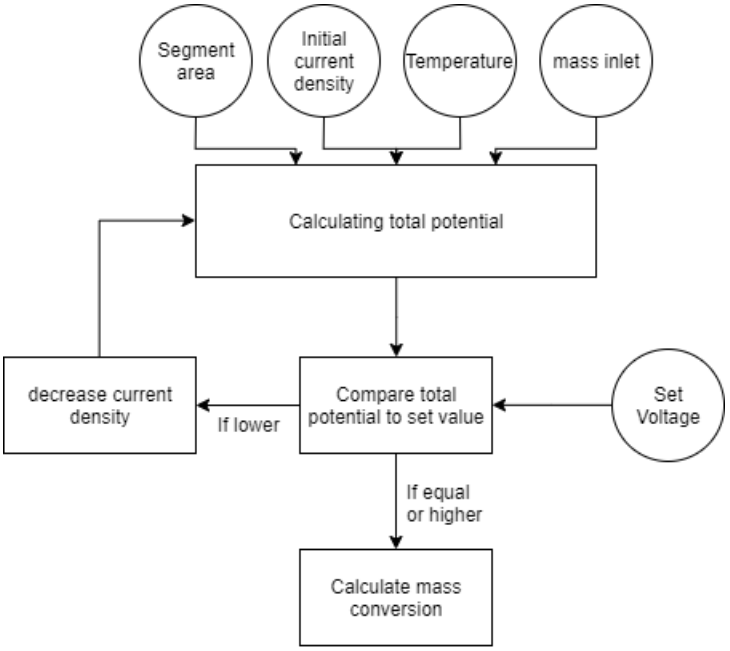

Figure 5.23: The decision tree used in the Matlab program to achieve an equipotential result.

5.2.2.2 Electrochemical model

In the previous section the equipotential control method is described. In this section the equations used to calculate the potential for a given current density are explained in more detail.
Before the potentials can be calculated, the method of determining the mass, or concentration, for each species in each segment needs to be clear. The first segments receive mass from the inlet. It is assumed that the inlet mass flow is distributed equally over the initial segments. This means that each segment receives 0.27777% of the inlet mass flow. In the model the mass conversion in a segment is calculated with Equation 5.5, where the area of a segment is determined with the matlab function "polyarea" and the coördinates of the segment. The masses resulting from this equation are the mass outputs of a segment. This output is used as the mass input for the next segment.

The result of the electrochemical model needs to be total, or operating, potential for a given segment. This is calculated by the model by subtracting the overpotentials from the Nernst potential, as shown in Equation 5.6.

$$V_{total} = V_{nernst} - V_{ohm} - V_{act_{fuel}} - V_{act_{air}} - V_{conc_{fuel}} - V_{conc_{air}} \tag{5.6}$$

The Nernst potential is calculated with Equation 2.7. In this equation the operating temperature and the partial pressures of hydrogen, oxygen and water need to be specified. The temperature

is determined by user input and due to the assumption that the cell operates under uniform temperature, this is the same for every segment. As the cell is assumed to operate under uniform atmospheric the partial pressures are calculated by the mass ratio of the species inside the segment.

The ohmic losses are calculated with Equations 2.9, 2.10 and 2.11. This overpotential is dependent on temperature, material properties and current density. The material properties used for these equations are specified in Table 5.5. As the specific data for the cells that were used is unknown, values from literature are used [18][19].

Table 5.5: Material properties for ohmic losses

Property	Value [unit]
τ_{air}	26e-6 [m]
τ_{elec}	370e-6 [m]
τ_{fuel}	6e-6 [m]
σ_{air}	40e3 [1/Ω]
σ_{elec}	(3.6e7/T)*exp(-(80e3)/(R*T))[1/Ω]
σ_{fuel}	80[1/Ω]

For the concentration overpotentials, the concentrations of each species inside the segment have to be calculated. The concentrations are calculated by dividing the number of moles by the volume of the segment. The number of moles is determined by dividing the total mass of a species in the segment by the molar mass. The molar masses for the relevant species are given in Table 5.6. The volume is determined by multiplying the height of the flow channel, 0.5 millimeter, by the area of the segment. It is assumed that the concentration is uniform in volume of the segment and that the effective diffusion coëfficient for the fuel electrode has a constant value of $36.6e-6(m^{-2}s^{-1})$ [18]. The effects of this assumption on the model results will be discussed in Chapter 7. It is also assumed that the concentration overpotential at the air electrode is sufficiently small to be neglected. With these variables determined the concentration overpotentials can be calculated with Equations 2.12,2.13 and 2.14.

Table 5.6: Molar mass values.

Species	Molar mass [unit]
M_{h2}	0.0002 [kg/mol]
M_{h2o}	0.0180 [kg/mol]
M_{o2}	0.0320 [kg/mol]
M_{n2}	0.0280 [kg/mol]

The last overpotential that needs to be calculated to determine the operational voltage is the

activation overpotential. This is calculated using Equations 2.15, 2.16 and 2.17. The activation energies and the preëxponential factors used for these equations are given in Table 5.7.

Table 5.7: Values for variables for the activation overpotential equations.

variable	Value [unit]
K_{air}	485e9 $[1/\Omega m^2]$
K_{fuel}	254e9$[1/\Omega m^2]$
E_{air}	131.25e3 [J/mol]
E_{fuel}	133e3 [J/mol]

5.2.2.3 From model to function

The SOFC model, described in the two sections above, is integrated into the the program that creates the segments as a function, shown in Equation 5.7. The function requires the mass inlet flows, temperature, area and desired operational potential of a segment as inputs to calculate the current density for that particular segment. The function outputs the values for the mass output, each overpotential and the current density for the particular segment.
This function is used in the program after the coördinates of a segment are determined. This order of computation is necessary as the area of the segment is needed as an input for the function. The order of calculation processes is displayed in Figure 5.24 and is repeated between every streamline.

$$Outputs(MassOut, Overpotentials, CurrentDensity) = function(Voltage, Temperature, Area, MassIn) \tag{5.7}$$

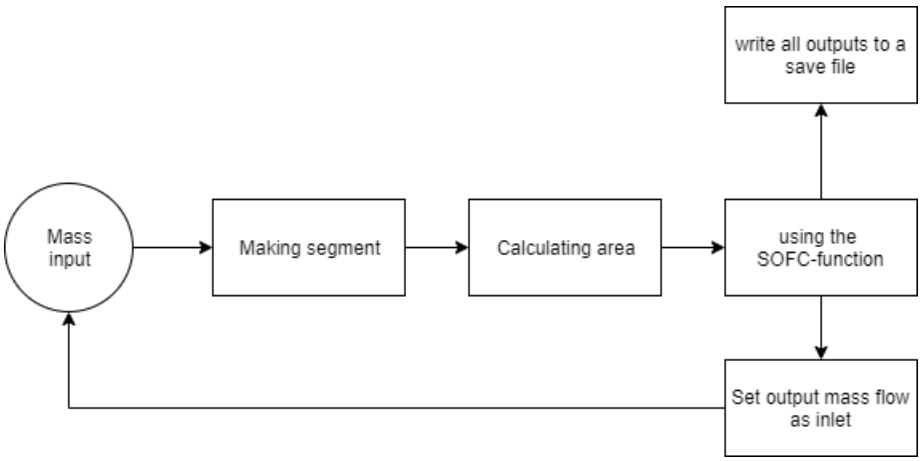

Figure 5.24: The program loop with incorporated SOFC-function command.

5.2.2.4 Producing graphical results

There were two methods considered to produce the figures seen in this chapter. The first method considered was to plot each segment as it was made. This method would add approximately 0.5 seconds per iteration, which would add 15 hours to the total computational time. For this reason the other method was chosen. In this method the coördinates of the nodes of the mesh elements from the CFD analysis are loaded into the model. When the function has calculated the outputs for a segment, these outputs are assigned to the points in that segment area. When the computation is done the plot can be made using the mesh coördinates and one of the output parameters. This method has less impact on computational time as the plot function is only used once.
The cost of this increase in computational time is the visual graphical resolution. As some coördinates are missed by the program they show up as points with value zero in the figures. This becomes vary apparent in Figure 7.10 between y-values of 30 and 35. Furthermore, compressing the nearly 1 million coloured data points to a relative small area produces some graphical anomalies. To put the number of data points into perspective, a 720P HD TV has less pixels than the graphs have data points. It is important to note that these anomalies are not found in the actual segment data produced by the model and thus not effect the calculations or the results of the model.

5.3 Model results in brief

The results of the model are displayed and explained in Chapter 7. In this section the results are explained very briefly to indicate why a new flow distribution plate is proposed in the next chapter. The model results show a significant increase in current output at the same potential for the ideal case compared to the setup case. This increase in current output at the same potential can be translated to a higher potential at the same current output and thus indicates better cell performance. Furthermore the setup case results show large areas with more than 80% fuel utilisation, which is when fuel starvation effects can occur [67]. In contrast the ideal case fuel utilisation remained below 60%, therefore reducing the risk on fuel starvation effects significantly.
Because of the results mentioned above it is shown by the model that switching from the setup flow distribution to a more ideal flow distribution can improve cell performance due to lower maximum fuel utilisation. This means that a test station will perform cell performance and degradation measurements better and more reliable as the cell performance and long term stability will be significantly less (negatively) effected by the flow distribution from the test station. Because of this, a new design of the flow distribution plate is proposed in to achieve a flow distribution closer to the ideal flow seen in this chapter.

Chapter 6

Flow distribution plate optimisation

With the results from the model described in the previous chapter, it becomes clear that there are benefits to implement a more ideal flow in the test station, as this minimises the (negative) influence of the test station on the measured results. In this chapter a new flow distribution plate design is evaluated. The goal of the new flow distribution plate is to create the inlet condition associated with the flow distribution from the ideal case in Chapter 5.

6.1 New Design

To be able to fit the design into the existing test station some design constraints have been put into place. One of these constraints is that the inlet and outlet ducts need to extrude perpendicular to the cell surface area from the flow distribution plate. As described in Section 3.1, the cell is sandwiched between two flow distribution plates and is suspended in the middle of the oven by attaching the inlet and outlet ducts coming from the flow distribution plates to the oven. This design constraint means there is a need for a method of converting the perpendicular flow to a tangential flow. In this design the inlet and outlet of the flow distribution plate are therefore moved to the sides, to create space to redirect the mass flow from the inlet duct and to create a desirable flow distribution.

To supply the cell with tangential mass flow, the mass flow direction needs to be turned 90 degrees as the inlet duct supplies the mass flow perpendicular to the cell due to the design constraint. To do this a channel needs to be cut into the flow plate. Unfortunately, as commercial metal 3D printing techniques are not available at the time of writing, the channel needs to be milled into the plate, which leaves the flow distribution plate open. The channel is therefore covered up with a cover plate made from the same material, which seals off the flow channel. In Figure 6.1 a section half view of the distribution plate is shown in the xz-plane, where the main flow plate is indicated with pink, the cell is indicated with orange, the mica seal with green and the cover plate in blue. From the figure it becomes clear that without the cover plate, indicated with blue, sealing the cell would be a challenge.

From this picture as well it is seen that the area underneath the cell is not milled. The reason for this is that the cell need to be insulated with a mica seal to prevent gas leakages. This mica seal, placed between the cell and the flow distribution plate, creates a distance between the cell and the flow distribution plate. If the flow distribution plate below the cell was milled like the rest of the channel, the bulk concentrations below the electrode would decrease due to the increased channel height, as concentration is a function of volume and number of molecules. This drop in concentration will influence cell performance, as concentrations effect the Nernst potential and overpotentials, as displayed in Equations 2.7 to 2.17. It is possible to negate these effects by introducing flow obstacles, however it is more convenient in the production process to not mill out the flow distribution plate section underneath the cell.
The resulting bump in the flow area does cause a z-shaped bend in the duct to exist and the entrance effects do need to be taken into account in determining the flow velocity profile along the cell. A more detailed evaluation of the z-shaped duct is given below.

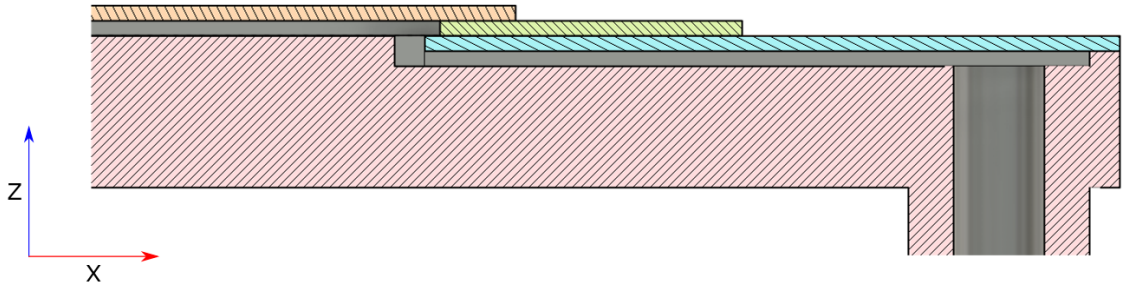

Figure 6.1: A half view of a design to seal of the channel necessary to turn the incoming mass flow by 90 degrees.

With the z-shaped duct design the flow passes through two 90 degree bends, which means that the velocity profile needs a distance to stabilise after these bends. This phenomenon is known as an entrance effect. To determine the entrance effect and length in this design, a 2D CFD simulation was done. This simulation used the same settings as described in Chapter 5, with the exception that the element size was reduced to $3.5e^{-5}$ and set to quadrilateral, the flow media was set to porous to minimise entrance effect and the inlet velocity was chosen as 0.27 m/s. The result of this simulation is shown in Figure 6.2. From this figure it becomes clear that the entrance effect lasts less than 0.5 millimeter.
To avoid that the entrance effects influence the cell performance, the cell is placed such that the active electrode area starts after the entrance effects. This means that the raised section underneath the cell is made 42 millimeter long, 2 millimeter more than the active cell area. This extra two millimeter, one millimeter at each end, prevents the leading and trailing edges of the cell to be effected by the entrance effects.

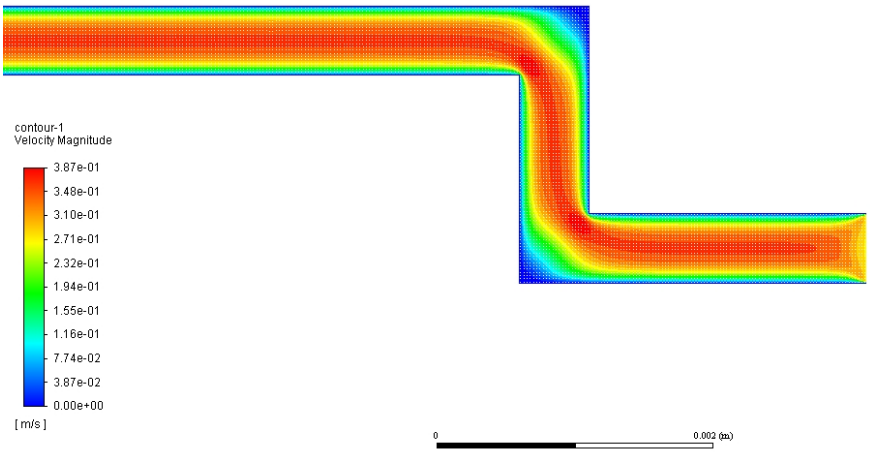

Figure 6.2: 2D velocity profile in the z-shaped duct transporting the fuel gasses to the cell.

The CFD analysis of the z-shaped duct gives an indication of the flow distribution profile in the xz-plane, as indicated in Figure 6.1. As the flow volume below the cell is three dimensional, the flow distribution in the xy-plane needs to be investigated as well. It is in this plane where the flow distribution study is done in Chapter 5. It is therefore important that the design creates the flow distribution seen at the inlet of the ideal case in Chapter 5, to achieve the goal set out for the design. To achieve this flow distribution, four different expansion area's are investigated. These flow areas are displayed as drawings in Figure 6.3. These drawings indicate the shape of the flow channel, shown in Figure 6.1, in the xy-plane.
In these designs the 3 millimeter diameter circles serve as mass flow inlets. The 3 millimeter diameter inlets have been chosen on the fact that it's a common size drill bit used in milling machines, which makes production easier, and the original setup operates with a similar inlet diameter, namely 3.17 millimeter, meaning the results will be comparable. The 40 millimeter edge on the left serves as mass flow outlet, which is located at the beginning of the z-shaped duct. The horizontal length of 22 millimeter is limited by the maximum flow plate dimensions the test station can accommodate, which is 90 millimeters.

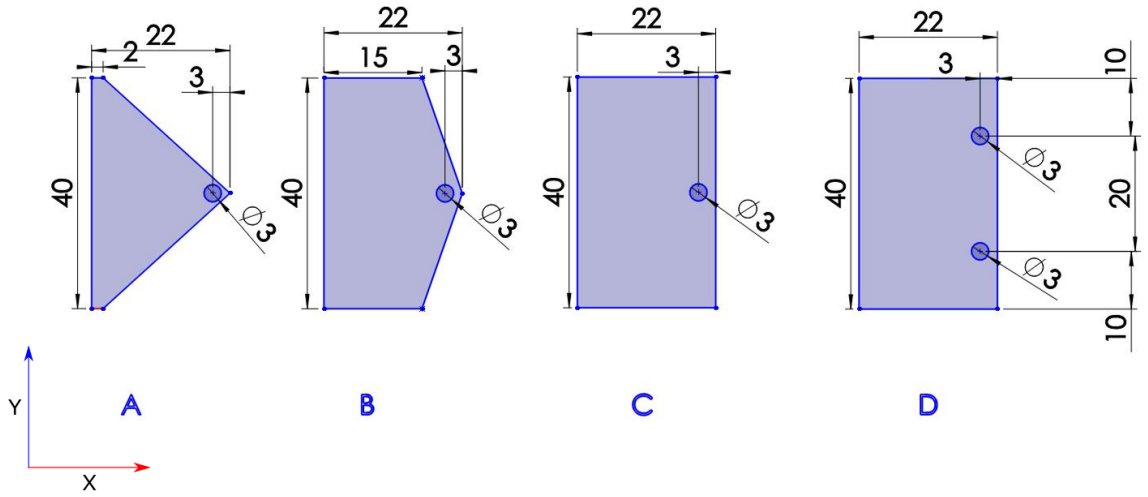

Figure 6.3: Designs of expander flow areas.

In Chapter 5 it is demonstrated that introducing nickel foam in the flow area minimises boundary layer development and provides a more uniform flow. This is the reason that the flow areas are modelled with as a porous media, to reduce the boundary layer development. Therefore, to achieve the CFD results in the experimental setup, the flow channel has to be filled with a nickel foam. The addition of nickel foam in the expansion area also creates continuity as the entire flow volume will be filled with nickel foam.

To evaluate the flow areas, 2D CFD simulations are made of each drawing. For these simulation the same settings as described in Chapter 5 where used, except the element size was reduced to $3.5e^{-5}$ and the inlet velocity was set to 1.15 m/s, to match the volume flow velocities mentioned in Section 3.1. The results of these CFD simulations is shown in Figure 6.4. The figure shows the outlet velocity profile for all designs. From this graph it becomes clear that the dual inlet design (D in Figure 6.3) provides a outlet velocity profile that most closely matches the inlet velocity profile seen in Chapter 5. In order to quantify how much this design matches the goal of creating the ideal inlet flow conditions, the inlet flow distribution and the outlet of the design are compared in Figure 6.5.

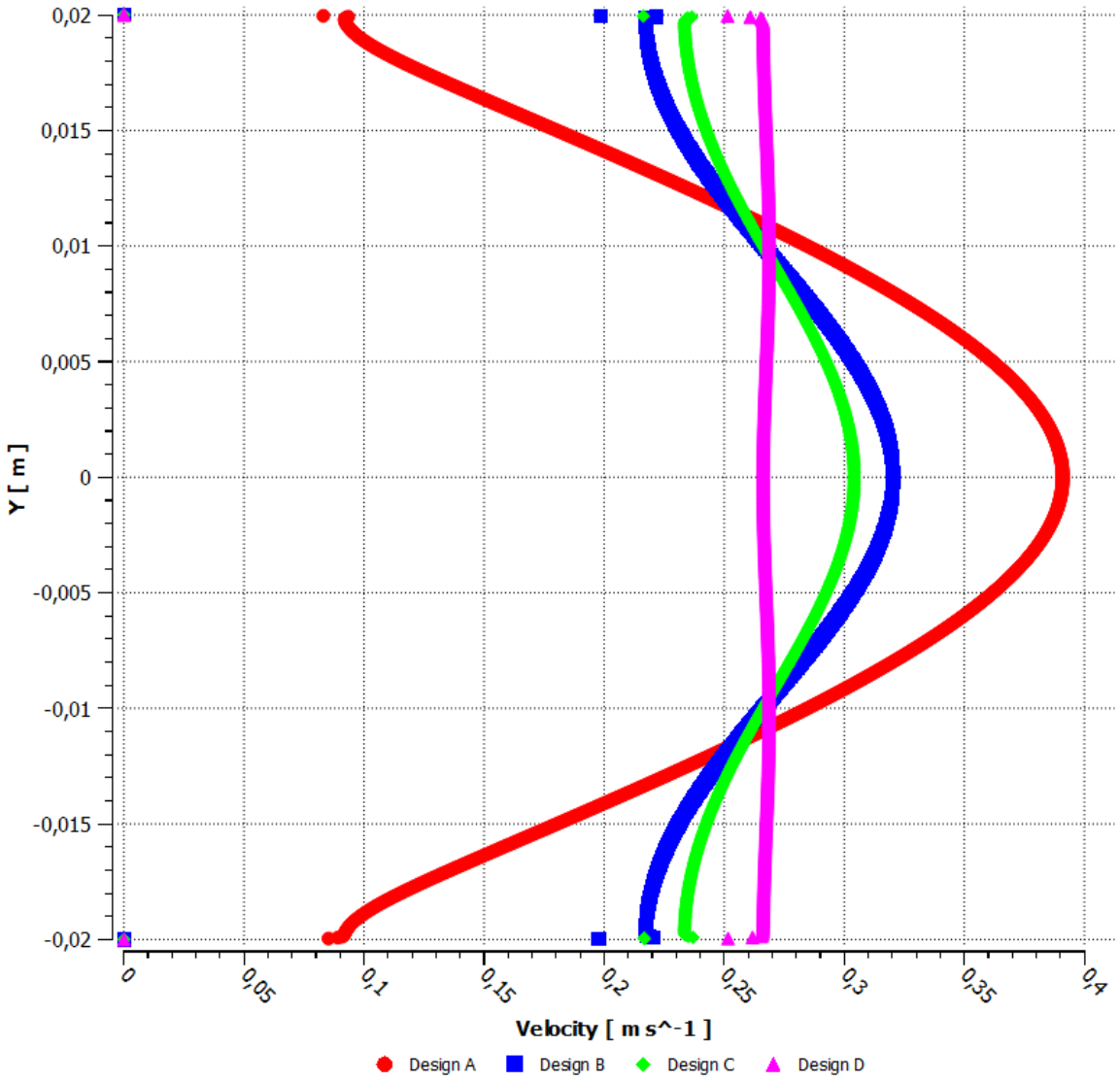

Figure 6.4: Comparison of the outlet velocity profiles of the different designs.

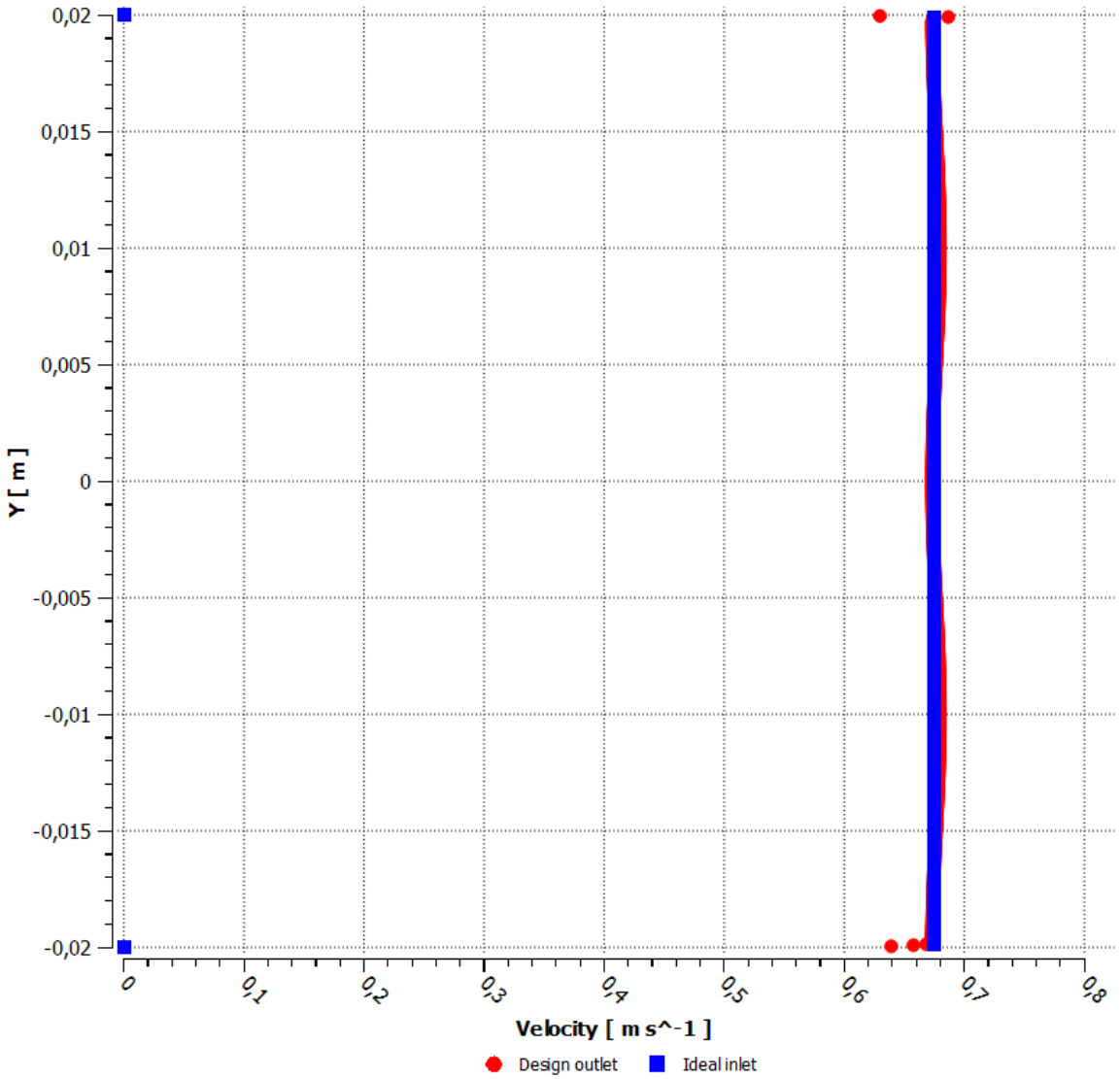

Figure 6.5: Comparison of the inlet distribution of an ideal inlet and the inlet provided by the design

The combination of the z-shaped duct and the flow area led to the design displayed in Figure 6.6 and Figure 6.7. This flow distribution plate design can be implemented in the test station as adapter plate or as a replacement. When the new design is to be used as an adapter plate, channels need to be made on the bottom connecting the flow inlet and outlets of the current flow distribution plate to the inlets and outlets of the new distribution plate. In this case the channels will replace the ducts shown in the figures as cylinders going down.

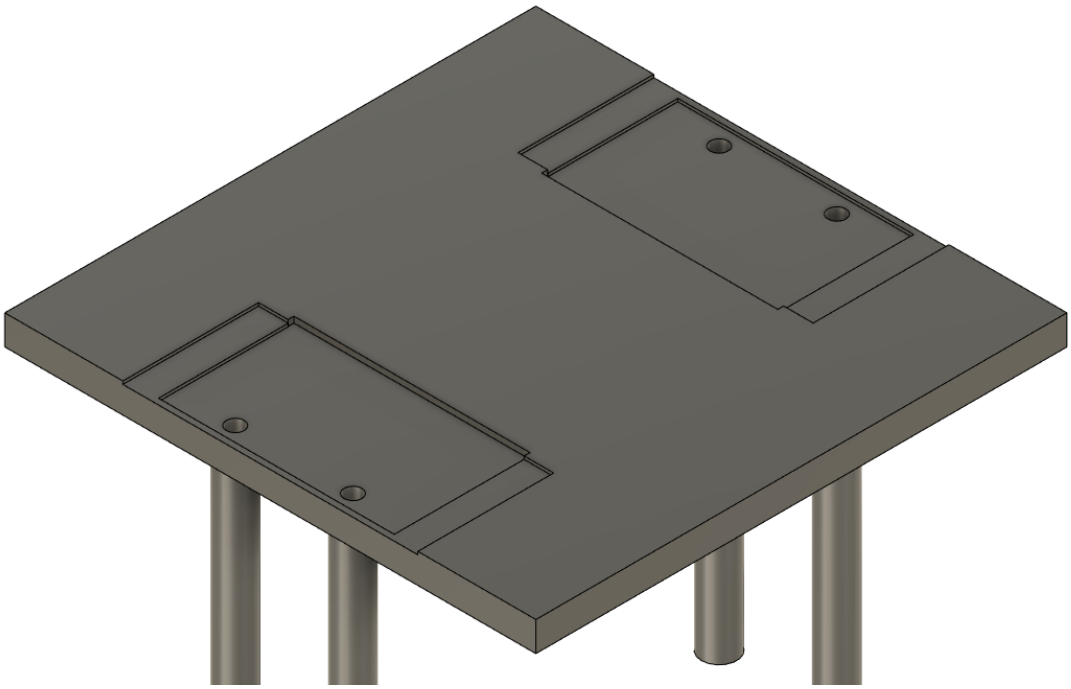

Figure 6.6: Figure of the design without cover plates.

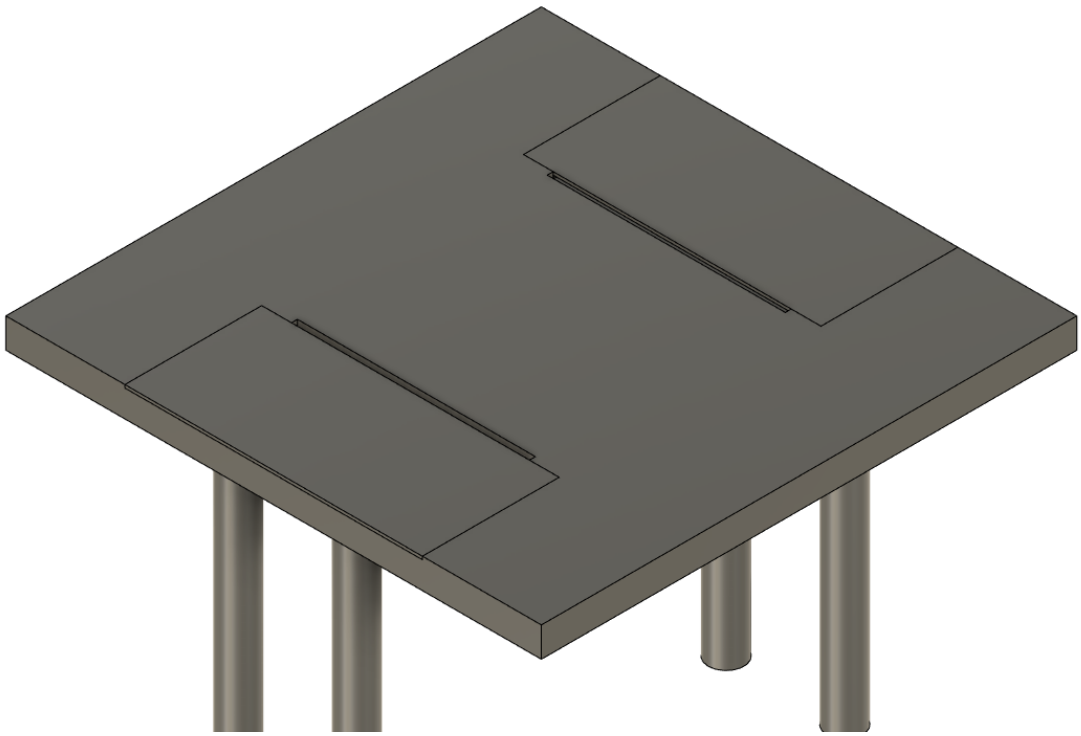

Figure 6.7: Figure of the design with cover plates.

Chapter 7

Results

In this chapter the results of the fuel flow distribution model and the experimental results will be shown. The conclusions of the results will be discussed in the next chapter. The chapter is split into two sections. The first section contains the experimental results indicating the improvement of the test station. Additional results from experiments can be found in Appendix B.
The second section displays the fuel flow distribution model results, where the current densities and fuel utilisation results are displayed for the ideal case and the setup case at high inlet velocities. The reason that these cases in particular are shown is that they correspond to the CFD results seen in Chapter 5. The results of other operating cases are displayed in Appendix C.

7.1 Test station improvement results

In Section 3.2 the original test station configuration is described. This test station was used to test solid oxide cells for the Balance project following an experimental protocol to determine characteristics of the cell which are described in Section 3.1. This protocol consisted of 120 hours of steady state fuel cell operation and 120 hours of steady state electrolysis operation, which is followed by 33 days of cyclic operation, as described in Section 3.1 and shown in Figure 3.1. During the first 6 experiments a problem was encountered. Shortly after the beginning of an experiment the performance of the cell would decrease significantly preventing the experiments to achieve the objectives. The summary of all the experiments is given in Table 7.1. In this table the cell number, which corresponds to the experiment number, the operating temperature, the number of completed cycles and the average current density is given. The percentage in the "completed cycles" column indicate how many of the 33 cycles had been completed before the experiment was stopped. The percentage number in the last column indicates how close to the average current density, during cyclic operation, was to the target current density of the protocol. The current density target was 0.5 A/cm^2 when operating at 750 ^oC and 1.25 A/cm^2 when operating at 700 ^oC. A more detailed description of each experiment is given in the rest of this Section.

Table 7.1: Brief summary of experimental results

cell number	operating temp.	completed cycles[#](%)	average current density[A/cm^2](%)
1	750^{o}C	1 (3%)	0.0375 (7.5%)
2	750^{o}C	1 (3%)	0.0375 (7.5%)
3	750^{o}C	1 (3%)	0.0625 (12.5%)
4	750^{o}C	1 (3%)	0.125 (25%)
5	750^{o}C	3 (9.10%)	0.2042 (40.8%)
6	750^{o}C	0 (0%)	0 (0%)
7	750^{o}C	10 (30.3%)	0.453 (90.6%)
8	750^{o}C	0 (0%)	0 (0%)
9	750^{o}C	21 (63.6%)	0.44 (88%)
10	700^{o}C	14 (42.4%)	0.718 (857.5%)
11	700^{o}C	7 (21.2%)	1.25 (100%)
12	700^{o}C	30 (90.9%)	1.25 (100%)

Experiments 1 to 6 were performed before this research and used the original test station configuration to perform the cell performance measurements. The results of these 6 experiments will be used as a baseline reference to evaluate the improvement of the new configuration of the test station.
From these 6 experiments, the first three experiments where conducted at a current density of 0.04 A/cm^2 and did not complete more than 5 cycles. These experiments were conducted at this relatively low current density because the measurement equipment could not measure current densities higher than 0.04A/cm^2. After experiment number 3 the electronic circuit was adapted to accommodate higher current densities as described in Section 3.2. However, as the first 3 experiments were performed at relatively low current density, the results from these experiments are not discussed further. Experiments with cells 4 and 6 did not complete more than 1 cycle and are thus also not discussed further, as too little data retrieved from these experiments to draw any useful conclusions. This leaves the experiment with cell 5 as baseline reference for further studies. The objective of experiment number 5 was to determine the cell characteristics mentioned in Section 3.1 whilst operating at a current density of 0.5 A/cm^2 during cyclic operation and the associated operating conditions.
The results of the cyclic operation and the first i-v curve measurement of this experiment are shown in Figure 7.1. The constant current operation results will be discussed later in this section. The data for the cyclic operation voltages seen in the figures were obtained by taking the average voltage value over the time the cell ran in that mode. This means the average of approximately 3600 voltage measurements during fuel cell mode and 24000 during electrolysis. The i-v curve data shown in the figures below was gathered by taking the average of 5 voltage measurements, taken at three seconds intervals.

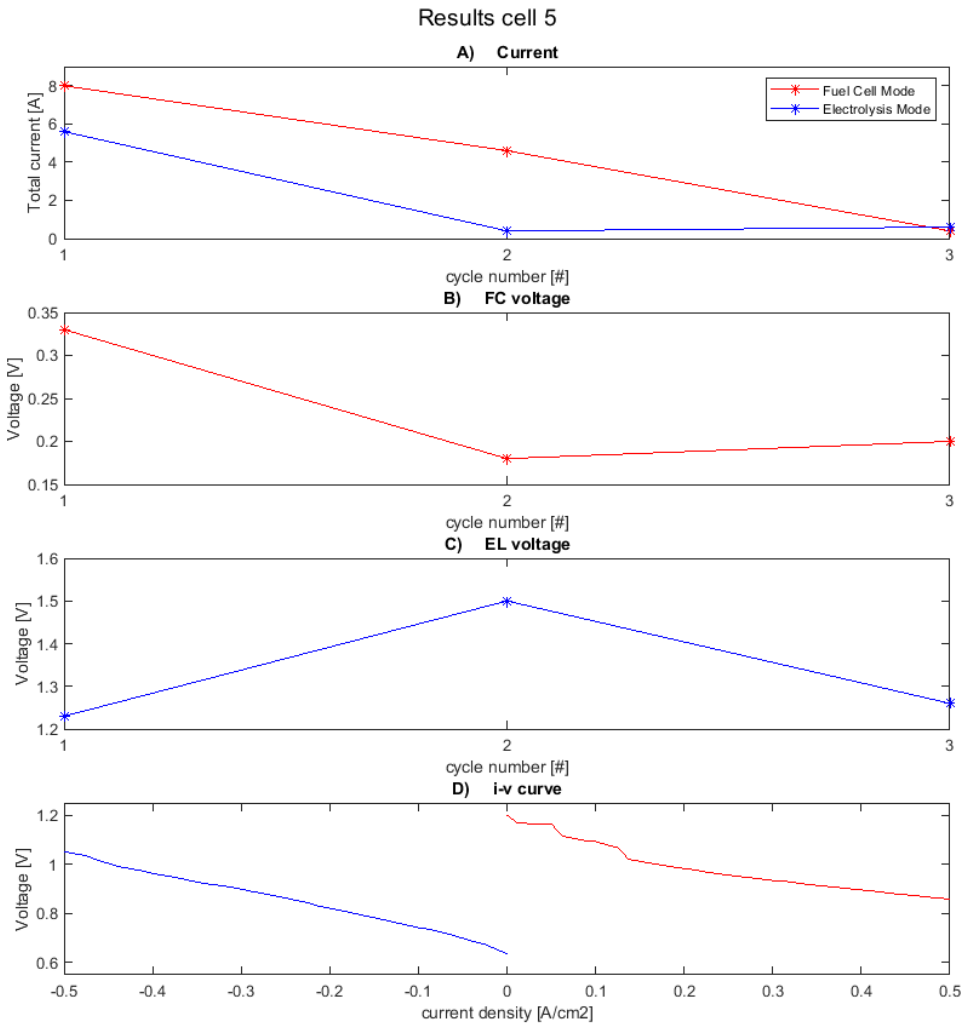

Figure 7.1: Results from experiment number 5.

Figure 7.1A displays the total current going through the cell in both electrolysis and fuel cell operation against the cycle number. A cycle starts with fuel cell operation, for 3 hours, and is followed by electrolysis, for 20 hours, which is why each cycle number has both a electrolysis and a fuel cell voltage.
The cyclic operation begins with fuel cell operation with a current of 8 ampère (0.5 A/cm^2). For cycle 2 this total current in fuel cell mode is reduced to 5.6 ampère and in cycle 3 it is even further reduced to 0.4 ampère. The cause of these current reductions is the operational voltage of the

cell. The operational voltage is the potential difference between the fuel and air electrode, which is determined by the summation of the Nernst potential and the overpotentials, as is explained in more detail in Chapter 2 in Equations 2.7 to 2.17. This potential difference is what is measured by the voltage measurement system in the test station described in Section 3.1. In Figure 7.1B the operational voltage of the cell during fuel cell mode is displayed. This graph shows that the operational voltage of the cell in cycle 2 had reduced to 0.18 volt when the total current was increased from 0 to 5.6 ampère. This operational voltage of 0.18 volt prevented the current to increase to the desired total current of 8 ampère, as this voltage could not be reduced further without damaging the cell, as explained in Section 3.1. In cycle 3 the operational voltage had reduced to 0.2 volt when the current was increased to 0.4 ampère, limiting any higher current outputs for the same reason.
The operational voltage during electrolysis is shown in Figure 7.1C. The operational voltage during electrolysis in the first cycle was manually limited to 1.25 volts, as a reaction to the low operational voltage during the fuel cell operation in that cycle. At the voltage limit the cell operated at a current of 5.6 ampère (0.35 A/cm^2). This indicates a 32.5 percent increase in voltage compared to the voltage value found at the same current density during i-v curve measurement. As this degradation rate is too high to complete all 33 cycles, the voltage was not increased further in an attempt to curb the degradation rate. This proved to be not effective, as during electrolysis in the second cycle the voltage had risen to 1.5 volts, while the current had only increased from 0 to 0.4 ampère. Because of his high voltage increase at a relatively low current increase in the second cycle, it was decided not to increase the current, and thus the operational potential, any further as the desired 8 ampère was not going to be reached within the operational voltage limit. In cycle 3 electrolysis performed relatively better, compared to cycle 2, as the voltage had risen to 1.26 volt when the current was increased from 0 to 0.6 ampère. It was decided not to increase the current any further in this cycle as well, because of the same reason in cycle 2.
The experiment was stopped after three cycles because the Balance protocol prescribed 0.5A/cm^2 current density was not going to be met in either operational mode within the specified upper and lower voltage limits of 0.4 and 1.7 volts.
In Figure 7.1D the initial i-v curve of experiment 5 is shown, which is the first measurement taken during the experiment. The i-v curve measurement is done to assess the operational potential of the cell for current densities varying between 0 and 0.5 A/cm^2, as this gives an indication on how the cell performs in both modes. This also provides a baseline to measure performance degradation over time against, as between the initial i-v curve measurement and the first cycle the cell has operated 120 hours in fuel cell mode and in electrolysis mode, respectively. The difference between the i-v curve measurement and the first cycle therefore give the degradation over these constant current operation sections of the protocol.
Figure 7.1D shows that the performance of the cell is significantly better during the i-v curve measurement compared to the performance seen during the first cycle of the cyclic operation. The fuel cell operation in the first cycle was performed at 0.33 volt, compared to the 0.86 volt during the i-v curve measurement at the same current density. This is a voltage loss of 62$\%$. As stated above the electrolysis performance dropped by, at least, 32.5% when comparing the first cycle electrolysis performance to the i-v curve measurements. These losses indicate that during the constant current operation a significant portion of the performance is lost.

No significant drop in performance was measured over the duration when the cell was operating in fuel cell mode with a constant current. During electrolysis however, an average degradation

was measured of approximately 1 millivolt per 25 minutes of operation. This difference in degradation rate is the reason how the electrolysis operation was identified as the source of the high degradation rate of the cells. The investigation therefore examined the electrolysis data of the constant current operation section more closely. In Figure 3.9 the data of the first hour of electrolysis during constant current operation is displayed. In this figure voltage spikes, of 20 millivolt, were found. These spikes occurred approximately every 45 minutes in the voltage reading. The voltage returned to the values seen before the spike over a relatively long time. If the spike had returned to the values before the spike in the next measurement, it could have been dismissed as a measurement error. However as the reduction of voltage happened over a relatively long time, it indicated a problem.

The explanation for the voltage spike and the time taken to return to the values seen before the spike, was found by identifying the variables that influence the voltage. These variables are found in the Nernst and overpotential Equations 2.7 to 2.17. From these equations it can be determined that the voltage spike down seen in Figure 3.9, can be caused by, among other things, an increase in temperature, increase in reactants and change in material properties. From these variables the change in reactants was deemed most plausible. During electrolysis, this means that the water concentration level fluctuated.

The water is injected via an injection needle into the inlet duct approximately 40 centimeters above the cell inlet, as displayed in Figure 3.8. The injected liquid water travels down a cartridge and thermocouple where it is evaporated. A cartridge is shown in Figure 3.7. In Chapter 4 it is calculated that a water droplet should evaporate within the length of the cartridge, if a cartridge is the sole component in the inlet duct. In the original test station configuration there is a thermocouple mixed in with the cartridge, it is therefore assumed that liquid water could accumulate on the temperature sensor and reach on the cell surface from there, as explained in more detail in Chapter 4. Once a droplet reaches the fuel electrode, it quickly vaporises with the heat contracted from the cell. This increase in water concentration on the cell electrode decreases the nernst potential, Equation 2.7, and the overpotentials from concentration and activation, Equations 2.12 to 2.17. This decrease is seen in the spikes down in the voltage graph in Figure 3.9. Droplets evaporating on the cell electrode also explains the steep rise in voltage after the spike down. As the concentration from the evaporated liquid water is exhausted from the cell, the voltage is expected to return to the values before the spike. However, as the droplet contracted heat from the cell the cell temperature is locally lowered, and a temperature gradient is created. This lowering of the temperature increases the Nernst potential and the ohmic overpotetial, Equation 2.9, explaining the voltage spike up. After the voltage spike up the cell heats up again. With the gradual heating up of the cell the Nernst potential and the ohmic overpotential reduce again and the cell is back to the potential before the initial spike, after approximately 45 minutes.

The rapid degradation is explained in this scenario by the temperature cycles and the reoccurring temperature gradient in the cell. These degradation mechanisms are explained in more detail in Section 2.2. Both of these mechanisms are known to cause cell failure as seen in Figure 3.10 and 5.1.

As this hypothesis fits the results seen from the electrolysis data and the post mortem investigation, the water injection system needed to be redesigned. The redesign had to incorporate a thermocouple temperature sensor at the cell inlet and a cartridge to evaporate water, without interfering each other. This design process is described in Chapter 4.

The redesign of the water injection system was therefore implemented into the test station, which

is referred to as the new configuration. In Chapter 4, it is shown that during the first hour of electrolysis operation the voltage fluctuation was reduced from 5 to 1.5 millivolt, a reduction of 70%. More importantly, the spike seen with the previous water injection system were completely removed and the cells were retrieved from the test station after experiments in one piece. In the discussion of the data from experiments 10 to 12 it will be shown that the high degradation during electrolysis has been minimised as well. This indicates that the hypothesis presented above was correct and that the redesign solved the problems that were encountered.

Experiments 7 and 9 were conducted with the same generation cells and followed the same experimental protocol as experiment 5, but completed 10 and 20 cycles respectively. Experiment 8 incurred experiment ending damage due to a exhaust duct failure before the experiments had began and is therefore omitted in the report. The most important difference between the experiment numbers 7 and 9, compared to experiment 5, is the fuel inlet duct was fitted with a p-trap. This p-trap prevented liquid water to enter the flow distribution area and thus from reach the cell surface. The fact that experiment duration with cell numbers 7 and 9 was significantly extended, ruled out that the cells were the limiting factor for the experimental duration. These experiments also confirmed the assumption that water condensation in the fuel inlet duct was the problem that was encountered in the baseline experiments.
Experiments 7 and 9 were also conducted with water injection systems to validate the calculations done in Chapter 4. Experiments 7 and 9 will therefore not be further mentioned in this chapter. Their experimental results are shown in Appendix B. Experiments 10, 11 and 12 were conducted with the water injection system that was designed in Chapter 4. The results of experiments 11 and 12 are shown in this chapter in Figures 7.2 and 7.3. The experimental results of cell number 10 are shown in Appendix B, as during the experiment an issue was encountered rendering the experiment unrepresentative.

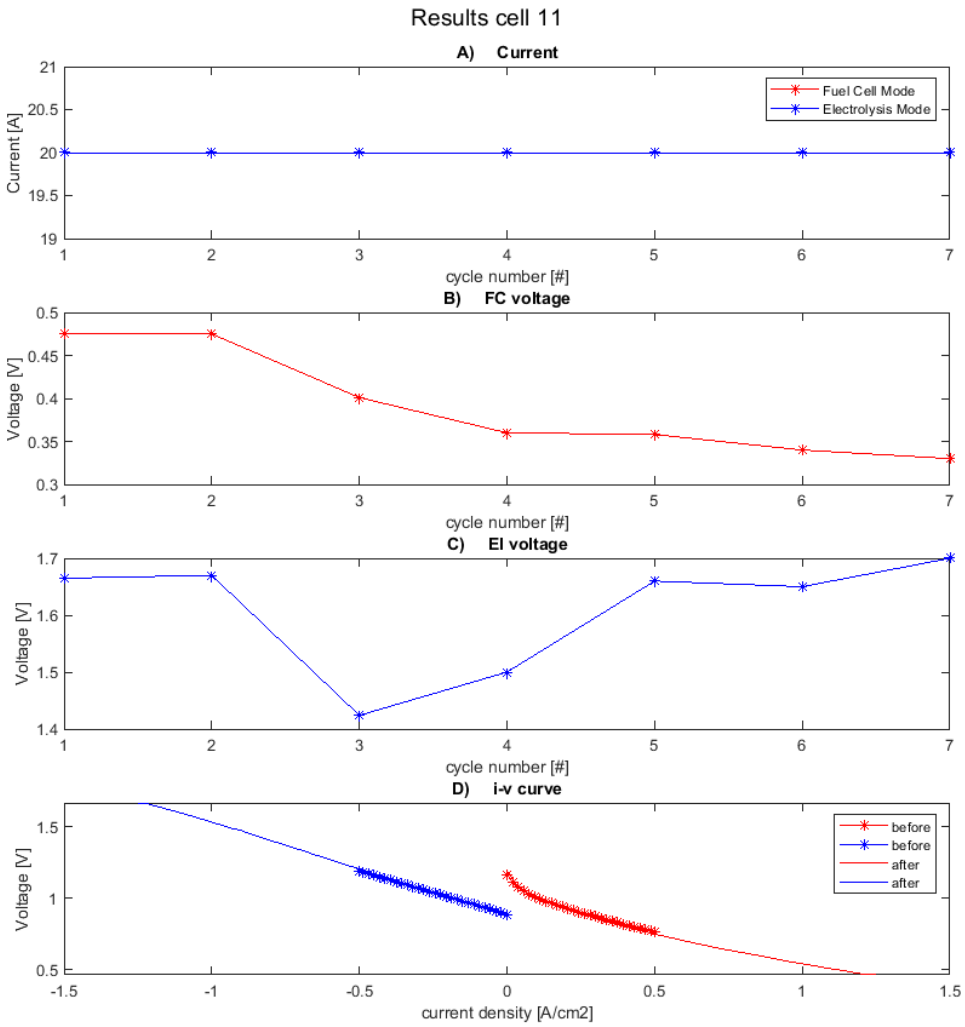

Figure 7.2: Results from experiment number 11.

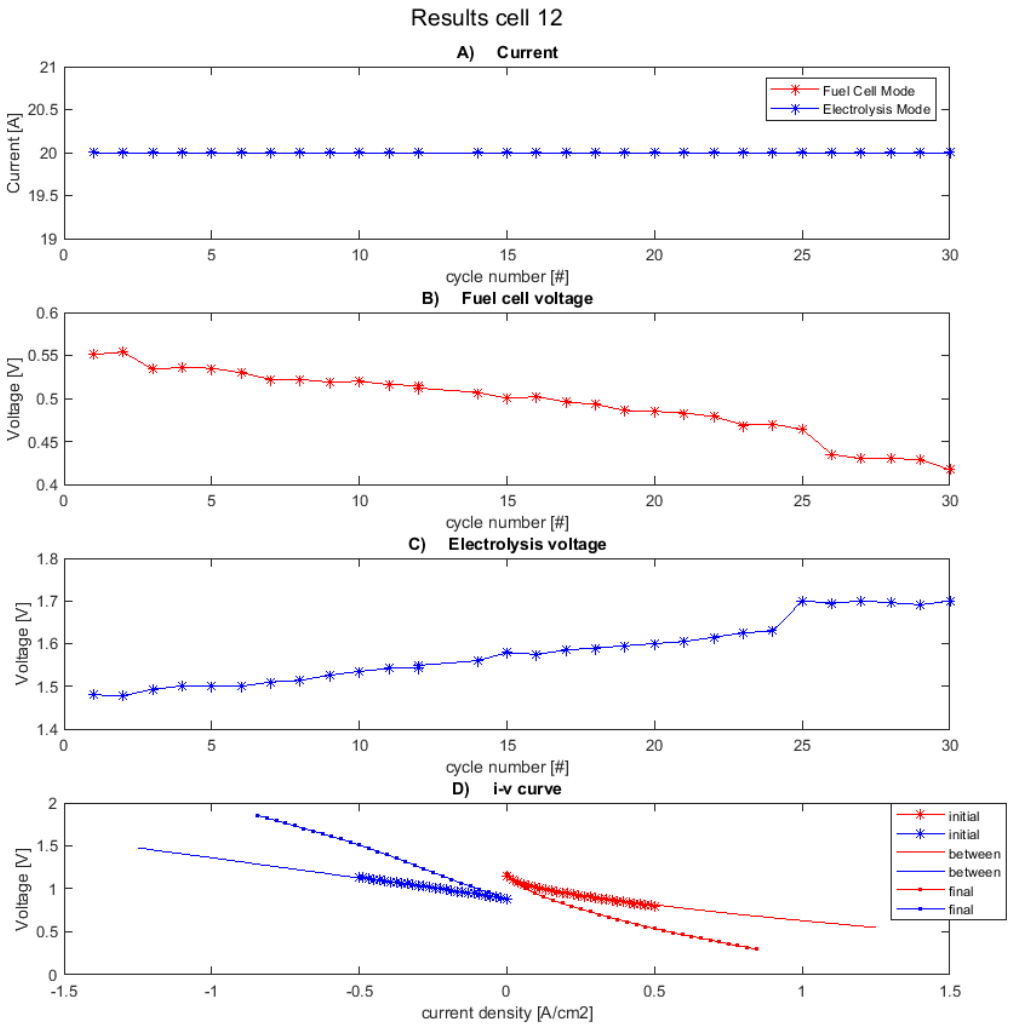

Figure 7.3: Results from experiment number 12.

Figures 7.2A and 7.3A, show that both fuel cell and electrolysis modes were conducted at 20 ampère (1.25 A/cm^2) in every cycle for both experiments. The operational voltage during fuel cell, shown in Figures 7.2B and 7.3B and for electrolysis in Figures 7.2C and 7.3C. As the current is equal between the experiments these operational voltage graphs give a good comparison between the experiments.
In Figure 7.2B, it is seen that during cycle 3 the voltage dropped below 0.4, which is the lower limit of the Balance experimental protocol. The experiment was continued despite the fuel cell operation

voltage being lower than the prescribed minimum, to identify the point where the electrolysis operational voltage would exceed the prescribed maximum. In Figure 7.2C the operational voltage during electrolysis exceeded 1.7 volt during cycle 7. With both the fuel cell and the electrolysis operational voltage exceeding the voltage limits set by the protocol, the experiment was stopped.
In Figure 7.2D two i-v curves are displayed. One is done before and one is done after the constant current operation sections. As the system has run both operational modes for 120 hours in between the time the two i-v curve measurement were taken, the difference between the i-v curves indicate the degradation over these modes combined. As the i-v curves are nearly fully overlapping, the degradation compared to experiment 5 is significantly reduced. This result, combined with the reduction in fluctuation, indicates that the redesigned water injection system minimises the effect of the test station on cell performance degradation by eliminating the condensation problem.

Figure 7.3 displays the results of experiment 12 and a similar story as the results from experiment 11. In Figures 7.3B and 7.3C the operational voltages during fuel cell and electrolysis mode are displayed. During this experiment the voltage degradation per cycle was significantly lower compared to experiment number 11, allowing the cell to run for 30 cycles. The experiment was stopped after 30 cycles as a human error was made during the switching of the operational modes during cycle 31, causing the cell to operating in fuel cell mode without hydrogen. This event caused the cell performance to decrease. This decrease in performance cause the operational voltages to exceed the protocol limits in both modes.

In Figure 7.3D, three i-v curves are displayed. One i-v curve measurement is done before and one after the constant current operation section. The last i-v curve measurement is taken after the 30 cycles where completed, which is named "finial" in the graph. The i-v curves taken before and after constant current operation show relatively little difference, as seen in experiment number 11 as well. This result indicates that the degradation over both steady state operations is shown to be relatively low, confirming that the high degradation due to the water injection system is greatly reduced.
The difference between the i-v curves named "after" and "final" in Figure 7.3D, shows the overall degradation sustained during cyclic operation in experiment 12. However, only a part of this degradation is actually sustained due to the cyclic operation. In Figures 7.4 and 7.5 a more detailed picture of the degradation is displayed, where the degradation of fuel cell and electrolysis operation is displayed in millivolt per cycle. In these figures the black line represents the cumulative degradation and the blue line the degradation per cycle.
In Figure 7.5 a degradation spike is seen in cycle 25 and in Figure 7.4 a spike is seen in cycle 26. These spikes are caused by a water pump failure during electrolysis operation in cycle 25. The water pump failure caused a lack of water flow to the cell during electrolysis operation. This lack of water supply during electrolysis meant that the Nernst potentials and overpotentials worsened, leading to a higher operational voltage for the operation in this cycle. However, it also had an effect on the total degradation, as Figure 7.3C shows that the voltage did not improve back to the original voltages after the pump had been repaired in cycle 26. Figure 7.4 shows that the fuel cell mode following the event also suffered high degradation. The reason for this degradation is assumed to be the lack of oxygen transport during electrolysis in cycle 25. It is assumed that, because the current was kept constant in the system by the electronic subsystem displayed in Figure 3.6, a mismatch was created between the number of oxygen ions available for transport

through the electrolyte and the current in the cell. This mismatch could be damaging to the cell. However, more research is needed to determine the precise degradation mechanism that occurred during this event.
During cycle 31 a human error occurred during the switching of the operational modes, causing the cell to briefly operate without hydrogen during fuel cell operation. During this event more oxygen ions where transported through the electrolyte compared to the available hydrogen at the fuel electrode. Because of this shortage of hydrogen, the oxygen ions reacted with the nickel in the fuel electrode, which is known as oxidation. When hydrogen was re-introduced at the fuel electrode, the oxygen from the fuel electrode reacted with the hydrogen. This process is known as the reduction of the fuel electrode. This cycle of oxidising and reducing the fuel electrode is known to damage the performance of a cell, as explained in Section 2.2.
Both these events added to the degradation due to cyclic operation. This total degradation is seen as the difference between the i-v curves in Figure 7.3D. As the degradation in this graph is a combination of factors, it is not straightforward to deduce the degradation due to cyclic operation from this graph. In Figures 7.4 and 7.5 the degradation is seen per cycle and the degradation across the first 24 cycles is on average 4.46 millivolt per cycle for fuel cell operation and 8.27 millivolt per cycle for electrolysis operation. As this result of degradation due to cyclic operation is taken before the events that impacted cell performance, it gives a better representation of the degradation due to cyclic operation compared to taking the difference in i-v curves from Figure 7.3.

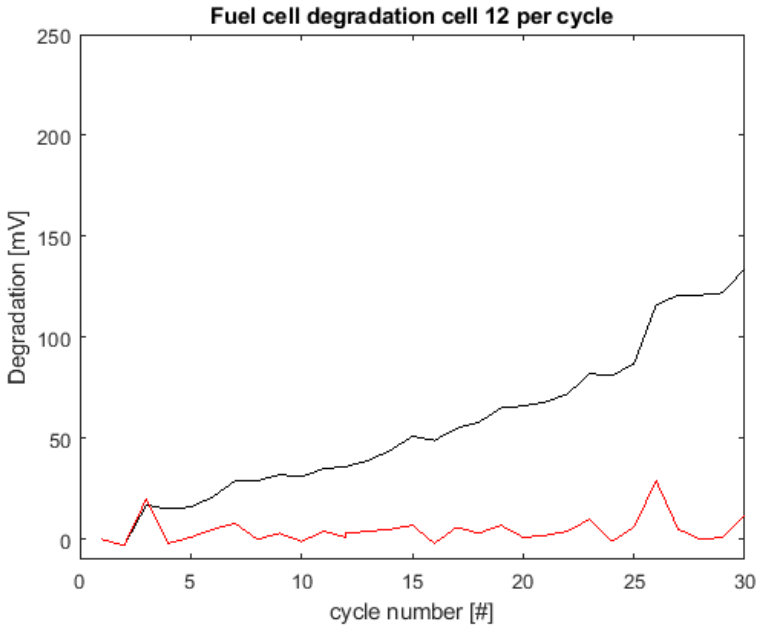

Figure 7.4: Fuel cell mode degradation of experiment number 12 per cycle.

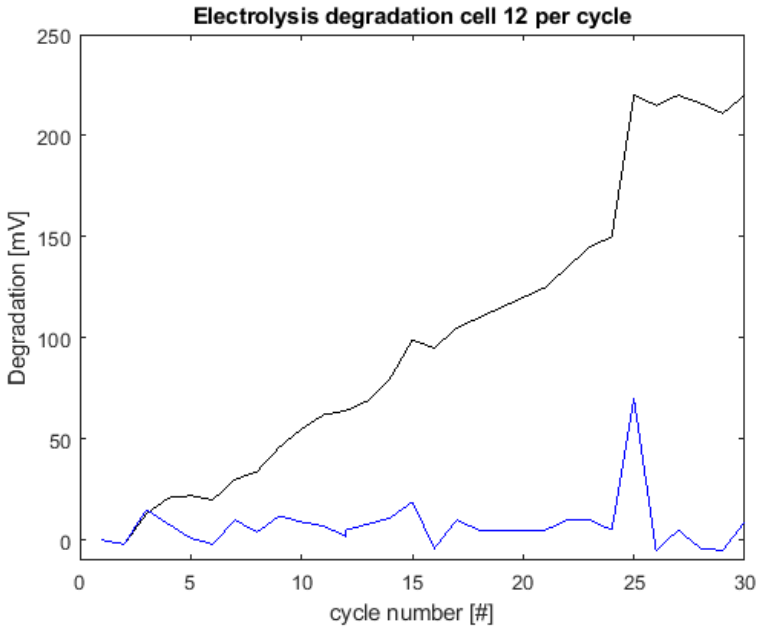

Figure 7.5: Electrolysis mode degradation of experiment number 12 per cycle.

From the results shown above, it is clear that both the original and the new test station configurations were able to assess initial fuel cell and electrolysis performance of a cell by measuring an i-v curve at the beginning of the experiment, as seen in Figures 7.1D, 7.2D and 7.3D. A performance degradation over time could also be measured by both configurations of the test station, as both completed the 120 hours of constant current operation for both modes. However, the new configuration test station with the redesigned water injection system showed significantly less degradation with the same generation cells and operational conditions. This difference indicates that the original test station configuration had influenced the results of the cell measurements.
The other objective stated in Section 3.1, determining degradation due to cyclic operation, could not be measured in the original test station configuration. Because the experiments did not reach the prescribed current densities within the operational voltage limitations during cyclic operation or completed enough cycles to determine a degradation rate. In Figures 7.4 and Figure 7.5, shown in the section above, it is shown that the elongated experimental duration, due to the redesigned water injection system, allowed the new configuration test station to determine the performance degradation per cycle due to cyclic operation.

To quantify the improvement of the changes made to the test station experiment number 5 is compared to experiment 12, as shown in Figure 7.6. In Figure 7.6A the initial i-v curves are compared. The performance during the initial i-v curve measurement of cell 5 is better than that of cell 12, as the i-v curve shows a higher voltage at the same current density during fuel cell operation. During electrolysis operation lower voltages are seen at the same current density, also indicating

better performance. This performance difference is due to the higher operating temperature of 750 degrees Celsius for cell 5, compared to 700 degrees Celsius for cell 12. The causes for the increase in performance is explained in detail in Chapter 2.
In Figure 7.6B the voltage for both operational modes per cycle is shown. From this graph it can not be stated if the experiment with cell 5 or 12 performed better. The voltage graph should not be taken as performance indicator on its own when current is not constant and equal between the experiments. In this case it should be combined with the current density data, as is also done with i-v curves. The current graph for both operational modes for both experiments is shown in Figure 7.6C. This graph shows that the current during both operational modes during experiment number 5 drops to nearly 0 within 3 cycles, where as the current during both operational modes in experiment 12 stays at 20 ampère for 30 cycles. Combining the graphs that show voltage and current, it can be stated that cell 12 has superior long term performance as it performed more cycles within the specification of the experimental protocol.
This performance difference shows that the new configuration of test station extended the experimental duration by 900%, whilst the current density target was increased by 150%.

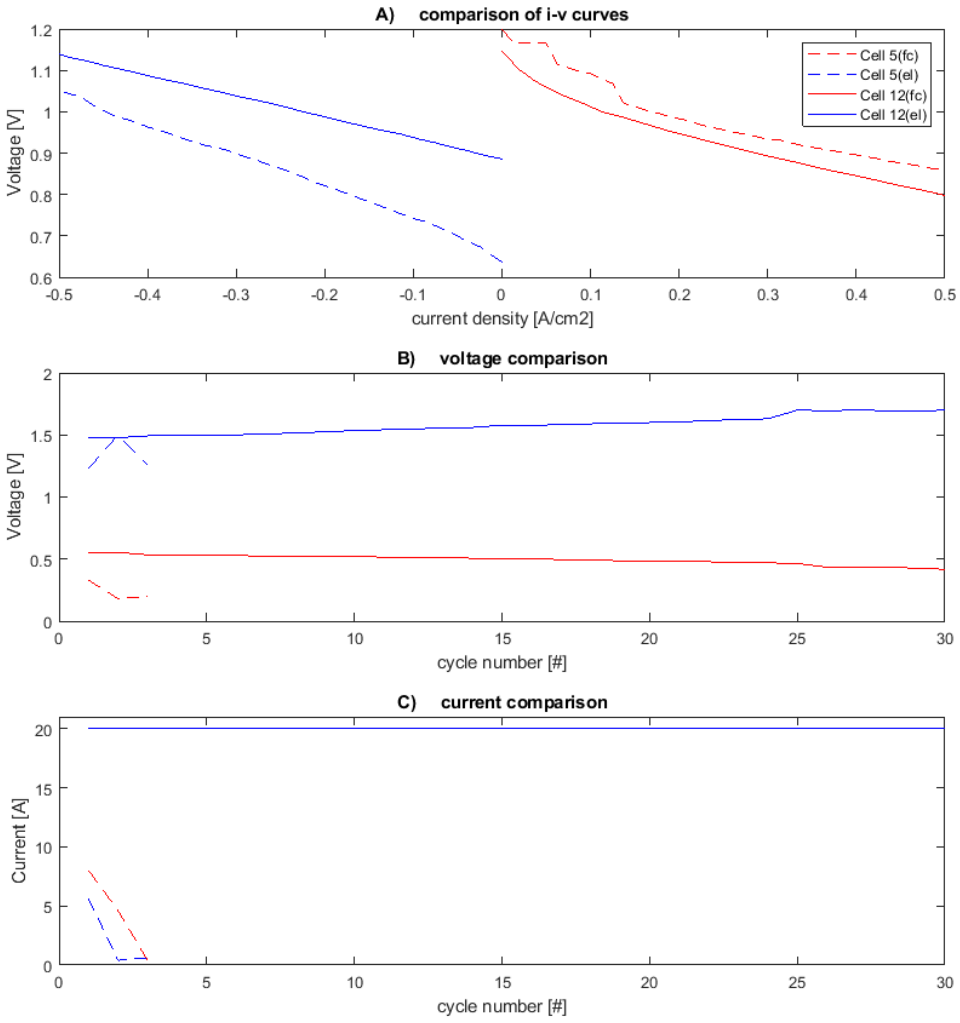

Figure 7.6: Comparison of experiment number 5 to experiment number 12.

In addition to the extended experimental duration, the reliability was also improved by implementing the redesigned water injection system. Because the cell performance degraded relatively quick during the experiments 1 to 6, the reliability of the experiment was low. This means that the performance of the different cells can not be compared, as the experimental execution differed from experiment to experiment. This difference is mentioned in the beginning of this section, where all experiments ran at different currents compared to each other and even from cycle to cycle. With the improvement due to the water injection system, this reliability is improved

to the point were different experiments can be compared, as shown below.
When looking at the results from experiment number 11 and 12, displayed in Figure 7.7, a difference of performance can be seen. Figure 7.7A shows the difference in performance with the initial i-v curve, which were performed under the same operating conditions. In this graph experiment number 12 showed better performance as voltage is higher at the same current density in fuel cell mode and lower for the same current density in electrolysis mode.
Figure 7.7B shows the difference in operational voltages per cycle during cyclic operation. The operational voltage difference is a good indicator of the performance difference between the cells in this case, as both experiments operated at a constant and equal current, as shown in Figure 7.7C. The operational voltages during experiment number 11 exceed the prescribed minimum and maximum in 7 cycles. This means that experiment number 12 performed better, compared to cell number 11, as the prescribed minimum and maximum where not exceeded in experiment number 12 until cycle 30. This figure also shows that the degradation rate is higher for cell 11 compared to cell 12.
With both experiments mentioned above following the same protocol under the same operational conditions, a performance difference could be measured between the cells in the test station with the redesigned water injection system.

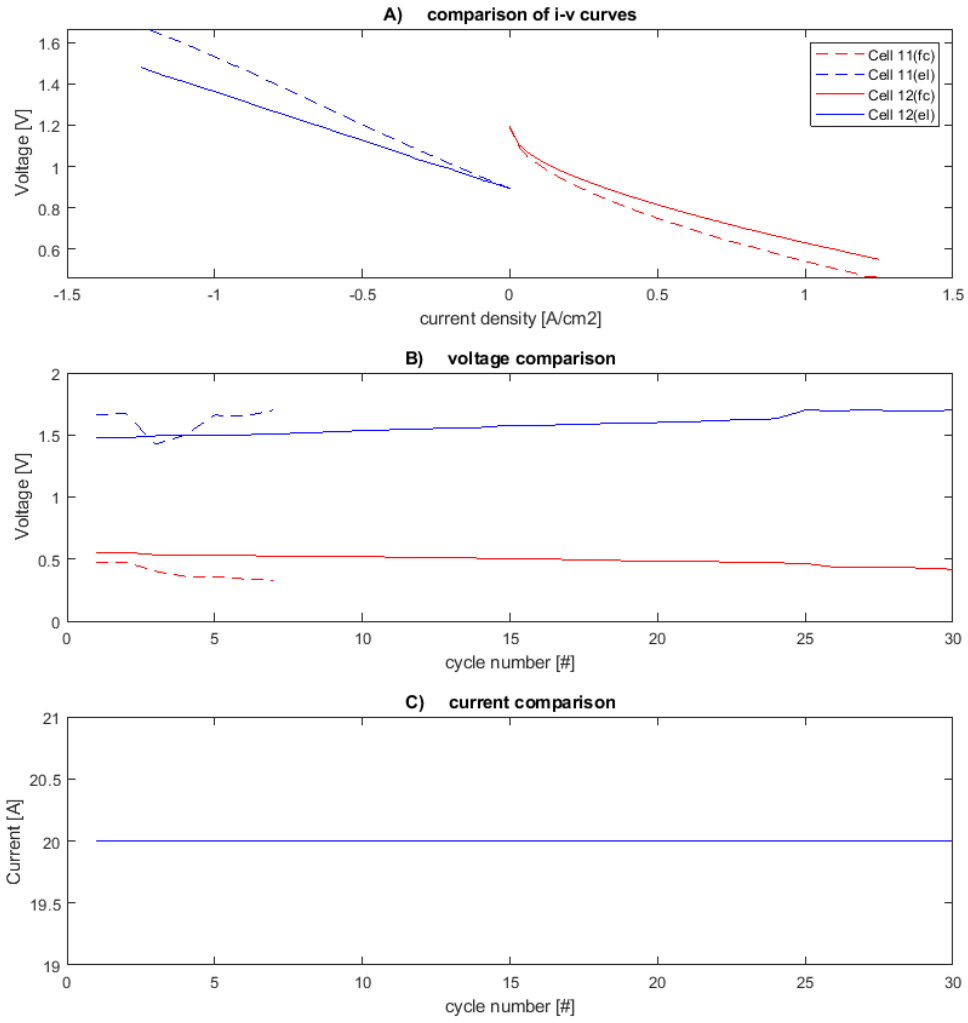

Figure 7.7: Difference between experiment 11 and 12.

7.2 Fuel flow distribution model results

When investigating the cause of the high performance degradation, it was discovered that the cells had markings on the fuel electrode. These markings are shown in Figure 5.1. It was assumed that these markings indicated the flow pattern of the fuel flow. A 2D CFD analysis of the fuel flow distribution showed streamlines with a similar pattern, seen in Figure 5.17, as the markings

seen on the fuel electrode, the assumption was not rejected. The CFD anlysis also indicated that the flow distribution in the test station was significantly different from those seen in literature, as described in Chapter 2 and 5. The fact that very low velocities were found in the velocity data of the 2D CFD anlysis led to the formation of the hypothesis that the fuel flow distribution across the cell due to the flow distribution plate of the test station has a significant impact on the cell performance measurements. To investigate the hypothesis, a model was made to convert the CFD data to current density and fuel utilisation data. Due to time constraints the model only simulates fuel cell operation conditions and only the fuel flow distribution is take into account, the air distribution on the air electrode is assumed to be non restrictive to performance. The results of the model simulating the test station case are compared to a fictional case, where the flow distribution is derived from what is seen in the literature review. With this comparison the hypothesis can be rejected or deemed plausible. In this section the flow distribution due to the flow distribution plate in the test station will be referred to as the setup case. The flow derived from literature is referred to as the ideal case.
The results from two case studies, the ideal case and the setup case with volume inlet flows associated with operation at 1.25 A/cm^2 current density, are displayed in this section. The other results are displayed in Appendix C, as they show the same trends as the ones showed in this section.

How the model converts the 2D CFD data to current density and fuel utilisation is described in detail in Chapter 5, in this section a brief description is given.
The streamline data from the CFD analysis is loaded into the matlab program as x,y coördinates and streamline numbers. All the coördinates with the same streamline number form a single streamline. These streamlines are sorted by the program to ensure that streamline 1 and 2 are neighbouring streamlines. This step is important as the program is going to make segments between the streamlines. These segments act as mesh elements during a CFD analysis. For each element the current density, mass conversion, mass inlet, mass outlet and fuel utilisation is calculated. The inputs for each segment come from the previous segment and the results of the segment are passed on to the next segment. To make the calculations easier to solve, the segments are made between two streamlines from the CFD analysis. The assumption is made that the system is in steady state, as well as uniform in temperature. When the system is in steady state no mass crosses the streamlines and as uniform temperature is assumed there is no heat transfer between segments. These assumptions makes calculations easier as the segments between streamlines the can be solved sequential, streamline per streamline.
To calculate the current density, mass conversion, the mass in and output and the fuel utilisation for each segment, an equipotential SOFC model is used, as described in Section 5.2.2. This model solves the Nernst potential and overpotential equations, seen in Section 2.1.3, with an iterative loop. In this iterative loop a high current density is given as an initial value and is lowered per iteration. The iterations stop once the operating potential, calculated with Equation 2.8, is equal to or greater than the user specified value. This method of obtaining the current density per segment is faster than using a system of equations solver for each segment, as the calculation duration decreased from 0.5 seconds per segment to 0.02 seconds per segment, an reduction of 96% computational time. This reduction comes at the price that the voltage is allowed to fluctuate 0.01% between segments, the voltage fluctuation is assumed to be acceptable in this research. The results of this program are displayed below.

Figures 7.8 and 7.9 display the model results of the current density resulting from that of a more ideal flow and from the flow distribution plate in the test station, respectively. Figure 7.8 shows a higher current on the inlet, on the left side, compared to the outlet, on the right side, which is expected. As the reacting species are consumed and products are produced, the Nernst potential is lowered and the concentration portion of the overpotentials grows, which is explained in more detail in Chapter 2. This causes the current density to go down as the cell is operated under equipotential conditions. A similar effect is seen in Figure 7.9 where the current density is highest at the inlet and decreases towards the outlets.
However, as the streamlines in the setup case diverge near the corners of the cell area, large area's with low current densities are seen. These low current densities are explained by the fuel utilisation plot in Figure 7.10. As mass flows outwards from the inlet, reacting species get consumed. Because the mass flow moving to the corners needs to travel more distance to the outlets compared to the flow going to the outlets directly, more reacting species get consumed and thus the current densities are lower. This is compounded by the fact that as streamlines diverge near the corners, more area is covered between the streamlines further lowering the concentration of reacting species. These effects add up to the result displayed in Figure 7.10, where the fuel utilisation in the corners rises to between 80 and 100 $\%$. In contrast, the more ideal case does not exceed 60$\%$ fuel utilisation, as shown in Figure 7.11. This fuel utilisation difference between the case studies led to the result that the current density in the setup case drops below 500A/m^2 and the more ideal case stays above 1000A/m^2.
The anomalies, the dark blue dots and scrambled lines, seen in the figures below were not found in the data produced by the model and therefore do not influence the results of the model. It is assumed that because the program Matlab is plotting nearly a million data points on a small area some graphical, or compression, errors have happened resulting in the anomalies seen in the figures.

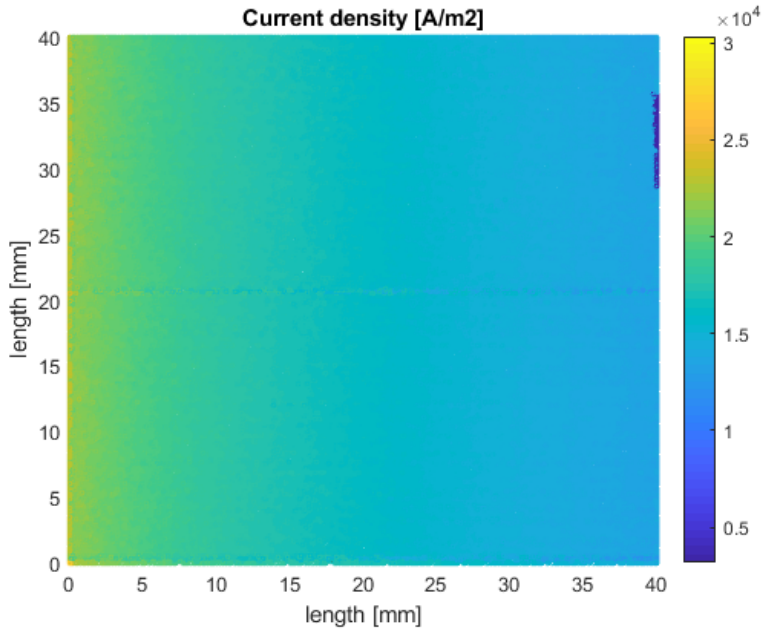

Figure 7.8: Current density results for the ideal case with an inlet velocity of 0.675 m/s.

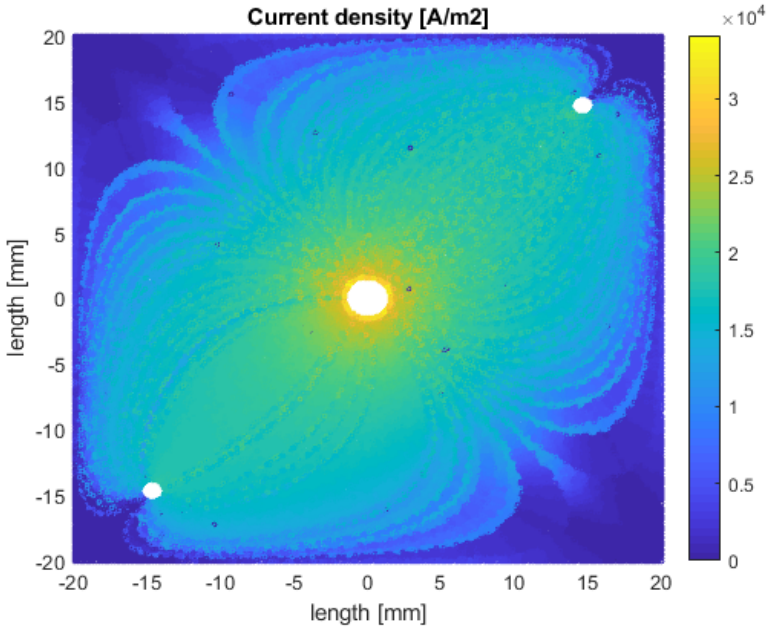

Figure 7.9: Current density results for the setup case with an inlet velocity of 2.7 m/s.

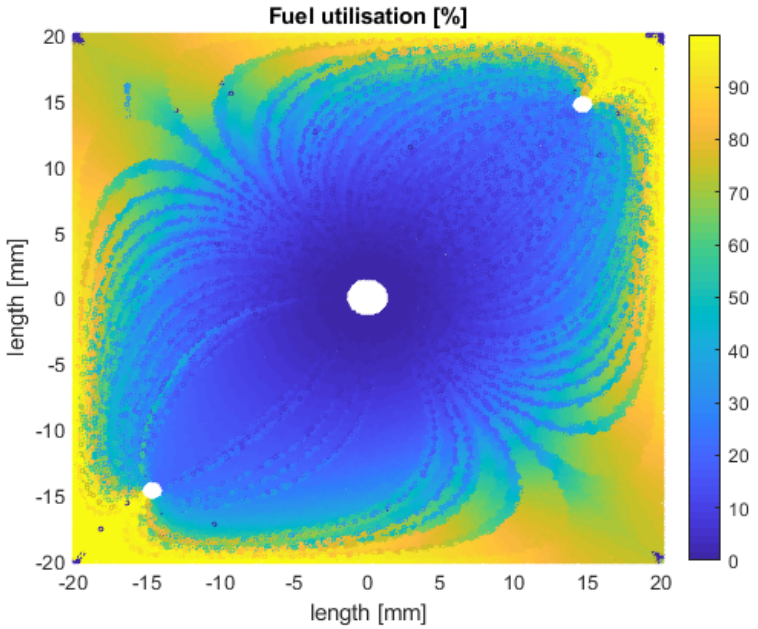

Figure 7.10: Fuel utilisation results for the ideal case with an inlet velocity of 2.7 m/s.

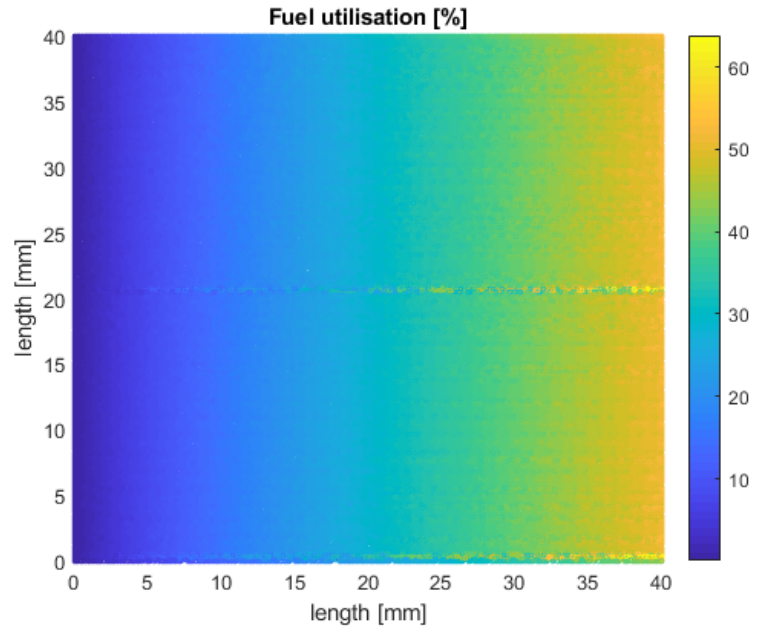

Figure 7.11: Fuel utilisation results for the ideal case with an inlet velocity of 0.675 m/s.

The overall results of the conversion model for all 8 case studies are displayed in the two tables below. These tables display the total cell current, fuel utilisation, mass inlet error and the improvement. The total current is calculated by a summery of all current density data from the segments multiplied by their respective area. The fuel utilisation is calculated as the percent difference of the inlet mass flow of reacting species compared to the outlet mass flow of reacting species. The improvement is the difference in total current output between the particular case study and the setup case for that operational point.
However, because of how the CFD analysis is performed in the setup case, the inlet and outlet area are not included in the analysis. The fuel utilisation and current density results therefore needs to be corrected for these areas. The reason for the way the CFD is performed is explained in more detail in Chapter 5.
For the current density this correction is done by multiplying the average of the current density of the first and last segments with by the area of the inlet and outlet, respectively. The fuel utilisation is corrected by adding the mass conversion of reactive species due to the extra current density at the inlet and outlets to the total converted mass of reactive species calculated by the model.
As the mass conversion on the inlet surface area is not taken into account in the model when calculating the variables such as current density, an overestimation of concentration of reactive species, and thus an underestimation of product species concentrations, is present during the calculations. The overestimation of reactive species during calculation is displayed in the tables below as the mass inlet error.

The operating potentials for the model were chosen as 0.815 volt for the operating conditions associated with the operation at 0.5 A/cm^2 and 0.535 volt for the operating conditions at 1.25 A/cm^2. These voltages where chosen as they correspond with the data from the initial i-v curve measurements during the experiments. With the active cell area at 16 cm^2 this means that the experiments resulted in a total current of 8 ampère at 0.815 volt and 20 ampère at 0.535 volt. At the specified potentials the setup case differs 0.14% and 0.21 %, respectively, from the experimental results with regards to the total current output.
The largest improvement in performance is found between the ideal case and the setup case. This difference in performance is 27-32%, with the ideal case outperforming the setup case. The nickel diffuser improves performance in the ideal case by 2.8-3.5%, in the setup case this slightly reduced to a 1.3-2.5% improvement.

Table 7.2: Results for the 4 cases at 750 degrees at 0.815 volt.

Case	current [A]	fuel utilisation [%]	mass inlet error [%]	improvement [%]
Setup	8.0112	39.4801	0.5741	-
Setup without diffuser	7.9012	38.9498	0.5743	-1.37
ideal	10.55	51.1069	0	31.69
Ideal without diffuser	10.1971	49.4068	0	27.29

Table 7.3: Results for the 4 cases at 700 degrees at 0.535volt.

Case	current [A]	fuel utilisation [%]	mass inlet error [%]	improvement [%]
Setup	20.0429	39.5099	0.4548	-
Setup without diffuser	19.5521	38.5623	0.4549	-2.45
ideal	26.4262	51.2055	0	31.85
Ideal without diffuser	25.7011	49.8081	0	28.23

It is important to state that the results shown in the tables above are based on a number of assumptions, mentioned in the list below.

- The streamlines do not change significantly due to phenomenons associated with SOFC operation.
- The diffusion coëfficient is constant.
- The concentration of reactants and products is uniform in the volume of a segment.
- Diffusion of species across streamlines is negligible.
- The temperature of the cell and gasses are uniform.
- The cell properties are taken from literature are representative.

It was assumed that the streamlines do not alter significantly due to phenomenons associated with SOFC operation. In chapter 5 it was shown that the streamlines from the CFD visually matched with the oxidation pattern on the cell. In this chapter, the results in Figure 7.10 show that with the areas with high fuel utilisation, above 80%, visually match with the greenest areas of Figure 5.1. As oxidation of the fuel electrode is dependent on the hydrogen concentration, the result concurs with the markings seen on the fuel electrode. This means that the assumption still can not be rejected based on the model results and visual comparison.
The assumptions that the concentration is uniform in the volume of a segment and that diffusion is constant, effects the results more in the areas where the fuel utilisation is higher. Because diffusion is dependent on the gradient of a concentration, means that the diffusion decreases as fuel becomes more dilute. This means that an assumed constant diffusion actively forces species to the fuel electrode, increasing performance. The reverse can be true if a segment has a high fuel concentration, where the assumed diffusion can limit the species transport. However, as the setup case has a significantly large area with very high fuel utilisation, compared to the ideal case, the assumption effects the setup case more.
The assumption that diffusion of species across streamlines is negligible has less effect on the ideal case, as the concentration differences on either side of a segment are relatively low. For the setup case this assumption has a larger effect as the concentration differences over streamlines can become relatively big, as seen near the outlets.

The fact that, despite the assumptions listed above, the model results are within 0.25% of the experimentally validated values for 2 operational conditions and visually match with the post mortem investigations, does not mean the effect of the assumptions is negligible. The results of the model should be taken as indications.

7.3 Summary of results

Figure 7.1 shows the results of a representative experiment performed in the original test station configuration. The i-v curve measurement taken before constant current operation and the performance during the first cycle after constant current operation indicated that there was a high performance degradation. Investigation pinpointed the water condensation in the inlet duct during electrolysis to be the root cause of high degradation encountered. This led to a redesign of the water injection system.
Experiments conducted in the test station configuration with the redesigned water injection system are shown in Figures 7.2 and 7.3. The i-v curves in Figures 7.2D and 7.3D, show a significantly reduced degradation during constant current operation, due to the optimised water injection system. This optimisation of the test station enabled the last experiment performed in this work to operate for 30 cycles within Balance protocol specification, whereas the experiments done with the original test station configuration could not perform a full cycle within those same specifications.
With the optimised water injection system, the test station enables solid oxide cell experiments to determine all experimental objectives, as specified in Section 3.1. Because the degradation due to cyclic operation can now be determined as seen in Figures 7.4 and 7.5, and the initial performance and degradation over time are displayed with the i-v curve measurements in Figures 7.2 and 7.3.
With the increased experimental duration came a increase in experimental reliability as well. The results of experiments performed in the original test station configuration could not be compared, as the current differed between the experiments and even per cycle in a single experiment. With the reduced degradation due to the new water injection system, experiments performed in the new configuration test station could be compared, as seen in Figure 7.7.

The results from the fuel flow distribution model, displayed in Table 7.2 and 7.3, show a clear cell performance improvement if the flow distribution is changed from the test station case to the flow distribution derived from literature. This confirms that the hypothesis, stating that the flow distribution of the test station has a significant influence on the experimental results of cell performance testing, is plausible. Because of these results from the model, a new flow distribution plate is designed for the test station in Chapter 6. This design provides the cell with a fuel flow flow distribution that is significantly closer to that found in the literature review, as shown in Figure 6.4. This improved flow distribution will therefore provide a cell performance improvement. More importantly the influence of the test station on the experimental results will be significantly reduced, meaning the cell performance measurements with the test station become more reliable.
Furthermore, the model shows that a significant area of the cell operates with a fuel utilisation that is associated with fuel starvation in the test station case. These effects influence the chemical stability of the fuel electrode by introducing a reduction-oxidation cycle, as explained in Chapter 5. This risk on fuel starvation effects is minimised by switching to a flow distribution as seen in the ideal case, as the maximum fuel utilisation decreases significantly. As the proposed flow distribution

plate provides the cell with a fuel flow flow distribution close to that of the ideal flow distribution, switching to this design of flow distribution will minimise the risk on the effects of fuel starvation.

Chapter 8

Conclusions and recommendations

The goal of this thesis was to develop the test station used for reversible solid oxide cell testing for the Balance project. The development was to lead to better and more reliable results from the experiments performed with the test station to achieve the experimental objectives set out by the Balance project.

Investigation into experiments performed in the original test station configuration started as the experiments showed a high degradation rate and the fact that post mortem investigation found that all cells had cracked during the experiment. With the data seen in Figure 3.9, the calculations done in Chapter 4 and the results of experiments numbers 7 and 9 it was shown that water condensation in the water injection system caused the high degradation rate and the breaking of the cells. As the original water injection system was influencing the experimental results and preventing the experiments to achieve the objectives stated in Section 3.1, the water injection system was redesigned in Chapter 4.

The implementation of the redesigned liquid water injection system led to the reduction of the voltage fluctuations during electrolysis operation from 5 millivolt to 1.5 millivolt, which is a reduction of 70%, as seen in Figure 4.3. The spikes of 20 millivolt, seen in Figure 3.9, with the original injection system disappeared as well when using the redesigned system. As these spikes are assumed to be only present when condensation in the inlet duct occurs, the absence of them indicate that the condensation problem is solved by using the redesigned water injection system. As a result of the improved water vapour supply, the solid oxide cells are now retrieved from the setup in one piece after experiments, the time dependence of the i-v curve measurements during electrolysis has been minimised and thus the reproducibility of the i-v curve measurement has been increased.
The new liquid water injection system also provides a significant upgrade in long term cell performance measurements. The baseline experiments which were performed with the original system, have achieved a maximum of 0.5A/cm^2 and a total of 3 cycles with an operating temperature of 750 degrees Celsius across 6 experiments. This means that the third and final experiment that used the optimised liquid water injection system not only operated at 350% the

average current density, calculated with the average current density over all cycles, it completed more than 900% more cycles with a 50 degree lower operating temperature. It has to be noted that the increase in longevity is in part due to the fact that the baseline experiments were performed with generation 1 cells and the last experiment with a generation 2 cell. The generation 2 cells should have less degradation over time compared to the generation one cells, as mentioned before, however to which extend is unclear. From personal correspondence with Balance project partners it became clear that they did not experience an increase in long term performance in the same magnitude, it is unlikely that the increase in performance and longevity seen between the experiments is solely due to the generational improvement of the cells used.
The extended experimental duration enabled the measurement of the degradation of performance during constant current operation and due to cyclic operation. It was found that the degradation is 5 and 7 times higher during cyclic operation, for fuel cell and electrolysis mode respectively. This result means that the degradation due to cyclic operation is significant. If the technology is to be used on a national level for electrical grid balancing applications, more research is needed. The degradation rate of the ReSOC measured was relatively high compared to the results from Balance partners. This finding means that part of the improvement can be found by further optimising the test station to improve long term ReSOC performance.
The optimisation of the water injection system has been an important step in the development of the test station, as this development enabled the test station to perform the experiments and measurements necessary to meet the objectives set for the experiments by the Balance protocol, as displayed in Section 3.1. Furthermore, it improved the reliability of the cell performance measurements as the influence of the test station on the short term and long term cell performance measurements is significantly reduced. Lastly the development improved the reliability of the test station, meaning that experiments can be duplicated and verified which showed that more research and development is necessary for both the ReSOC and the test station.

When investigating the breakage of the cell, markings were found on the fuel electrode. A 2D CFD study confirmed that it is plausible that the markings indicate the flow distribution inside the test station. It was hypothesised from these findings that the fuel flow distribution significantly impacts the cell performance and thus the measurements done in the test station.
A simple SOFC model was used to convert the CFD data to current density and fuel utilisation data. The results from this model show an approximate increase of 30% of total current output at the same potential for an case with a more ideal flow distribution compared to the case with the distribution found in the test station. This value can be found in Tables 7.2 and 7.3.
This increase in performance is due to the fuel flow distribution removing the high fuel utilisation area's from the cell. Figure 7.10 shows that an area of approximately 20% operates with a fuel utilisation of higher than 80% with the original flow distribution plate, whereas the more ideal flow distribution does not exceed 60% fuel utilisation. To give context, the overall fuel utilisation in the case with the more ideal fuel flow distribution is 10 percentage points higher compared to the case with the flow distribution found in the test station. This decrease in local fuel utilisation across the cell in the more ideal case leads to a higher local reversible, Nernst, potentials, lower overpotentials and thus an increased cell performance.

When drawing conclusions from the results of the model it has to be kept in mind that the results, mentioned above, are based on a large number of assumptions. Due to these assumptions the

results need to be taken as indication.
As all experiments shown in Chapter 7 have stopped before the 33 operational cycles were completed because the prescribed upper and lower voltage limits were reached, a further extension of the experiment duration is therefore expected if a ideal flow distribution is used in the test station. With the improved flow distribution the upper and lower potential limits will be met later during the experiment due to the increased cell performance. The fact that the maximum local fuel utilisation is decreased significantly can also contribute to a longer experiment duration as the risk of fuel starvation effects on the cell is minimised. It is difficult to state to which extend the effects of fuel starvation impact fuel electrode stability, and thus long term performance. At the time of writing the impact of these effects are still unclear in literature. However, as the degradation seen during the experiments is still higher compared to the results from Balance partners, it is assumed that this effect had a significant effect on the degradation.
The fact that the model shows that adopting a more ideal flow distribution in the test station can increase cell performance significantly and reduce the risks and effects of fuel starvation, means that the current flow distribution influences the experimental results. Changing the flow distribution in the test station to a more ideal flow will therefore reduce the influence of the test station on the cell performance measurements and thus improve reliability of the measurements
The results in Chapter 6 show that the proposed flow distribution plate provides the cell with a flow distribution closer to the ideal flow distribution than the currently in the test station. It is therefore recommended that the adapter plate is produced to further improve the test station, as the implementation will increase the reliability of cell performance measurements in the test station as the influence of the fuel flow distribution is further minimised.
With the implementation of the more ideal flow plate, the simple SOFC conversion model can be validated as well. If the new flow distribution plate provides the increase in performance as predicted by the model, it proves that the fuel flow distribution model can be used as a quick tool to asses the performance differences between ReSOC test stations.

In summary, this thesis concludes that the redesign of the water injection system has solved the condensation problem in the inlet duct which caused the high degradation and cell failure observed during experiments. The minimisation of condensation has led to more reliable measurements and longer experiment duration. The longer experiment duration enabled the test station to perform the experiments needed to achieve all experimental objectives set by the Balance project.
Due to the longer experiment duration it was measured that the degradation over constant operation was approximately 5 to 7 times lower compared to the degradation due to cyclic operation. This result indicates that the impact of cyclic operation is still significant and that the ReSOC still needs further development if the technology is to be used in cyclic operation on an industrial scale. Part of the improvement needed can come from development of the test station, as the results seen from the experiments are still lagging behind compared to other Balance partners. A simple fuel flow distribution model showed that further improvement of the test station can be made when the inlet of the fuel flow distribution plate is changed from perpendicular to tangential, to the cell surface area. It is therefore recommended that in future work the proposed fuel flow distribution plate is used in the test station. The use of the new fuel flow distribution plate will not only improve cell performance, lower the influence of the test station on performance measurements and reduce fuel starvation risks, it can also validate the fuel flow distribution model. When the model is validated, it offers experimental researchers a quick tool to compare flow distribution plates.

The main conclusions mentioned in this chapter are listed below.

- Degradation of cell performance is seen in constant current and in cyclic operation.
- Degradation is higher in cyclic operation compared to constant current operation.
- Cell performance increased and degradation reduced due to the redesigned water injection system.
- With the redesigned water injection system the experimental duration was verified up to 1000 hours and all test objectives can be achieved.
- Degradation measured in the test station of the TuD still lags behind compared to other Balance partners, except during constant current electrolysis operation, where the performance and the degradation rate is similar compared to other Balance partners.
- Performance degradation needs to be decreased further for economic viability.
- Test station can be further optimised to increase cell performance and reduce degradation.

"**Science knows it doesn’t know everything, otherwise it would have stopped.**"
- Dara O’Briain

Appendices

Appendix A

CFD results

In this appendix the remaining results of the CFD analysis are discussed. For each of the remaining cases the residuals, the flow velocity field and the streamlines are shown below.

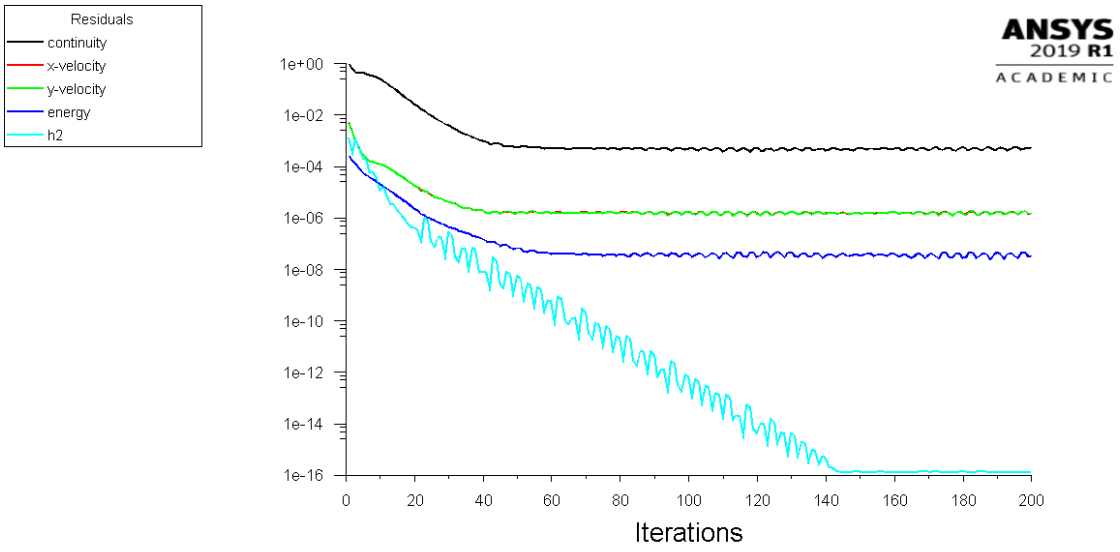

Figure A.1: Residual plot of the CFD for the setup case without nickel foam diffuser.

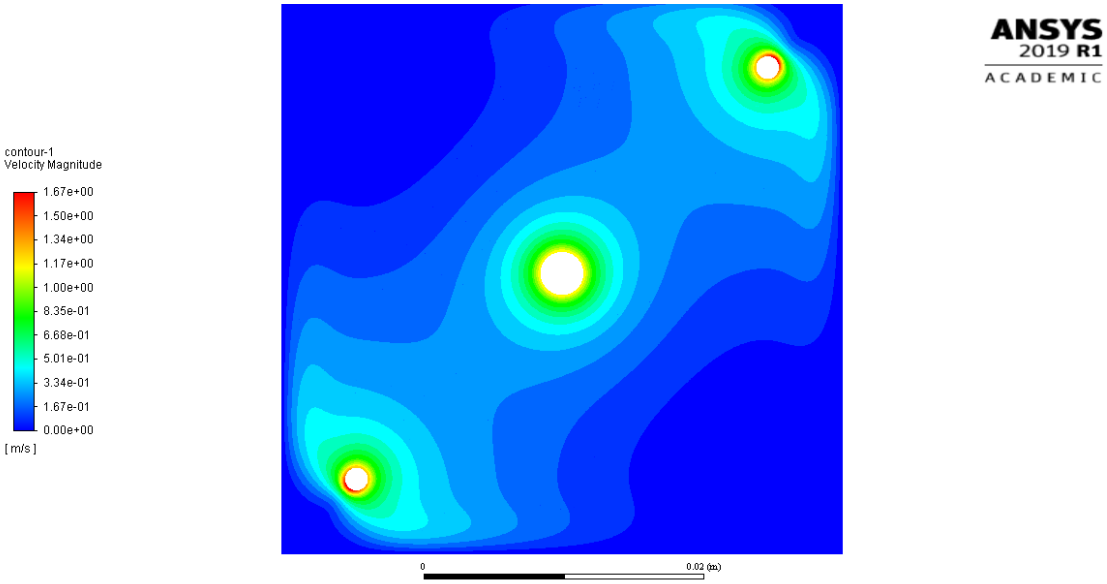

Figure A.2: Residual plot of the CFD for the setup case without nickel foam diffuser.

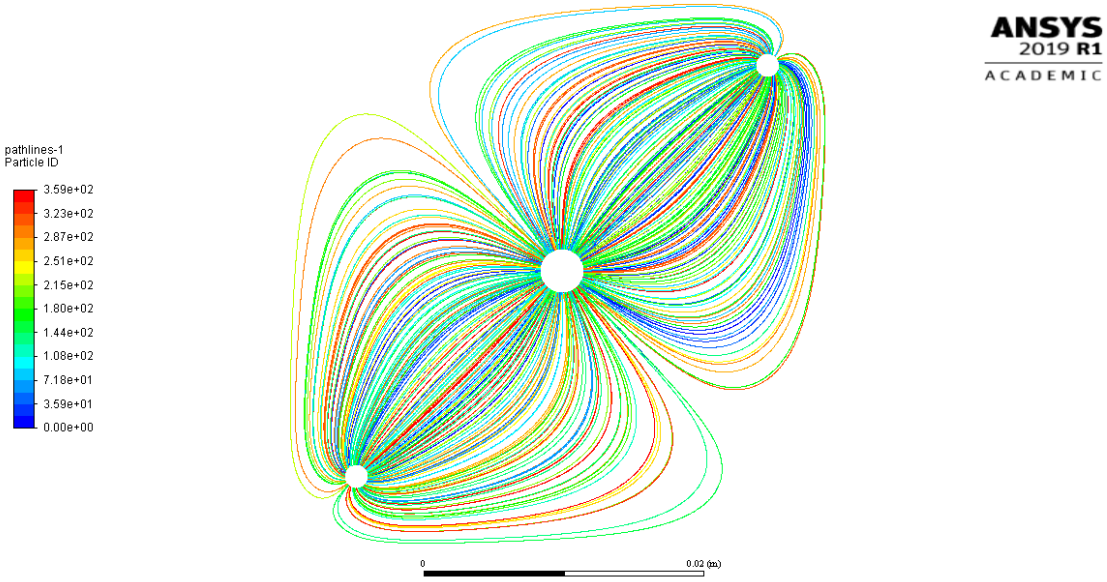

Figure A.3: Residual plot of the CFD for the setup case without nickel foam diffuser.

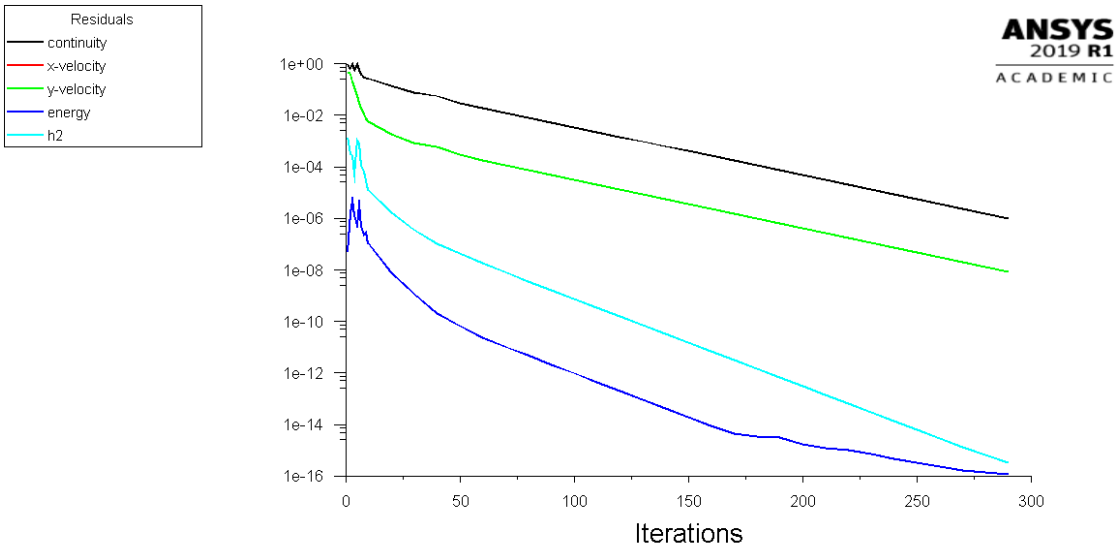

Figure A.4: Residual plot of the CFD for the setup case with nickel diffuser.

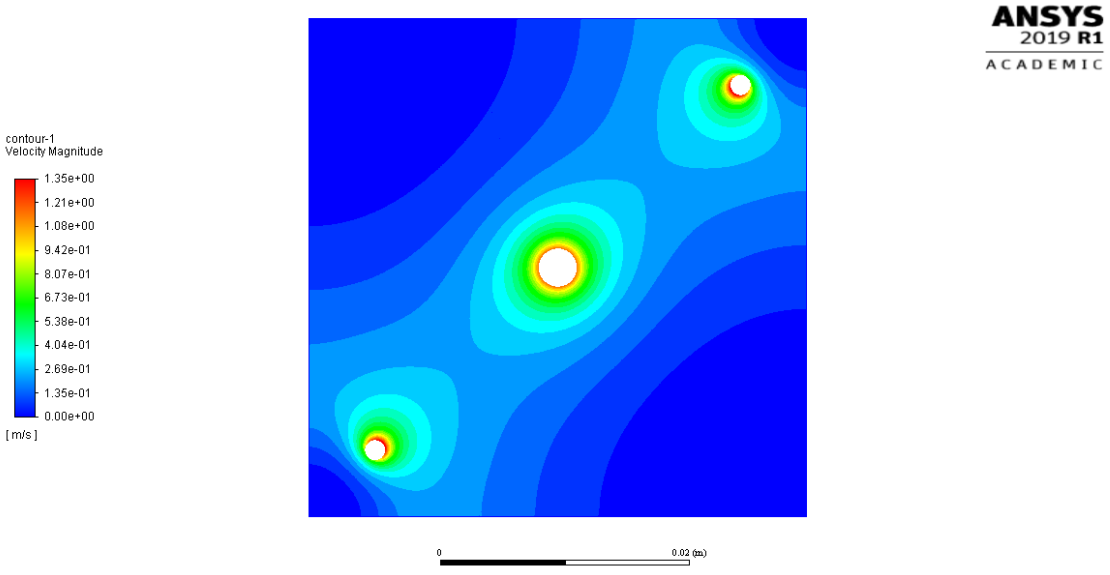

Figure A.5: Residual plot of the CFD for the setup case with nickel diffuser.

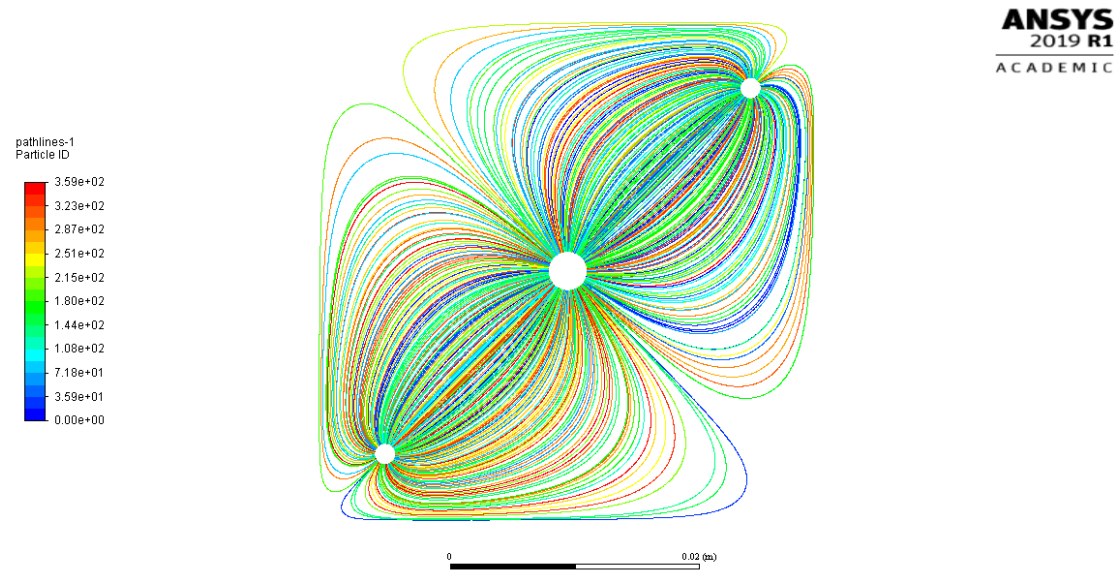

Figure A.6: Residual plot of the CFD for the setup case with nickel diffuser.

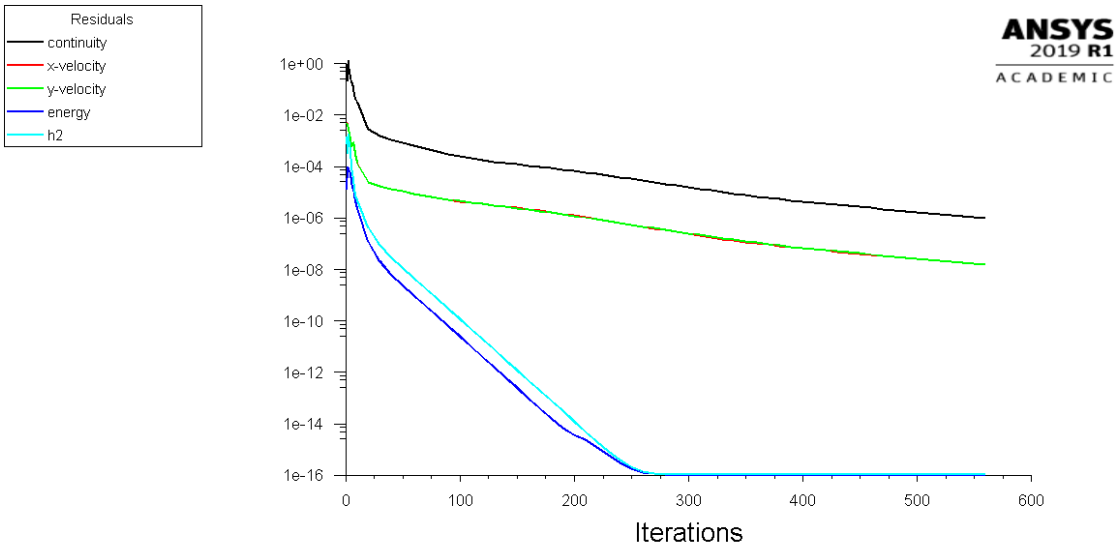

Figure A.7: Residual plot of the CFD for the setup case with higher inlet flows and without nickel foam diffuser.

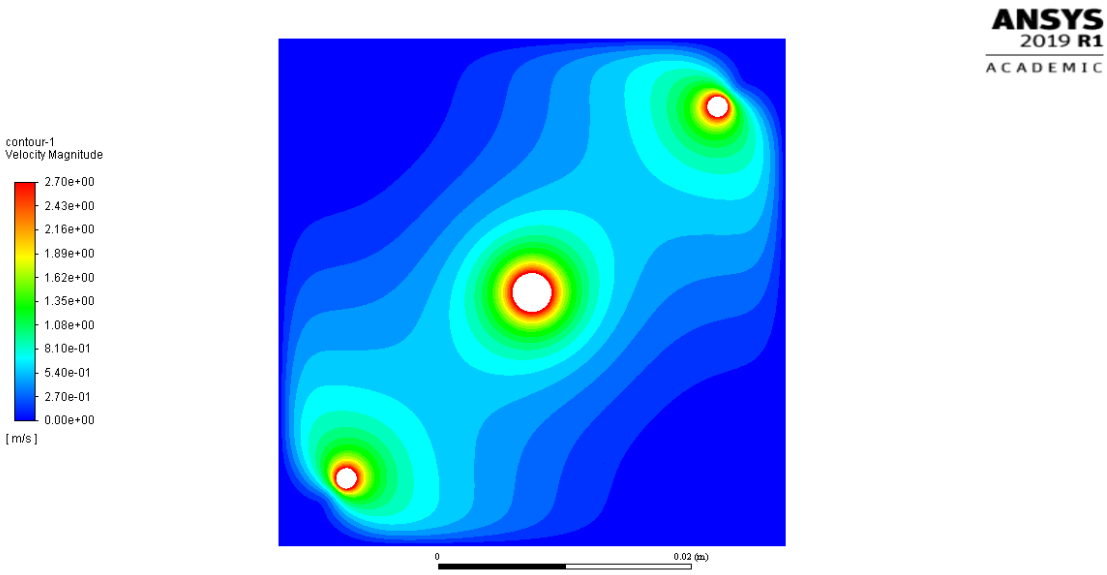

Figure A.8: Residual plot of the CFD for the setup case with higher inlet flows and without nickel foam diffuser.

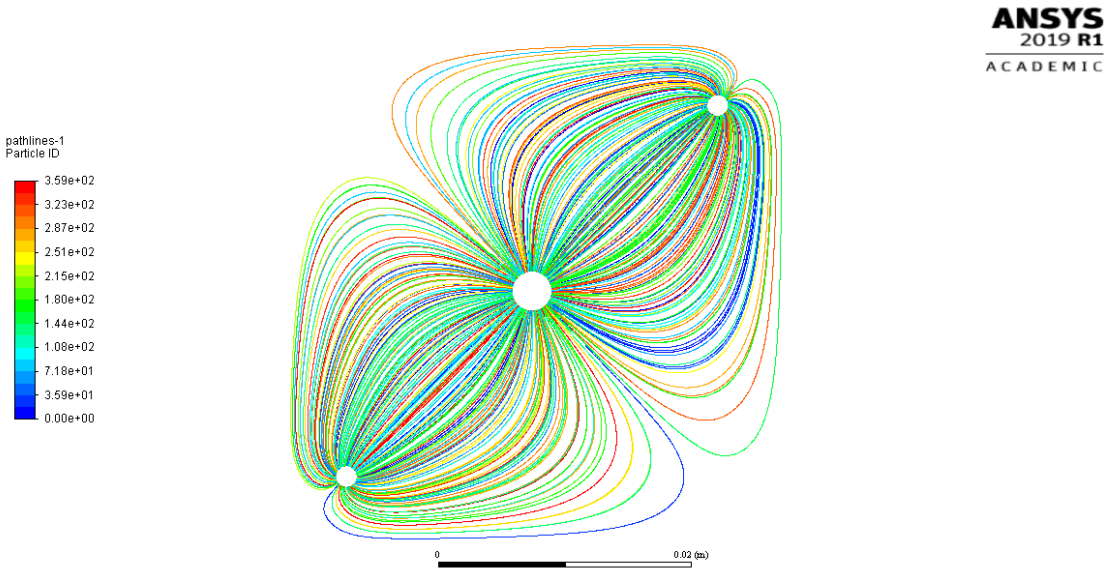

Figure A.9: Residual plot of the CFD for the setup case with higher inlet flows and without nickel foam diffuser.

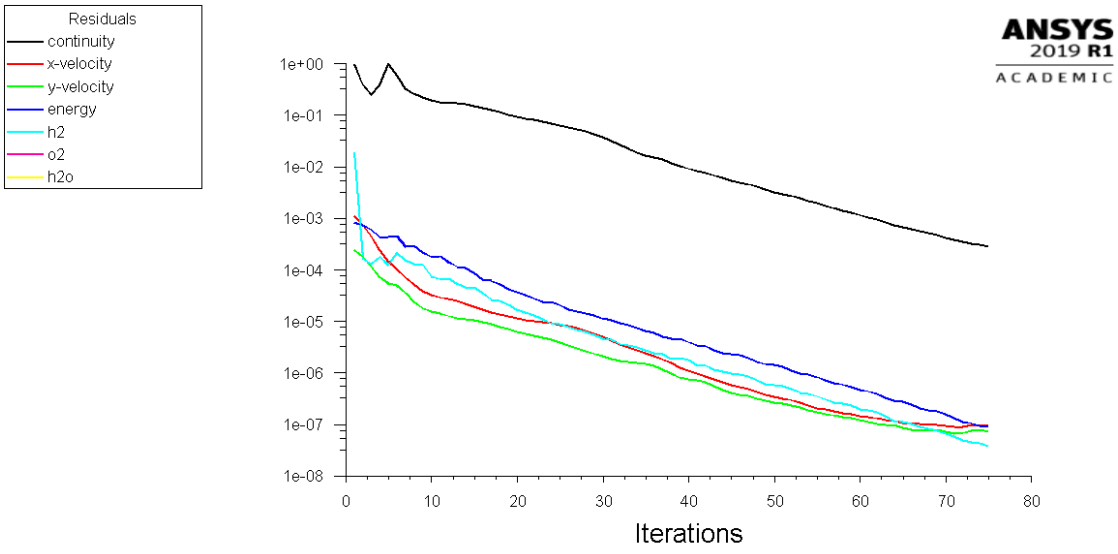

Figure A.10: Residual plot of the CFD for the ideal case without nickel foam diffuser.

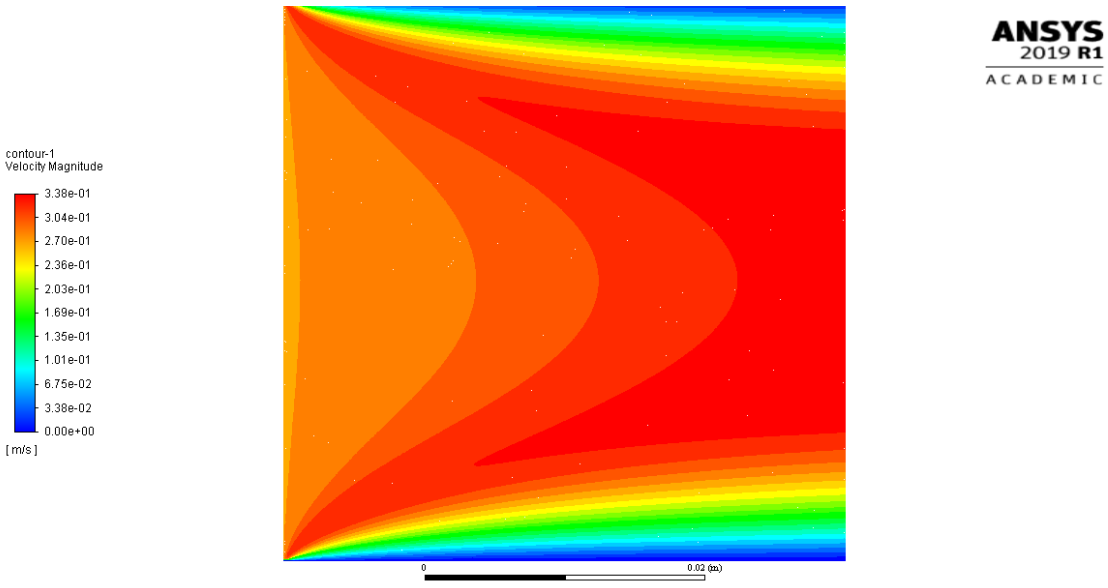

Figure A.11: Residual plot of the CFD for the ideal case without nickel foam diffuser.

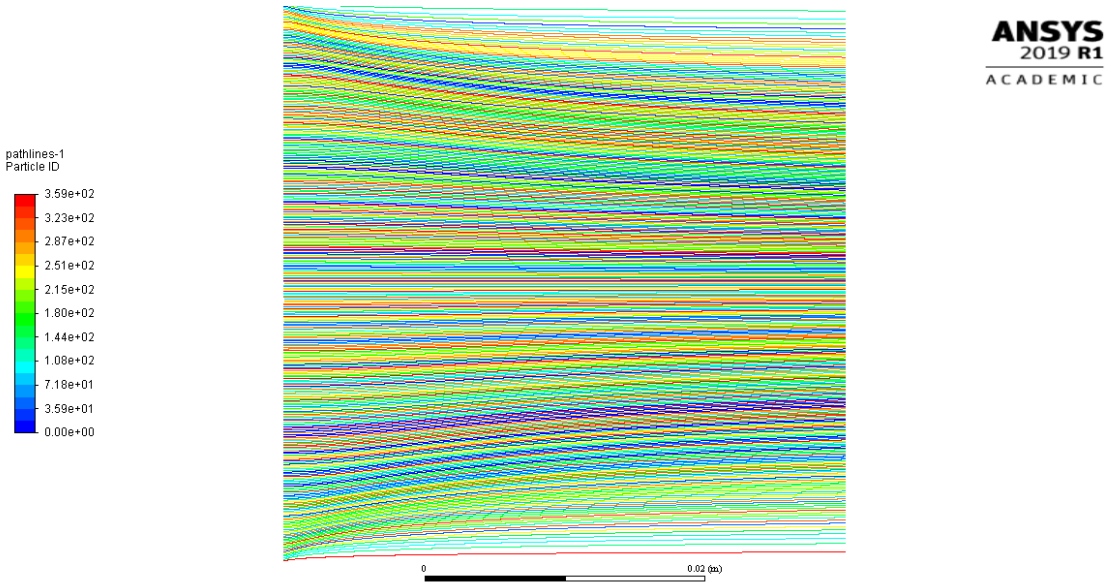

Figure A.12: Residual plot of the CFD for the ideal case without nickel foam diffuser.

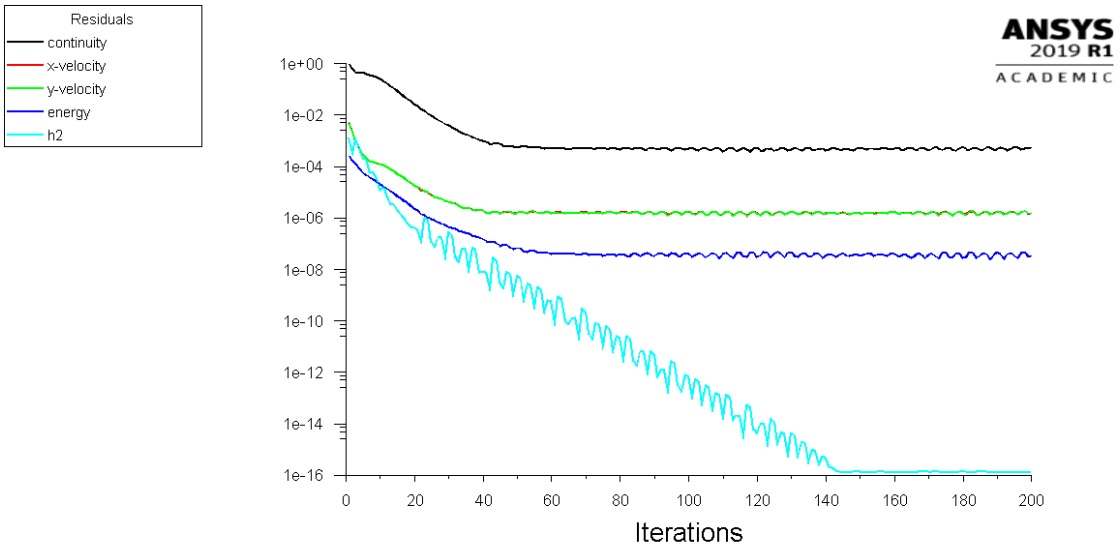

Figure A.13: Residual plot of the CFD for the ideal case with nickel diffuser.

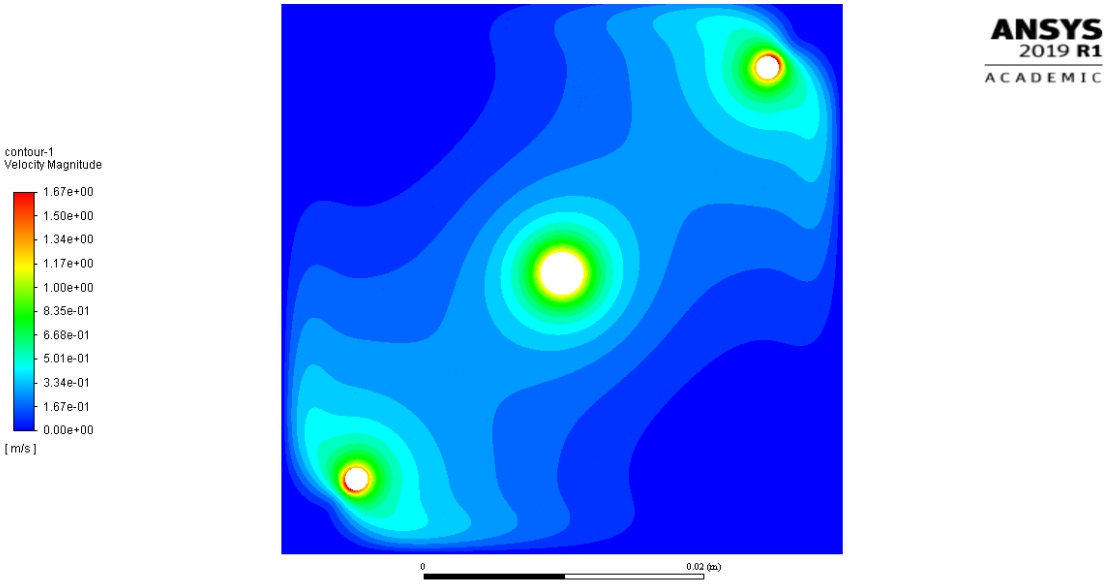

Figure A.14: Residual plot of the CFD for the ideal case with nickel diffuser.

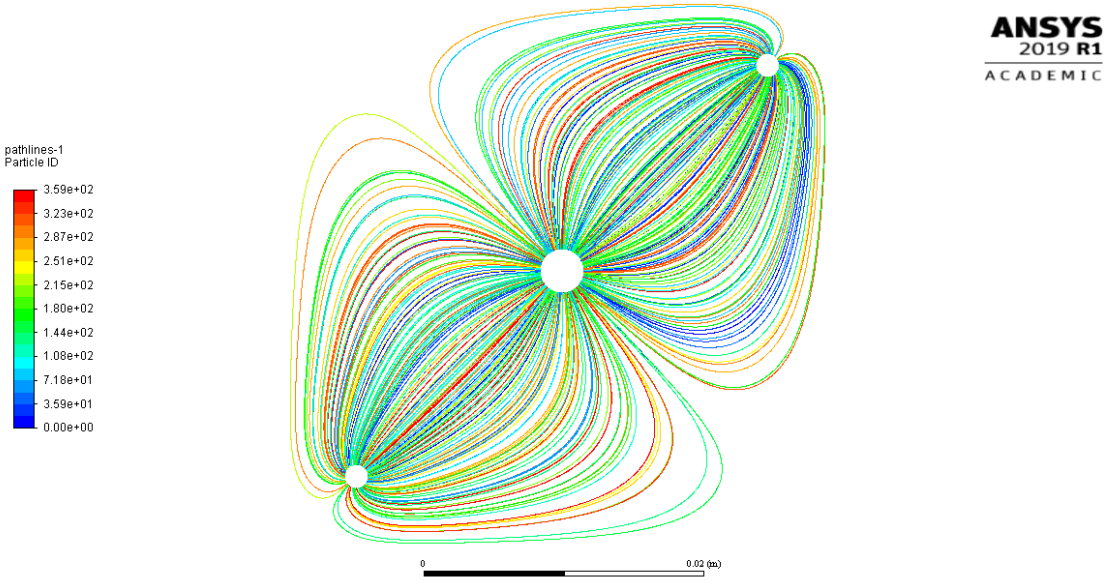

Figure A.15: Residual plot of the CFD for the ideal case with nickel diffuser.

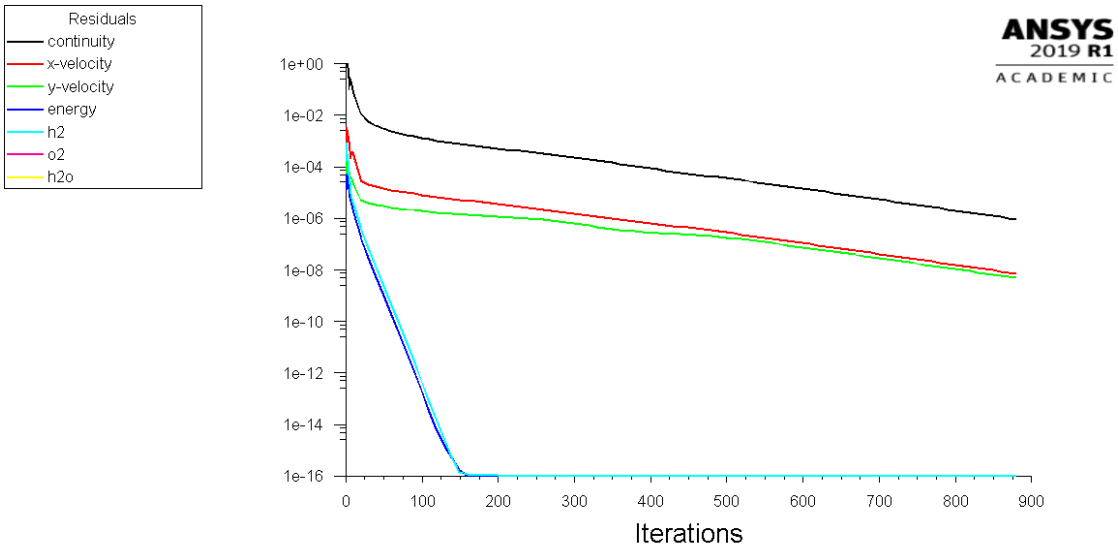

Figure A.16: Residual plot of the CFD for the ideal case with higher inlet flows and without nickel foam diffuser.

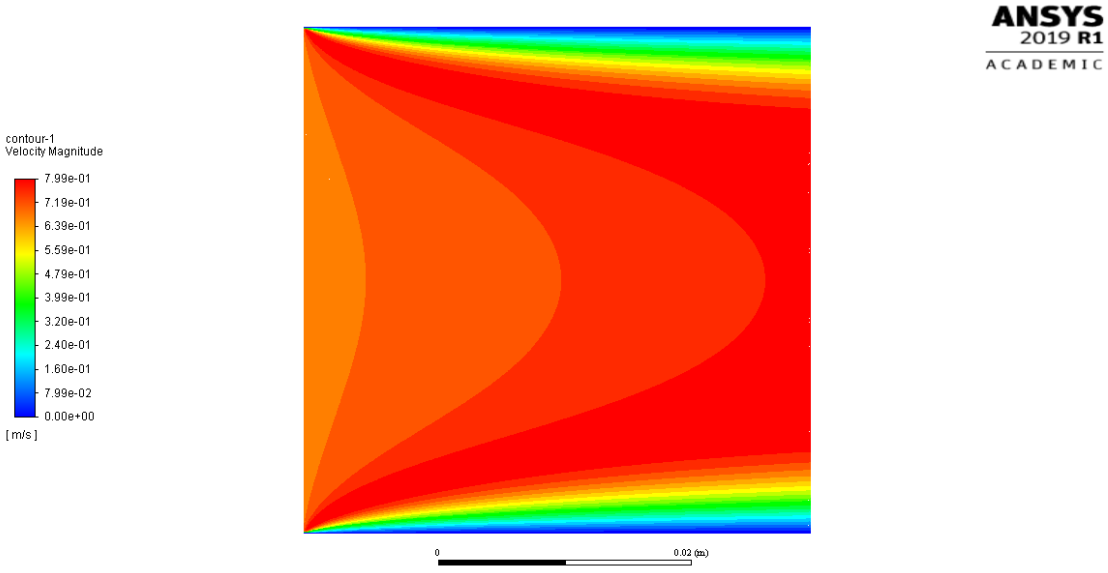

Figure A.17: Residual plot of the CFD for the ideal case with higher inlet flows and without nickel foam diffuser.

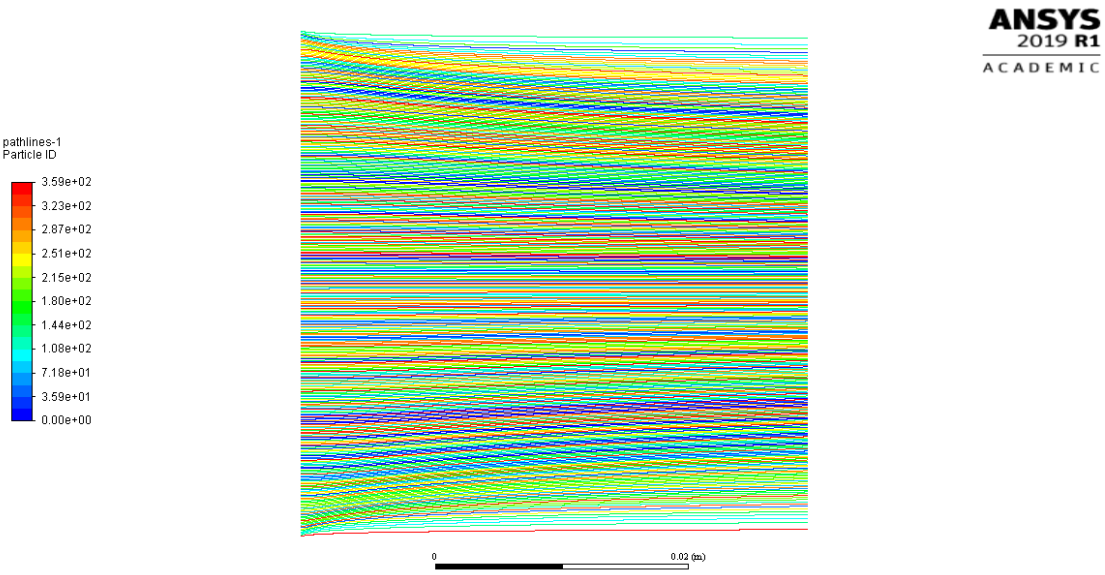

Figure A.18: Residual plot of the CFD for the ideal case with higher inlet flows and without nickel foam diffuser.

Appendix B

Results of experiments

In this appendix the results of experiments 7,8 and 10 are displayed. These results were omitted from the report as they were conducted with a different objective or the data was effected by an unexpected event.
In Figure B.1 the result of experiment number 7 is displayed. This experiment was performed with a 3 meter long preheated inlet duct without cartridge to verify calculations done in Chapter 4.
The experiment was conducted at a current density of 0.5 A/cm^2, which gives a total current of 8 ampère as seen in Figure B.1.A. As this experiment was performed to gather data on the fluctuations during electrolysis, the fuel cell voltage was kept above 0.6 volt to prevent any issues during fuel cell limiting the experimental duration. The average operational potential during fuel cell operation is shown B.1.B. During cycle 7 the voltage decreased to 0.6 volt at a current of 7.7 ampère, the current was not increased further. For cycles 8,9 and 10 the current output was reduced even further to keep the voltage equal or above 0.6 volt.
In Figure B.1.C the operational voltage is shown during electrolysis. The first 6 cycles the voltages was allowed to increase as the current was kept steady at 8 ampère. During these cycles the voltage climbed 200 millivolt, which is 34 millivolt per cycle. This decrease in performance is roughly 4 times higher than what is seen in experiment number 12. Therefore, in order to exend the experiment the current was limited to 6 ampère in cycles 7 and 8 to elongate the experiment, as degradation is dependent on the current density. To verify if this actually worked, the experiment was put back to 8 ampère in cycle 9. As the operational voltage increased to over 1.6 volt, an increase of more than 200 millivolt per cycle, the reduction of current did not reduce the degradation of performance. Finally in cycle 10 the current was reduced to 4.5 ampère, which marked the end of the experiment.
In Figure B.1 the i-v cuve graph shows the inital i-v curve measurement. Due to heavy fluctuations, as displayed in Figure 4.3, some i-v curve measurement points during electrolysis could not be measured.

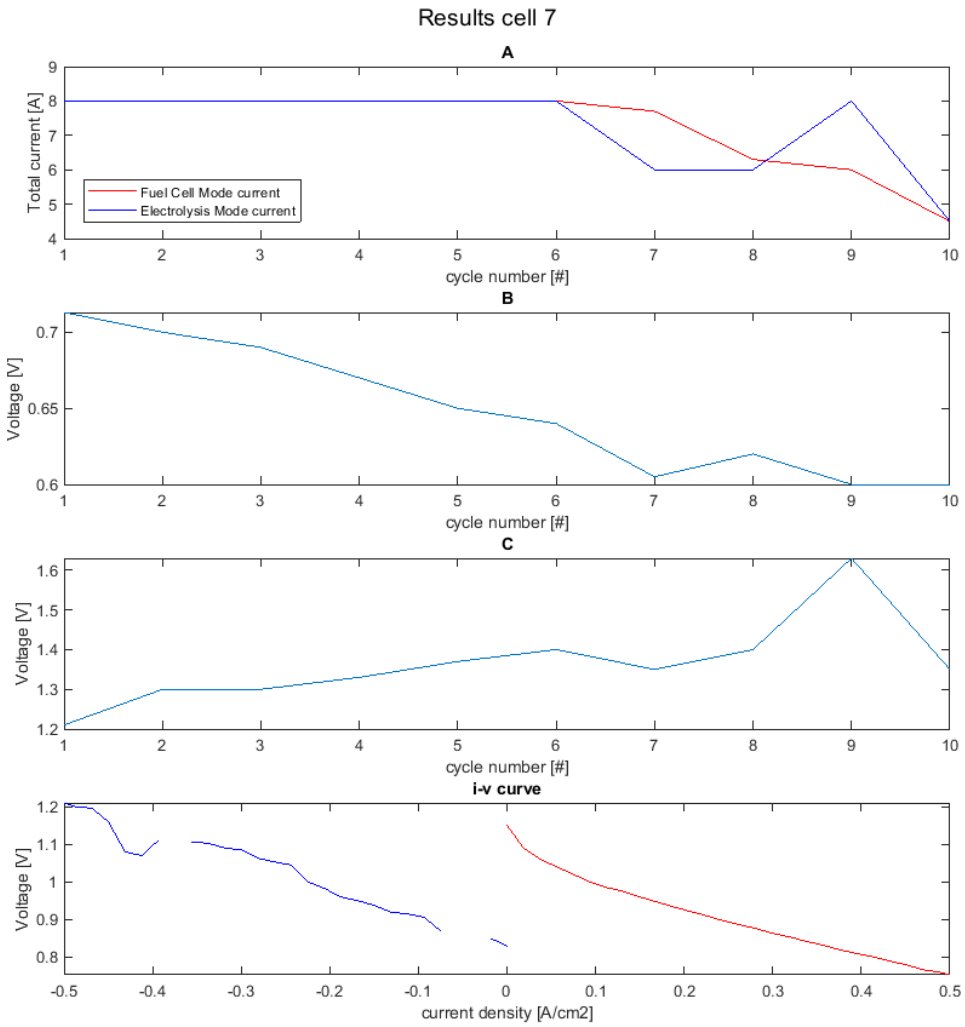

Figure B.1: Results from experiment number 7.

Experiment number 8 collected no data due to a failure during the start up procedure, where a fuel exhaust duct got clogged. This blockage caused a fuel back pressure, which reduced the cell performance to a unusable level.

Experiment number 9 was conducted to verify the calculations in Chapter 4, like experiment number 7. The fuel cell operation was operated at 7 ampère, shown in Figure B.2.A, as the initial operational voltage was already under 0.6 volt. Like in experiment number 7, the operational

voltage of the fuel cell operation was kept relatively high compared to the specified minimum of 0.4 volt, as to prevent the occurance of experiment ending events during this operation. In Figure B.2.B the operational voltage during fuel cell operation is seen.
Electrolysis operation was performed at 8 ampère in the first 2 cycles. However during these two cycles the operational voltage increased more than 50 millivolt per cycle, as seen in Figure B.2.C. In an effort to curb the degradation rate the current was lowered to 7 ampère. This reduction in current draw allowed the cell to operate for 21 cycles.
In the last graph, the i-v curve measurement results from before the cyclic operation and after cyclic operation are displayed. The difference between the two curves indicate the performance loss over 21 cycles is significant.

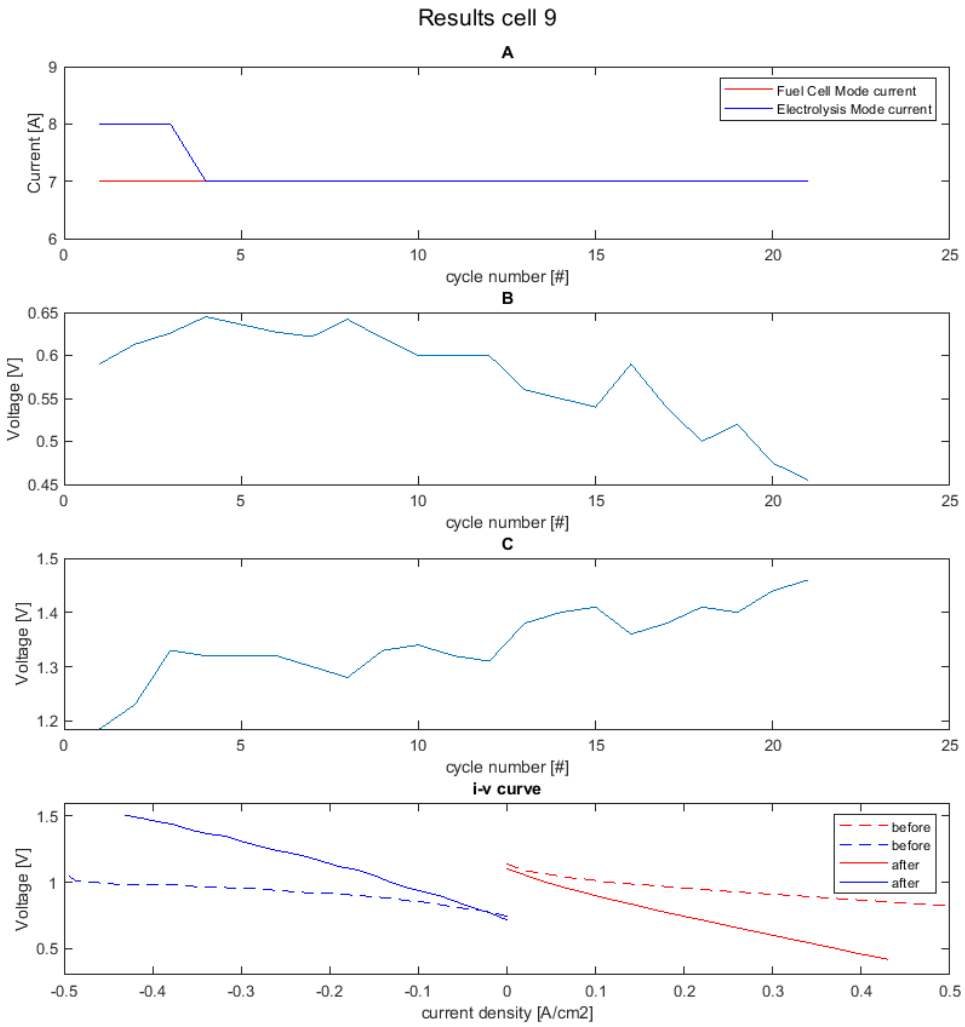

Figure B.2: Results from experiment number 9.

The results of experiment number 10 are shown in Figure B.3, where B.3.A indicated total system current, B.3.B fuel cell operational voltage, B.3.C the operational electrolysis voltage and the last graph shows the i-v curve measurements. This was the first experiment conducted with the objective to operate at 1.25 $A.cm^2$, instead of 0.5, and the first experiment with the redesigned water injection system.
The first setback that was encountered during this experiment, occurred during the fuel cell operation in the first cycle. During this operation the platinum wires coming from the cell to

transport the current to the electrical subsystem started to glow white hot. Because of this setback, all operation was limited to 12 ampère. This is therefore the current seen in cycles 2 to 6 for fuel cell operation and 1 to 6 for electrolysis operation. This setback was solved for experiment number 11 by adding more platinum wires to the current collector.
During fuel cell operation in cycle 7, an outside event triggered a gas alarm. This gas alarm cut off all flows to the setup. This caused high degradation in the cell as seen by the significant decrease in operational voltage in cycle 7 during fuel cell mode and the significant increase in electrolysis in cycle 8. After this event the current in both modes was reduced to keep the operational voltage of fuel cell mode above 0.5 volt and for electrolysis mode below 1.5. Because of the relatively low performance after the event, the experiment was stopped after 14 cycles, as it was more beneficial for the Balance project to start a new experiment.
In the last graph the i-v curve measurements taken before steady state operation and before cyclic operation are shown. From these measurements it is demonstrated that the high degradation over the steady state operation is relatively low with the redesigned water injection system, which is also concluded from the i-v curves shown in Figures 7.2 and 7.3.

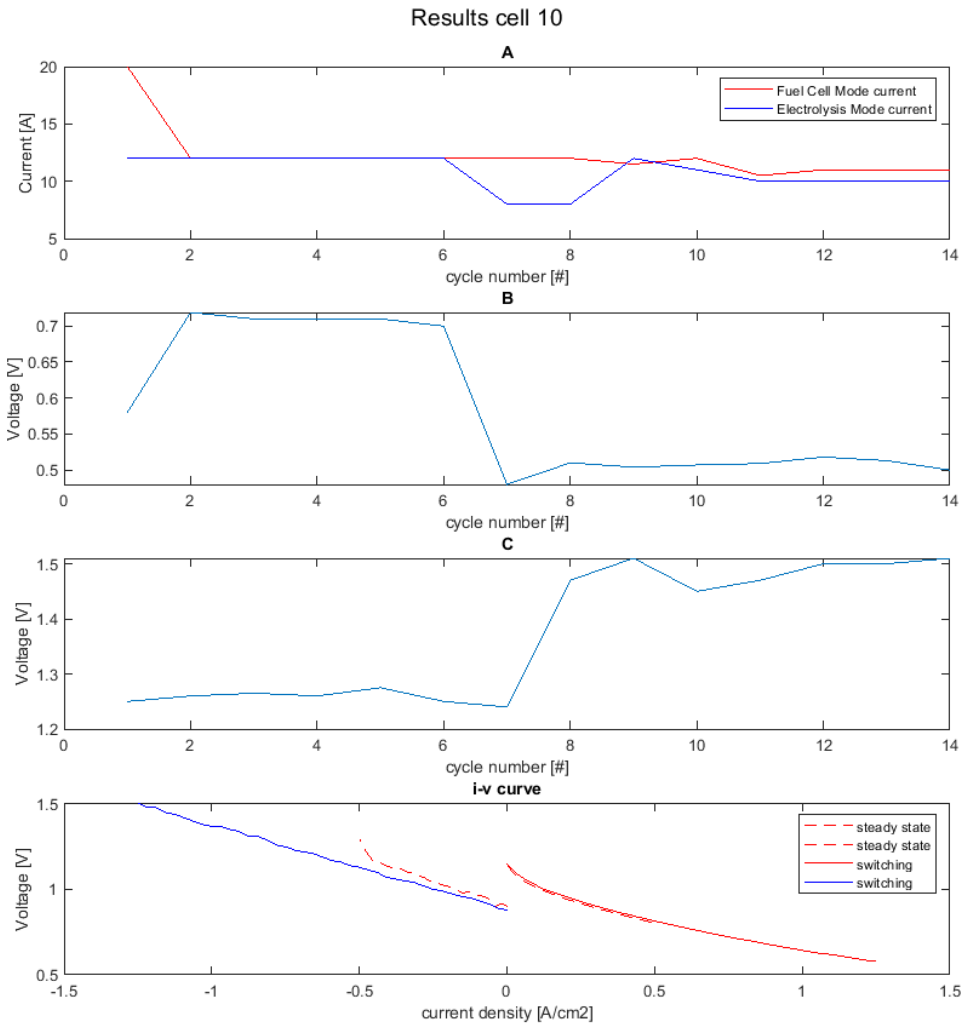

Figure B.3: Results from experiment number 10.

Appendix C

Results of the fuel flow distribution model

In this section of the report the results from the model for the cases not discussed in the report are displayed. These results were omitted from the report to improve readability as they show the same trend mentioned in the report. The ideal case has a more uniform flow compared to the setup case and the nickel foam diffuser has a slightly bigger impact on performance in the ideal case. This larger impact is due to the more pronounced boundary layer development in the ideal case.

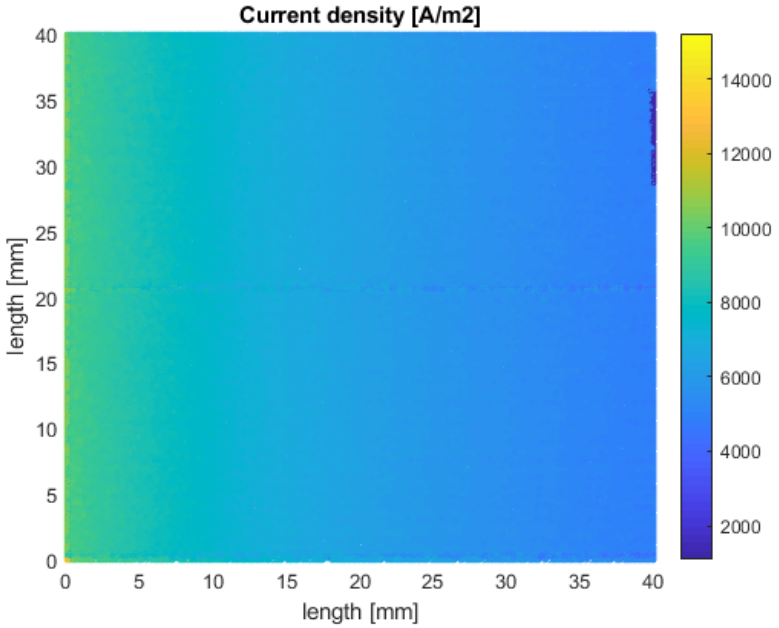

Figure C.1: Current density of the ideal case.

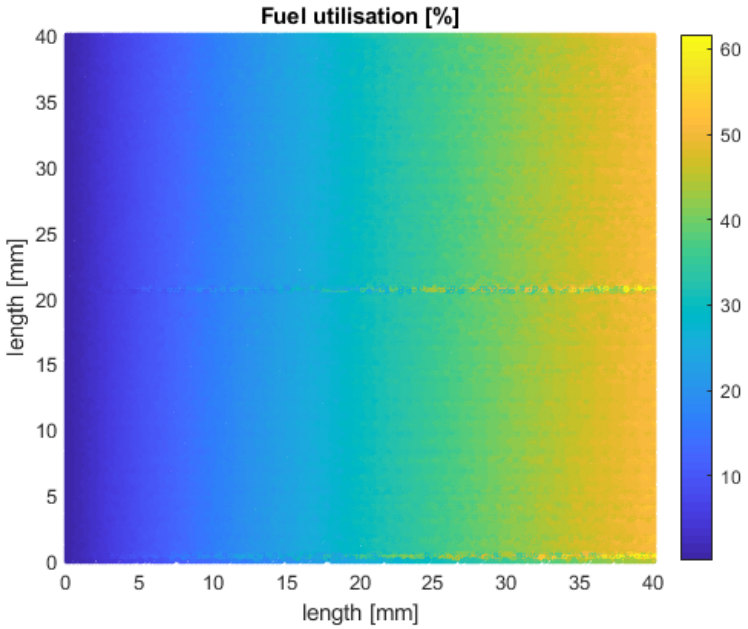

Figure C.2: Fuel utilisation of the ideal case.

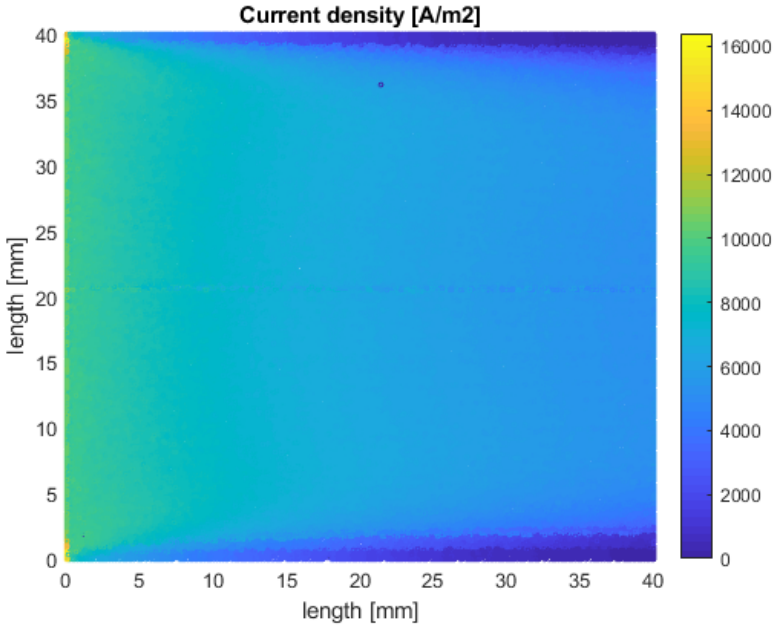

Figure C.3: Current density of the ideal case without nickel foam diffuser.

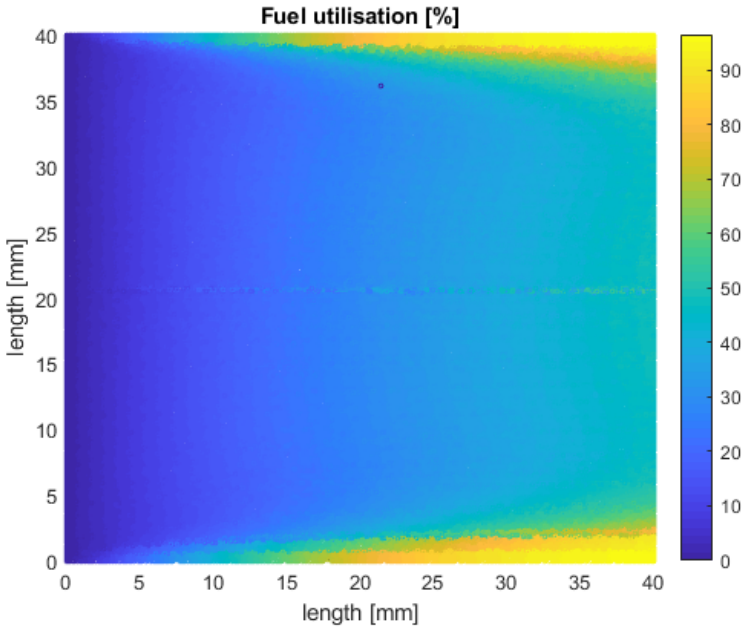

Figure C.4: Fuel utilisation of the ideal case without nickel foam diffuser.

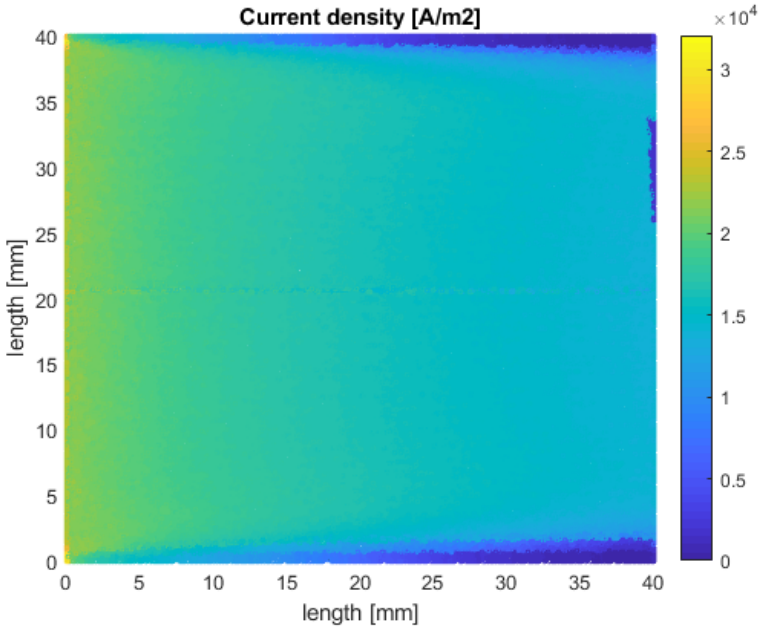

Figure C.5: Current density of the ideal case with higher flows and without nickel foam diffuser.

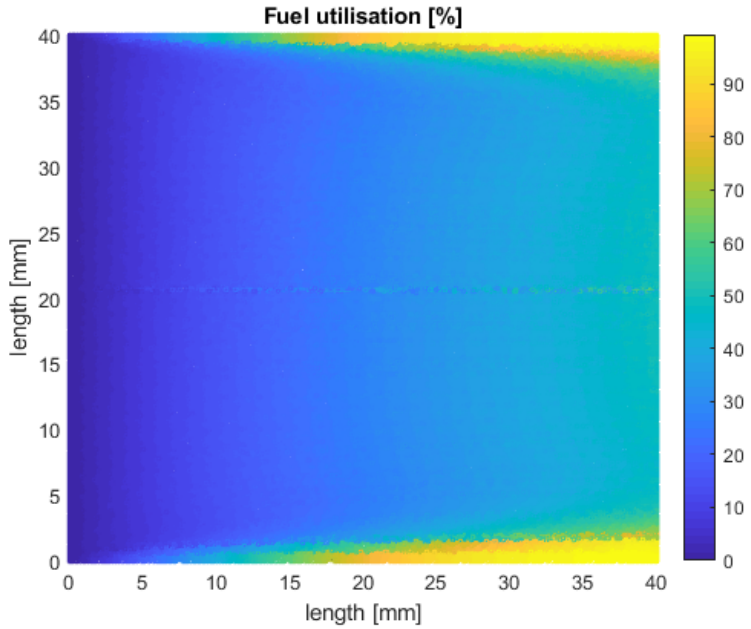

Figure C.6: Fuel utilisation of the ideal case with higher flows and without nickel foam diffuser.

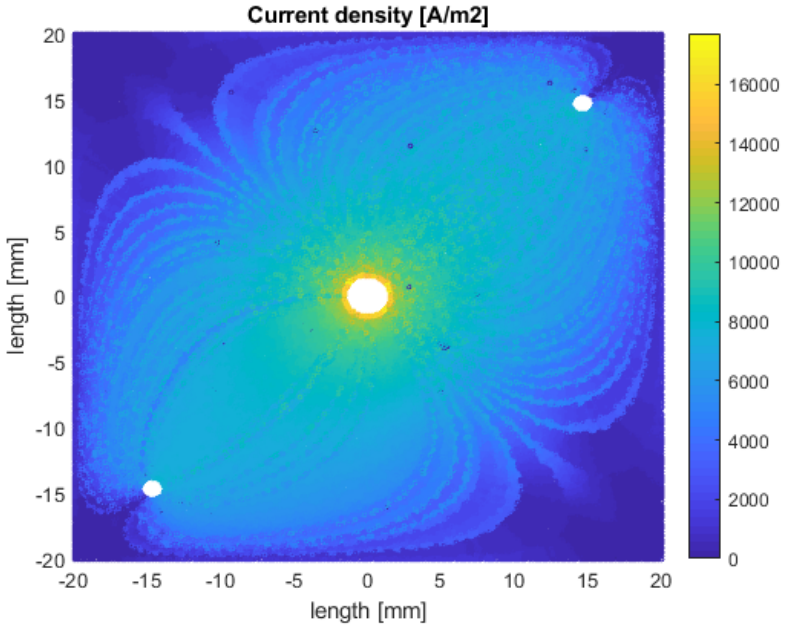

Figure C.7: Current density of the setup case.

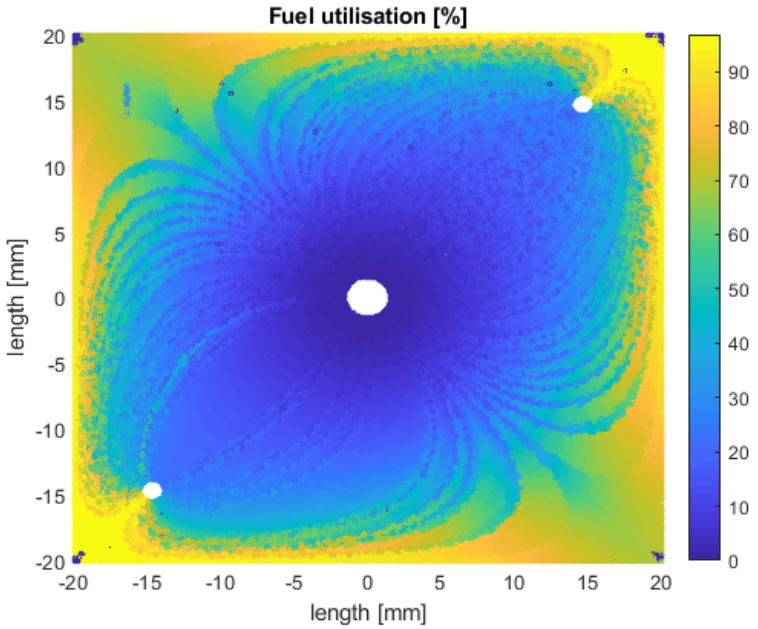

Figure C.8: Fuel utilisation of the setup case.

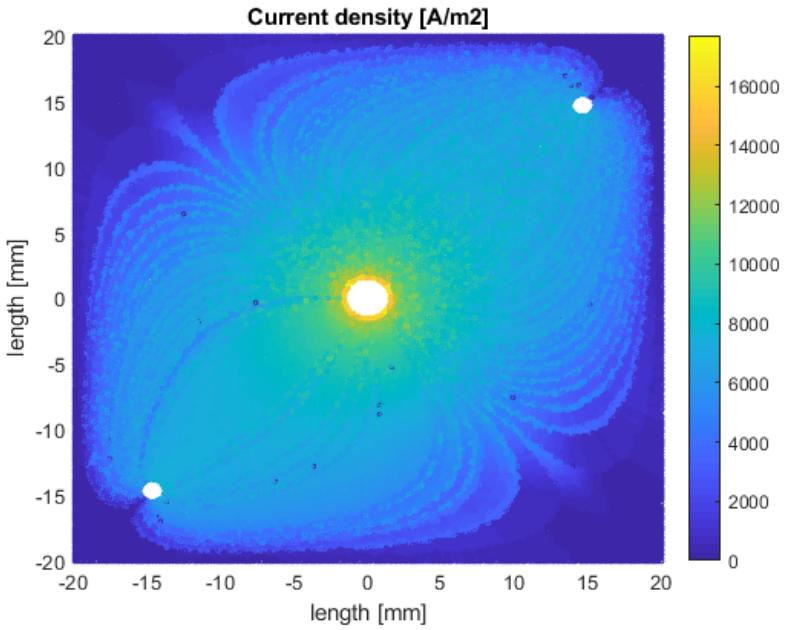

Figure C.9: Current density of the setup case without nickel foam diffuser.

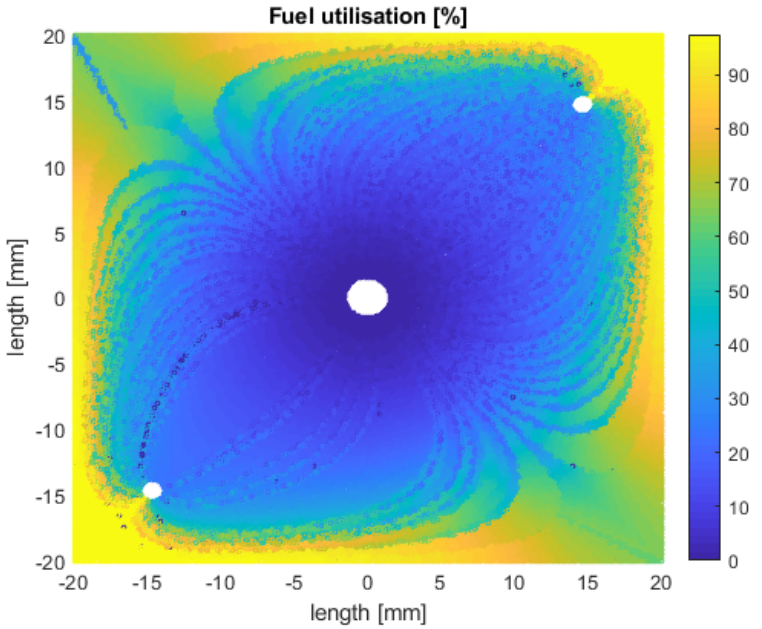

Figure C.10: Fuel utilisation of the setup case without nickel foam diffuser.

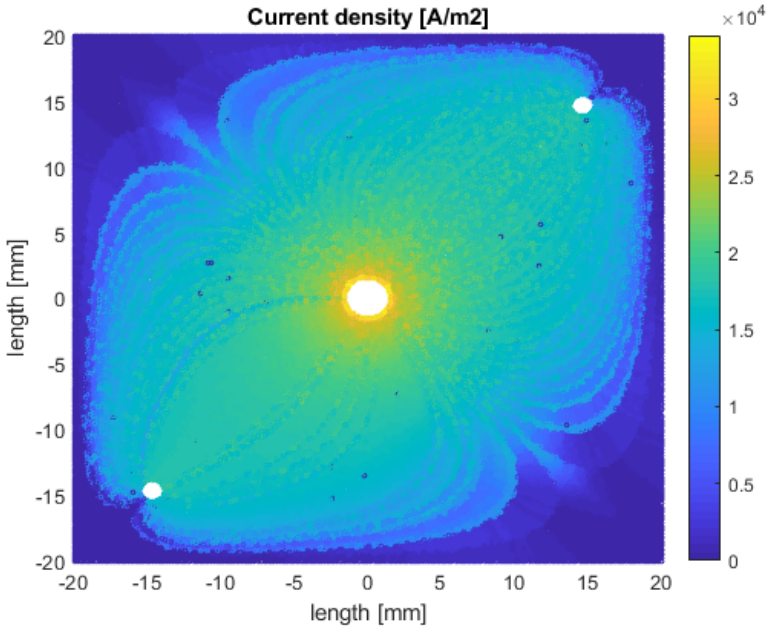

Figure C.11: Current density of the setup case with higher flows and without nickel foam diffuser.

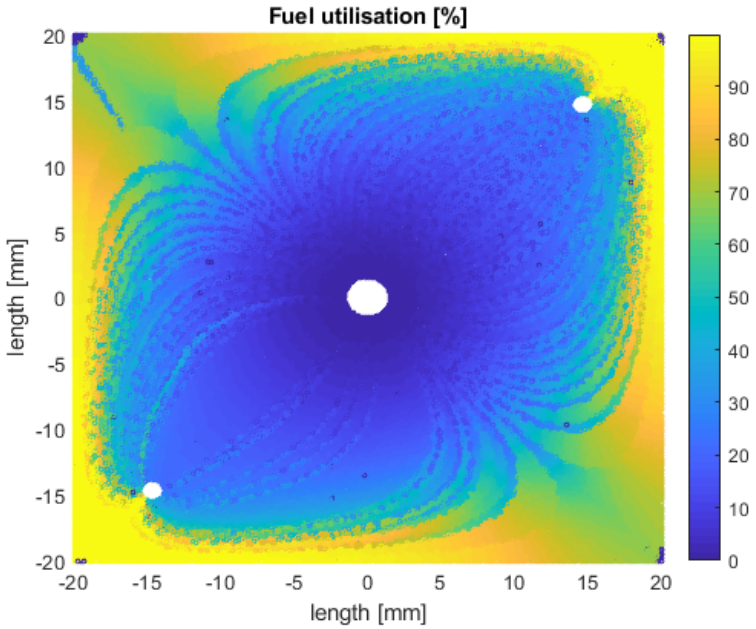

Figure C.12: Fuel utilisation of the setup case with higher flows and without nickel foam diffuser.

Appendix D

Experiment manual

In this appendix the method of assembling the cell in the setup used by the university is described step by step.
Firstly the the seals need to be cut to dimension. The mica sheets with thickness of 0.7mm is cut to 60mm by 60mm outer dimensions and 40mm by 40mm inner dimensions. A nickel foam with a thickness of 0.55mm needs to be cut to 40mm by 40mm dimensions. Lastly 2 aluminafelt sheets are taken. One of these sheets requires a square cut out of 40mm by 40mm in the middle which is rotated 45 degrees compared to the sheet. The end products are displayed in Figure D.1. The cell is not displayed in the figure, but is necessary for testing.

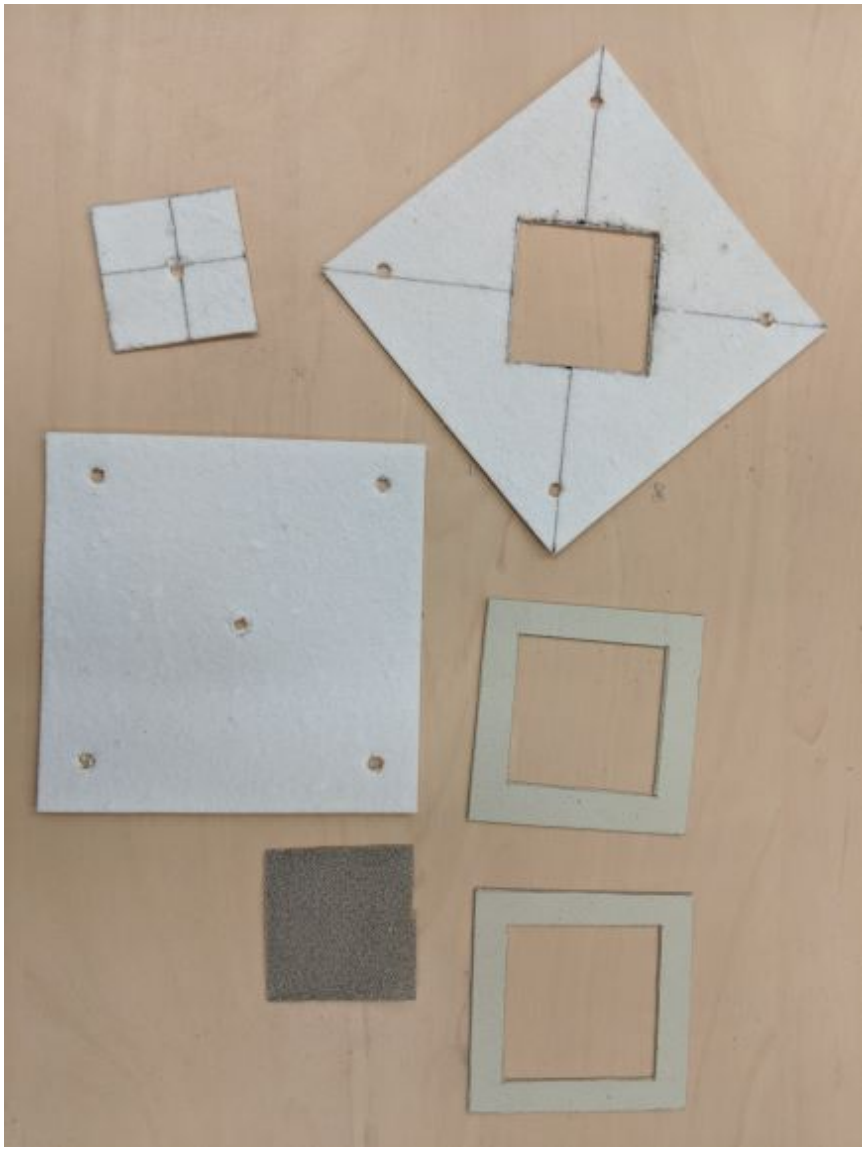

Figure D.1: Items required for assembly. From top left to bottom right: aluminafelt cut out, aluminafelt #1, aluminafelt #2, mica sheet, nickel foam, mica sheet.

Before assembly begins the fuel flow distribution plate needs to be sanded down and cleaned with a cleaning agent to improve the seal between the plate and the mica sheet. After cleaning place a mica sheet on the distribution plate in a manner that the inlets and outlets are encompassed by the mica sheet. The nickel foam should fit right in the center of the mica sheet. To prevent the mica sheet from moving during assembly tape the mica to the distribution plate with painters tape. The use of stronger tapes is highly discouraged as those tapes do not burn off as easily as painters tape.

These steps are depicted in Figure D.2.

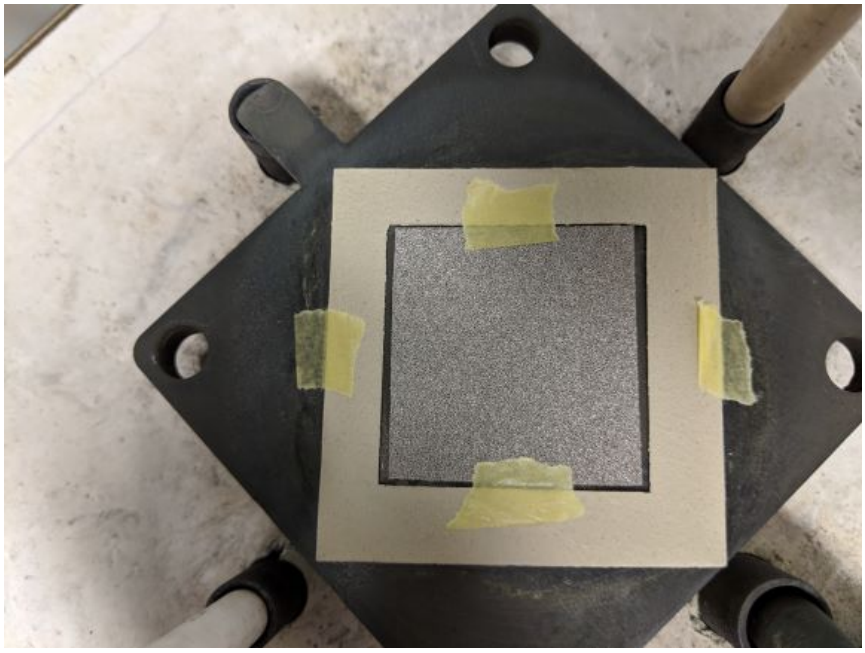

Figure D.2: Assembly of the first mica sheet and the nickel foam diffuser.

With the nickel foam in place the cell can be place on top of the nickel foam and mica sheet with the green nickel electrode down. The second mica sheet can be placed on top of the cell in manner that leaves the black air electrode fully exposed. This is shown in Figure D.3. Again to aid assembly the mica sheet is taped down to the distribution plate.

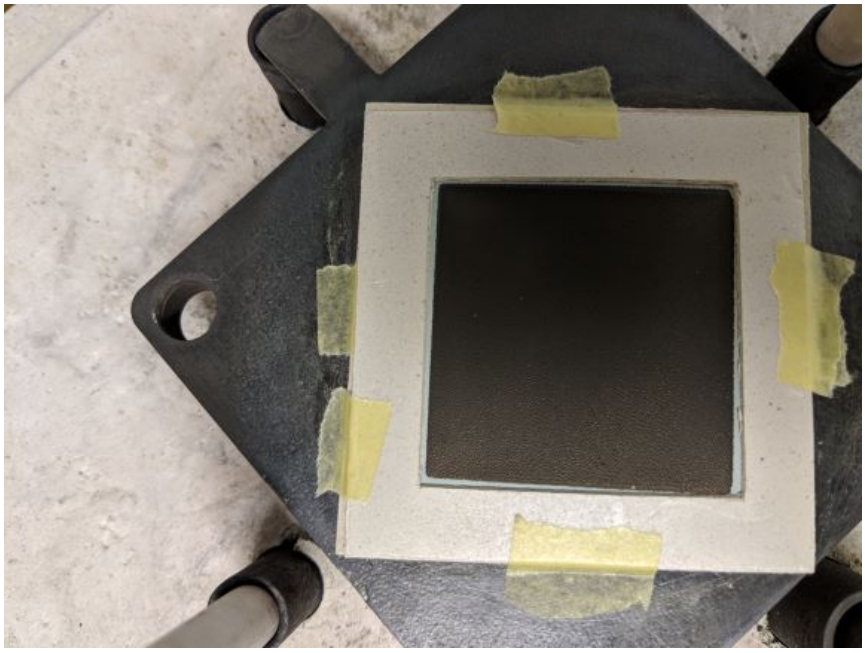

Figure D.3: Assembly of the cell and second mica sheet.

After the cell and mica sheet are placed the aluminafelt with the square cutout is place on top of the cell. The cutout of the aluminafelt lines up with the cell leaving the air electrode exposed whilst simultaneously lining up the holes on the corners of the felt with those of the distribution plate. With the aluminafelt in place the platinum current collector is placed on the air electrode as displayed in Figure D.4. The cutout of the aluminafelt is placed on top of the platinum current collector and the last aluminafelt is placed on top of that. The end result should look similar to Figure D.5.

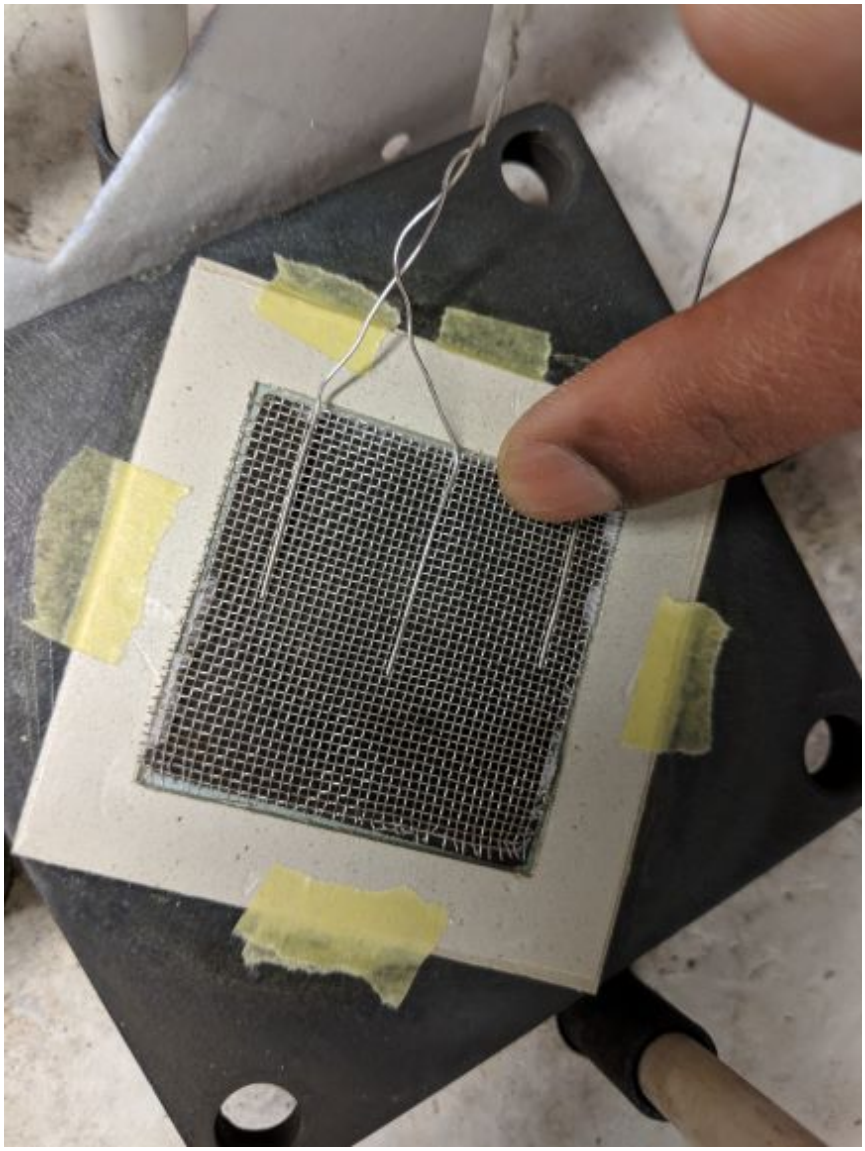

Figure D.4: A figure depicting how the platinum current collector should be placed on the air electrode.

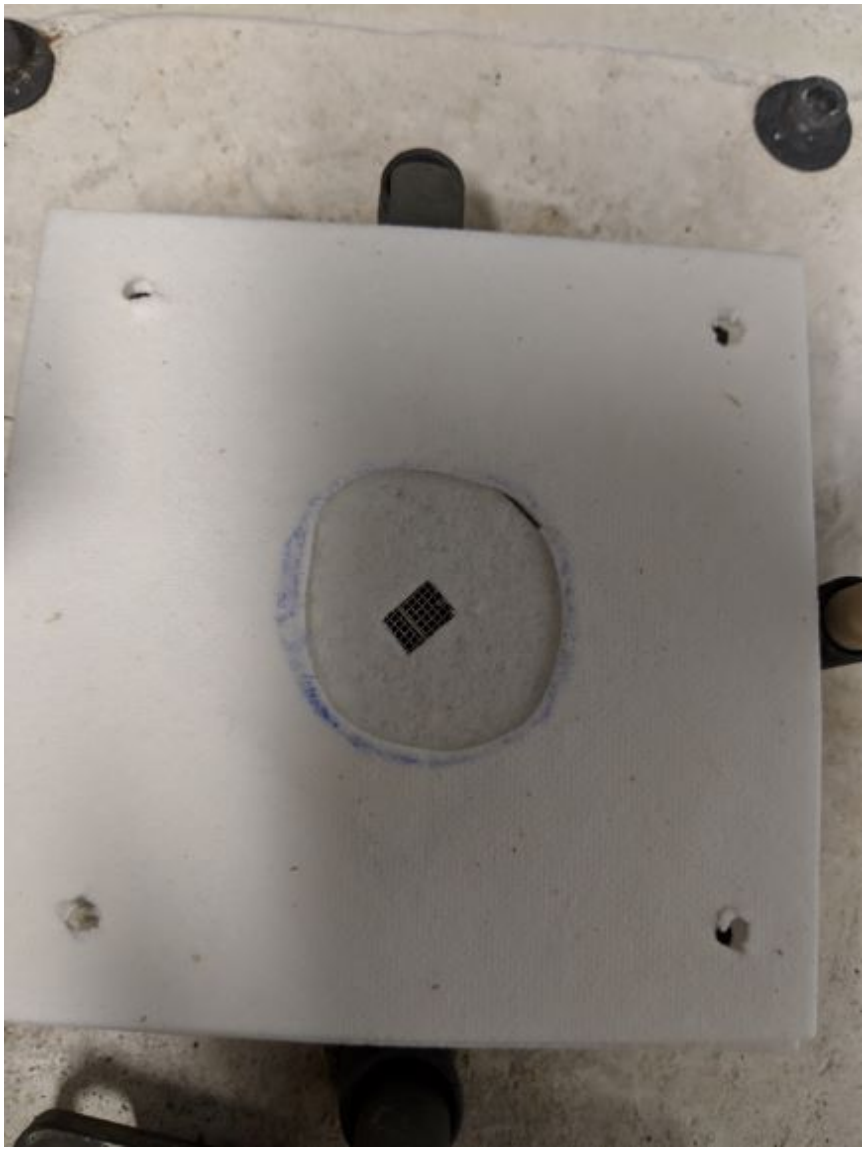

Figure D.5: Assembly with the aluminafelts in place.

With the aluminafelts in place the air flow distribution plate can be placed on top. With the air distribution plate in place the retention bolts can be inserted in the way that is depicted in Figure D.6. On the bottom of the retention bolts springs are attached. These springs have an unloaded length of 29mm and a spring constant of $3kg/mm$ and were tightened to 26mm during testing. The whole setup can now be flipped upside down and lowered into the oven for testing.

Figure D.6: Fully assembled setup.

Bibliography

[1] UNFCCC. Conference of the Parties (COP). ADOPTION OF THE PARIS AGREEMENT - Conference of the Parties COP 21. *Adoption of the Paris Agreement. Proposal by the President.*, 21932(December):32, 2015. ISSN 1098-6596. doi: FCCC/CP/2015/L.9/Rev.1. URL http://unfccc.int/resource/docs/2015/cop21/eng/l09r01.pdf.

[2] Erin Beddingfield, Keith Forbes, Kristin Igusky, Makely Lyon, Michael Mondshine, and Richard Richards. Emissions of Greenhouse Gases in the United States 2009, DOE/EIA-0573(2009). *U.S. Energy Information Administration*, (March), 2011. URL https://www.eia.gov/environment/emissions/ghg{_}report/pdf/0573{%}282009{%}29.pdf.

[3] CBS. StatLine - Emissies van broeikasgassen berekend volgens IPCC-voorschriften, 2019. URL https://opendata.cbs.nl/statline/{#}/CBS/nl/dataset/70946ned/table?dl=10757.

[4] International Renewable Energy Agency. *Renewable capacity statistics 2018 Statistiques de capacité renouvelable 2018 Estadísticas de capacidad renovable 2018*. 2018. ISBN 9789295111905.

[5] Renew Economy. The stunning numbers behind success of Tesla big battery | RenewEconomy, 2018. URL https://reneweconomy.com.au/the-stunning-numbers-behind-success-of-tesla-big-battery-63917/.

[6] Balance project. Description — BALANCE project, 2016. URL https://www.balance-project.org/projects.

[7] Syngaschem BV. Synthesis Gas Chemistry and Synthetic Fuels - Syngaschem BV, 2012. URL http://www.syngaschem.com/syngaschem.

[8] Joshua Mermelstein and Oliver Posdziech. Development and Demonstration of a Novel Reversible SOFC System for Utility and Micro Grid Energy Storage. *Fuel Cells*, 17(4):562–570, 2017. ISSN 16156854. doi: 10.1002/fuce.201600185.

[9] S. Santhanam, M. P. Heddrich, M. Riedel, and K. A. Friedrich. Theoretical and experimental study of Reversible Solid Oxide Cell (r-SOC) systems for energy storage. *Energy*, 141:202–214, 2017. ISSN 03605442. doi: 10.1016/j.energy.2017.09.081. URL https://doi.org/10.1016/j.energy.2017.09.081.

[10] Foteini M. Sapountzi, Jose M. Gracia, C. J.(Kees Jan) Weststrate, Hans O.A. Fredriksson, and J. W.(Hans) Niemantsverdriet. Electrocatalysts for the generation of hydrogen, oxygen and

synthesis gas. *Progress in Energy and Combustion Science*, 58:1–35, 2017. ISSN 03601285. doi: 10.1016/j.pecs.2016.09.001. URL http://dx.doi.org/10.1016/j.pecs.2016.09.001.

[11] Floriane Petipas, Annabelle Brisse, and Chakib Bouallou. Thermal management of solid oxide electrolysis cell systems through air flow regulation. *Chemical Engineering Transactions*, 61: 1069–1074, 2017. ISSN 22839216. doi: 10.3303/CET1761176.

[12] Sune Dalgaard Ebbesen, Søren Højgaard Jensen, Anne Hauch, and Mogens Bjerg Mogensen. High temperature electrolysis in alkaline cells, solid proton conducting cells, and solid oxide cells. *Chemical Reviews*, 114(21):10697–10734, 2014. ISSN 15206890. doi: 10.1021/cr5000865.

[13] Eric D. Wachsman and Kang Taek Lee. Lowering the temperature of solid oxide fuel cells. *Science*, 334(6058):935–939, 2011. ISSN 10959203. doi: 10.1126/science.1204090.

[14] Daniel J.L. Brett, Alan Atkinson, Nigel P. Brandon, and Stephen J. Skinner. Intermediate temperature solid oxide fuel cells. *Chemical Society Reviews*, 37(8):1568–1578, 2008. ISSN 03060012. doi: 10.1039/b612060c.

[15] Tatsumi Ishihara. *Perovskite oxide for solid oxide fuel cells*. Springer, 2009. ISBN 9780387777085.

[16] LibreTexts. Nernst Equation - Chemistry LibreTexts, 2019. URL https://chem.libretexts.org/Bookshelves/Analytical{_}Chemistry/Supplemental{_}Modules{_}(Analytical{_}Chemistry)/Electrochemistry/Nernst{_}Equation.

[17] Martin Bazant. Lecture 8: The Nernst equation. *MIT opencourse lecture*, 1(3):1–11, 2014.

[18] J. Udagawa, P. Aguiar, and N. P. Brandon. Hydrogen production through steam electrolysis: Model-based steady state performance of a cathode-supported intermediate temperature solid oxide electrolysis cell. *Journal of Power Sources*, 166(1):127–136, 2007. ISSN 03787753. doi: 10.1016/j.jpowsour.2006.12.081.

[19] Q. Cai, E. Luna-Ortiz, C. S. Adjiman, and N. P. Brandon. The effects of operating conditions on the performance of a solid oxide steam electrolyser: A model-based study. *Fuel Cells*, 10 (6):1114–1128, 2010. ISSN 16156846. doi: 10.1002/fuce.200900211.

[20] Vinod M. Janardhanan and Olaf Deutschmann. Modeling of solid-oxide fuel cells. *Zeitschrift fur Physikalische Chemie*, 221(4):443–479, 2007. ISSN 09429352. doi: 10.1524/zpch.2007.221.4.443.

[21] Denver F. Cheddie and Norman D.H. Munroe. A dynamic 1D model of a solid oxide fuel cell for real time simulation. *Journal of Power Sources*, 171(2):634–643, 2007. ISSN 03787753. doi: 10.1016/j.jpowsour.2007.06.170.

[22] Harvind Arjun Rai. Steady-State Multiplicity and Transient Behaviour within a Lumped-Parameter Solid Oxide Fuel Cell. (September), 2016.

[23] Su Jeong Heo and Junsung Hong. Chromium Poisoning of La 1-x Sr x MnO 3 $\pm$ δ Cathodes and Electrochemical Validation of Chromium Getters in Intermediate Temperature-Solid Oxide Fuel Cells. 166(13):990–995, 2019. doi: 10.1149/2.0931913jes.

[24] Ruth Knibbe, Johan Hjelm, Mohan Menon, Nini Pryds, Martin Søgaard, Hsiang Jen Wang, and Kai Neufeld. Cathode-Electrolyte Interfaces with CGO Barrier Layers in SOFC. *Journal of the American Ceramic Society*, 93(9):2877–2883, apr 2010. ISSN 00027820. doi: 10.1111/j.1551-2916.2010.03763.x. URL http://doi.wiley.com/10.1111/j.1551-2916.2010.03763.x.

[25] B. Shri Prakash, S. Senthil Kumar, and S. T. Aruna. Properties and development of Ni/YSZ as an anode material in solid oxide fuel cell: A review, 2014. ISSN 13640321.

[26] Shabana P.S. Shaikh, Andanastuti Muchtar, and Mahendra R. Somalu. A review on the selection of anode materials for solid-oxide fuel cells. *Renewable and Sustainable Energy Reviews*, 51:1–8, 2015. ISSN 18790690. doi: 10.1016/j.rser.2015.05.069. URL http://dx.doi.org/10.1016/j.rser.2015.05.069.

[27] Milad Ebadi Chelmehsara and Javad Mahmoudimehr. Techno-economic comparison of anode-supported, cathode-supported, and electrolyte-supported SOFCs. *International Journal of Hydrogen Energy*, 2018. ISSN 03603199. doi: 10.1016/j.ijhydene.2018.06.114.

[28] Han Xu, Zheng Dang, and Bo Feng Bai. Electrochemical performance study of solid oxide fuel cell using lattice Boltzmann method. *Energy*, 67:575–583, 2014. ISSN 03605442. doi: 10.1016/j.energy.2014.02.021. URL http://dx.doi.org/10.1016/j.energy.2014.02.021.

[29] W Bujalski. UoB lecture slides on Solid Oxide Fuel Cells (SOFCs), 2018. URL http://www.durablepower.eu/images/downloads/hoe/02{_}01{_}03{_}REALSOFC{_}3Review+testing+project.pdf.

[30] Detlef. Stolten and Bernd. Emonts. *Fuel cell science and engineering : materials, processes, systems and technology*. John Wiley & Sons, 2012. ISBN 3527650261. URL https://books.google.nl/books?id=EzXQOUuHUb0C{&}pg=PA48{&}lpg=PA48{&}dq=sofc+current+collection+gold+platinum{&}source=bl{&}ots=Tnw180I2kW{&}sig=ACfU3U1-f3XXcYCh43n-9vc9Z64wfXGvyw{&}hl=nl{&}sa=X{&}ved=2ahUKEwjy-4DD7sjkAhXFUlAKHZHOBhQQ6AEwEHoECAkQAQ{#}v=onepage{&}q=sofccurrent.

[31] Chihiro Hiraiwa, Kazuki Okuno, Hiromasa Tawarayama, Masatoshi Majima, Junichi Nishimura, and Hitoshi Tsuchida. Application of Ni porous metal to solid oxide fuel cells. *SEI Technical Review*, (83):59–65, 2016. ISSN 13434349.

[32] Neelima Mahato, Amitava Banerjee, Alka Gupta, Shobit Omar, and Kantesh Balani. Progress in material selection for solid oxide fuel cell technology: A review. *Progress in Materials Science*, 72:141–337, 2015. ISSN 00796425. doi: 10.1016/j.pmatsci.2015.01.001. URL http://dx.doi.org/10.1016/j.pmatsci.2015.01.001.

[33] Theis L Skafte, Johan Hjelm, Peter Blennow, and Christopher Graves. Quantitative review of degradation and lifetime of solid oxide cells and stacks. *EFCF 2016 proceedings*, (B0501): 8–26, 2016.

[34] Joseph D Fehribach. The support of the National Science Foundation under grant DMS-0707692 is gratefully ac- knowledged. ∗.

[35] Jürgen Fleig. Solid Oxide Fuel Cell Cathodes: Polarization Mechanisms and Modeling of the Electrochemical Performance. *Annual Review of Materials Research*, 33(1):361–382, 2003. ISSN 1531-7331. doi: 10.1146/annurev.matsci.33.022802.093258.

[36] F. Tietz. Thermal expansion of SOFC materials. *Ionics*, 5(1-2):129–139, 1999. ISSN 18620760. doi: 10.1007/BF02375916.

[37] Julie Tavernier, Muhammad Imran Asghar, and Peter Lund. Thermal expansion modeling to predict cracks in SOFC. pages 61–63.

[38] M. Kornely, N. H. Menzler, A. Weber, and E. Ivers-Tiffée. Degradation of a High Performance SOFC Cathode by Cr-Poisoning at OCV-Conditions. *Fuel Cells*, 13(4):506–510, 2013. ISSN 16156846. doi: 10.1002/fuce.201200182.

[39] J. Andreas Schuler, Harumi Yokokawa, Caroline F. Calderone, Quentin Jeangros, Zacharie Wuillemin, Aïcha Hessler-Wyser, and Jan Van Herle. Combined Cr and S poisoning in solid oxide fuel cell cathodes. *Journal of Power Sources*, 201:112–120, 2012. ISSN 03787753. doi: 10.1016/j.jpowsour.2011.10.123. URL http://dx.doi.org/10.1016/j.jpowsour.2011.10.123.

[40] Kongfa Chen and San Ping Jiang. Review - Materials degradation of solid oxide electrolysis cells. *Journal of the Electrochemical Society*, 163(11):F3070–F3083, 2016. ISSN 19457111. doi: 10.1149/2.0101611jes.

[41] K. P. Lillerud and P. Kofstad. High Temperature Oxidation of Chromium. *International Corrosion Conference Series*, 127(1):155–161, 1983. ISSN 03614409.

[42] Paolo R. Zafred, Stephen W. Sofie, and Paul S. Gentile. Progress in Understanding Silica Transport Process and Effects in Solid Oxide Fuel Cell Performance. In *ASME 2010 8th International Fuel Cell Science, Engineering and Technology Conference: Volume 2*, pages 421–426. ASME, 2010. ISBN 978-0-7918-4405-2. doi: 10.1115/FuelCell2010-33297. URL http://proceedings.asmedigitalcollection.asme.org/proceeding.aspx?articleid=1610682.

[43] D. Simwonis, F. Tietz, and D. Stöver. Nickel coarsening in annealed Ni/8YSZ anode substrates for solid oxide fuel cells. *Solid State Ionics*, 132(3):241–251, 2000. ISSN 01672738.

[44] Rostislav A. Andrievski and Arsen V. Khatchoyan. Grain Growth and Nanomaterials Behavior at High Temperatures. pages 7–25. Springer, Cham, 2016. doi: 10.1007/978-3-319-25331-2_2. URL http://link.springer.com/10.1007/978-3-319-25331-2{_}2.

[45] M.S. Sohal. Degradation Issues in Solid Oxide Cells During High Accessed. *MIT opencourse lecture*, 1, 2010.

[46] Anil V. Virkar, Hyung Tae Lim, and Greg Tao. Failure of solid oxide fuel cells by electrochemically induced pressure. *Procedia IUTAM*, 10:328–337, 2014. ISSN 22109838. doi: 10.1016/j.piutam.2014.01.028. URL http://dx.doi.org/10.1016/j.piutam.2014.01.028.

[47] Muhammad Shirjeel Khan, Xiaoyong Xu, Jie Zhao, Ruth Knibbe, and Zhonghua Zhu. A porous yttria-stabilized zirconia layer to eliminate the delamination of air electrode in solid oxide electrolysis cells. *Journal of Power Sources*, 359(September 2018):104–110, 2017. ISSN 03787753. doi: 10.1016/j.jpowsour.2017.05.049. URL http://dx.doi.org/10.1016/j.jpowsour.2017.05.049.

[48] A.V. Virkar. Mechansim of Oxygen Electrode Delamination in Solid Oxide Electrolyser Cells. *International Journal of Hydrogen Energy*, 35(18):9527–9543, 2010. ISSN 0360-3199. doi: 10.1016/j.ijhydene.2010.06.058. URL http://dx.doi.org/10.1016/j.ijhydene.2010.06.058.

[49] Marko Nerat and Đani Juričić. Modelling of anode delamination in solid oxide electrolysis cell and analysis of its effects on electrochemical performance. *International Journal of Hydrogen Energy*, 43(17):8179–8189, 2018. ISSN 03603199. doi: 10.1016/j.ijhydene.2018.02.189.

[50] R. Vaßen, D. Simwonis, and D. Stöver. Modelling of the agglomeration of Ni-particles in anodes of solid oxide fuel cells. *Journal of Materials Science*, 36(1):147–151, 2001. ISSN 00222461. doi: 10.1023/A:1004849322160.

[51] A. Zekri, K. Herbrig, M. Knipper, J. Parisi, and T. Plaggenborg. Nickel Depletion and Agglomeration in SOFC Anodes During Long-Term Operation. *Fuel Cells*, 17(3):359–366, 2017. ISSN 16156854. doi: 10.1002/fuce.201600220.

[52] Chao Yang, Jiatang Wang, Jiapei Zhao, Yu Wu, Chen Shu, He Miao, Fu Wang, Weiqiang Ye, and Jinliang Yuan. CFD modeling and performance comparison of solid oxide fuel cell and electrolysis cell fueled with syngas. *International Journal of Energy Research*, 43(7):2656–2677, 2019. ISSN 1099114X. doi: 10.1002/er.4315.

[53] H. W. Choi, J. G. Pharoah, D. Ryland, A. Kettner, and N. Gnanapragasam. Computational fluid dynamics modeling of solid oxide electrolysis cell. *ECS Transactions*, 57(1):3161–3170, 2013. ISSN 19386737. doi: 10.1149/05701.3161ecst.

[54] R. T. Nishida, S. B. Beale, and J. G. Pharoah. Comprehensive computational fluid dynamics model of solid oxide fuel cell stacks. *International Journal of Hydrogen Energy*, 41(45):20592–20605, 2016. ISSN 03603199. doi: 10.1016/j.ijhydene.2016.05.103. URL http://dx.doi.org/10.1016/j.ijhydene.2016.05.103.

[55] M. Andersson, J. Yuan, and B. Sundén. SOFC cell design optimization using the finite element method based CFD approach. *Fuel Cells*, 14(2):177–188, 2014. ISSN 16156854. doi: 10.1002/fuce.201300160.

[56] J.N. Stam, D.J.E.M. Roekaerts, and P.V. Aravind. Modeling of radiative heat transfer in solid oxide fuel cells. *Proceedings of the 7th european fuel cell piero lunghi conference*, pages 331–332, 2017.

[57] Paulina Pianko-Oprych, Tomasz Zinko, and Zdzislaw Jaworski. A numerical investigation of the thermal stresses of a planar solid oxide fuel cell. *Materials*, 9(10), 2016. ISSN 19961944. doi: 10.3390/ma9100814.

[58] Paulina Pianko-Oprych, Tomasz Zinko, and Zdzislaw Jaworski. Computational fluid dynamics calculation of a planar solid oxide fuel cell design running on syngas. *Chemical and Process Engineering - Inżynieria Chemiczna i Procesowa*, 38(4):513–521, 2017. ISSN 02086425. doi: 10.1515/cpe-2017-0040.

[59] W. Wu, G. L. Wang, W. B. Guan, Y. F. Zhen, and W. G. Wang. Effect of contact method between interconnects and electrodes on area specific resistance in planar solid oxide fuel cells. *Fuel Cells*, 13(5):743–750, 2013. ISSN 16156846. doi: 10.1002/fuce.201300028.

[60] K. Sudaprasert, R. P. Travis, and R. F. Martinez-Botas. A computational fluid dynamics model of a solid oxide fuel cell. *Proceedings of the Institution of Mechanical Engineers, Part A: Journal of Power and Energy*, 219(3):159–167, 2005. ISSN 09576509. doi: 10.1243/095765005X7583.

[61] Ugur Pasaogullari and Chao-Yang Wang. Computational Fluid Dynamics Modeling of Solid Oxide Fuel Cells. *ECS Proceedings Volumes*, 2003-07:1403–1412, 2003. ISSN 0161-6374. doi: 10.1149/200307.1403pv.

[62] A.F. Mills. *Basic Heat and Mass Transfer: Int.* 2 edition, 2013. ISBN 9781292042480.

[63] Pijush K. Kundu, Ira M. Cohen, and David R. Dowling. *Fluid mechanics: Sixth edition*. Elsevier, jan 2015. ISBN 9780124059351.

[64] Bastian E. Rapp. *Microfluidics: Modeling, mechanics and mathematics*. Elsevier Inc., dec 2016. ISBN 9781455731411. doi: 10.1016/c2012-0-02230-2.

[65] Nasa. Definition of Streamlines. URL https://www.grc.nasa.gov/www/k-12/airplane/stream.html.

[66] LibreTexts. 7.5: Equipotential Surfaces and Conductors - Physics LibreTexts, 2019. URL https://phys.libretexts.org/Bookshelves/University{_}Physics/Book{%}3A{_}University{_}Physics{_}(OpenStax)/Map{%}3A{_}University{_}Physics{_}II{_}-{_}Thermodynamics{%}2C{_}\Electricity{%}2C{_}and{_}Magnetism{_}(OpenStax)/7{%}3A{_}Electric{_}Potential/7.5{%}\3A{_}Equipotential{_}Surfaces{_}and{_}Conductors.

[67] China Ser and B-Chem | Apr. Advance in highly efficient hydrogen production by high temperature steam electrolysis. 51(4):289–304, 2008. doi: 10.1007/s11426-008-0054-z. URL www.scichina.com.